UC San Diego
UC San Diego Electronic Theses and Dissertations

Title

Expanding Silicon Photonics Through Novel Components and Applications

Permalink

https://escholarship.org/uc/item/2s00x7rc

Author

Wang, Xiaoxi

Publication Date

2022

Peer reviewed|Thesis/dissertation

UNIVERSITY OF CALIFORNIA SAN DIEGO

Expanding Silicon Photonics Through Novel Components and Applications

A Dissertation submitted in partial satisfaction of the requirements
for the degree Doctor of Philosophy

in

Electrical Engineering (Photonics)

by

Xiaoxi Wang

Committee in charge:

      Professor Shayan Mookherjea, Chair
      Professor Julio Barreiro
      Professor Dinesh Bharadia
      Professor George Papen

2022

The Dissertation of Xiaoxi Wang is approved, and it is acceptable in quality and form for publication on microfilm and electronically.

University of California San Diego

2022

DEDICATION

I dedicate this work to my parents and family, who have tirelessly supported my

education throughout my life, and have always believed in my ability to improve and pursue my

goals.

TABLE OF CONTENTS

LIST OF FIGURES

LIST OF TABLES

ACKNOWLEDGEMENTS

First and foremost, I would like to thank my advisor, Prof. Shayan Mookherjea, for supporting me through the many years of my graduate school. It is rare to have an advisor who values intellectual freedom and exploration for his students and graciously offers an abundance of his time to personally train and develop their research skills, while at the same time being an inspiring leader. His passion for research, expertise, scientific vision and breadth, and professionalism have been a constant source of inspiration for me. The past few years have been not just the most formative of my career, but also the most fun, and I am very grateful to have his guidance, wisdom, and encouragement.

I would like to thank my doctoral committee: Prof. George Papen, Prof. Julio Barreiro, and Prof. Dinesh Bharadia—I am very grateful for our discussions. Prof. George Papen's graduate classes in optics were also some the best classes I have ever taken, and I am also grateful for his teachings and layered perspectives of tackling different aspects of research.

I would like to thank all my former and current colleagues from Shayan's lab: Dr. Ranjeet Kumar, Dr. Ryan Aguinaldo, Dr. Marc Savanier, Dr. Peter Weigel, Dr. Hannah Grant, Dr. Chaoxuan Ma, Nikhil Mathur, Dr. Jie Zhao, Dr. Michael Rusing, Forrest Valdez, Victor Gunawan, Jinhua Xu, Dr. Viphretuo Mere, Carson Valdez, and Ferrill Rushton. Ranjeet was the first person in the group I met during my visit at the Ph.D. recruitment; I'm thankful that he helped convince me to join in the beginning, and I'm thankful for collaborations from Ranjeet and Dr. Haisheng Rong's Intel team and advice in the subsequent years. Ryan's gracious support in getting started with Silvaco simulations during my first few months on his visits to the lab after his graduation were immensely helpful. I'm very thankful for Marc's guidance and wisdom when I first joined,

and offering his talented expertise and guidance as I was learning new things in photonic chip design.

I would like to thank Peter for his guidance and skill in explaining concepts to me in my early years in the group, for always being a reliable source of feedback on my work, and for being a great scientist to bounce ideas around with. I am tremendously thankful for his pioneering work in bonded thin film lithium niobate, without which some of the subsequent work in this dissertation would not have been possible. I am very thankful to have Ellen (Chaoxuan) as a labmate and close collaborator throughout our silicon photonic projects. Much of my work would not have been possible without her—I cherish the journey through struggles, successes, and the great amount of learning together. I have much nostalgia for the very long hours we have spent debugging puzzles, and admire her relentless pursuit of reaching project milestones. It has very much been a joy to develop ideas and projects with her. I am thankful to have Jie as a colleague during my graduate school years as well—I cherish our many research discussions on lithium niobate and nonlinear photonics. I'm very grateful for her help fabricating the devices in the cleanroom and process discussions. Jie has never hesitated to lend a hand on many experiments—I have also enjoyed sampling different Chinese food with her and Yue, and discussing the different regional flavors. I would also like to thank Hannah for her help on early projects, sharing her experience on different optical setups, trips to various restaurants, and selfless sharing of some outstanding coffee beans. I am thankful that Michael brought his lithium niobate expertise and comraderie to the lab, during his years as a postdoctoral fellow here, as well as his love for airplanes and continuing discussions not only in science but also science fiction (and fantasy). His scientific intuition, creativity, and knack for out of the box ideas is infectious, and it is always a joy having long discussions with him. I'd like to thank Victor for his help on FPGAs and all that I've learned from him. Forrest has

been a great help on many projects in the early years, and I am grateful we have been able to work together on lithium niobate projects in the recent years. It has been great fun working on the higher power modulators and hitting some major milestones together, and I look forward to his coming developments. I'm very grateful that Viphretuo joined our group and has led the charge in the recent fabrication of the current lithium niobate projects. His tremendous depth of experience in the clean room and skill in fabrication is a joy to see and learn from. The last year and half of Covid experience and earlier periods of isolation when Viphretuo joined has been fun, while sharing food, movie, and California experiences. I look forward to seeing his future development and research.

I would also like to thank our collaborators at the NASA Jet Propulsion Lab—Dr. Matt Shaw, Dr. Boris Korzh, Dr. Brian Drouin, Dr. Deacon Nemchick, and the MIT SNSPD team. Matt hosted me as a visiting researcher during my work on our >100 GHz single photon sampling oscilloscope project, graciously helped me get our experiments set up, and connected me with a great depth of expertise at JPL. I thank Boris for his great mentorship, and training me on single photon detectors, cryogenics, and helping us get our cryo setup with more advanced detectors and readout. Boris's passion for pushing the boundaries of scientific advances and devices has been a great motivation to me—our discussions on out of the box experiments and science during coffee breaks after working in the dark, pizza dinners, and outings has been a great joy. I am very much grateful for Brian and Deacon's help on setting up the RF amplifiers and lending their expertise. I am very thankful to have spent those months with everyone on Matt's team at JPL: Dr. Emma Wollman, Dr. Jason Allmaras, Dr. Andrew Mueller, Eddie Ramirez, and Dr. Andrew Beyer. I would also like to thank Dr. Scott Merritt and the NASA NSTRF team for their support through those years.

Chapter 3 contains material published in: Xiaoxi Wang and Shayan Mookherjea, "High-speed silicon microresonator modulators with high optical modulation amplitude (OMA) at input powers >10 mW," Opt. Express 30, 6826-6837 (2022). The dissertation author was the primary author of this paper.

Chapter 5 contains material published in: Xiaoxi Wang and Shayan Mookherjea, "Performance comparisons between semiconductor and fiber amplifier gain assistance in a recirculating frequency shifter," Opt. Lett. 43, 1011-1014 (2018). The dissertation author was the primary author of this paper.

Chapter 6, in part, is currently being prepared for submission for publication of the material. Xiaoxi Wang, Forrest Valdez, Viphretuo Mere, and Shayan Mookherjea, The dissertation author was the primary author, and together with his adviser, led the research efforts for this work.

Chapter 7, contains material published in: Xiaoxi Wang, Forrest Valdez, Viphretuo Mere, and Shayan Mookherjea, "Monolithic Integration of 110 GHz Thin-film Lithium Niobate Modulator and High-Q Silicon Microring Resonator for Photon-Pair Generation," in Conference on Lasers and Electro-Optics, Technical Digest Series (Optica Publishing Group, 2022), paper JTh6B.9. The dissertation author was the primary author of this paper. Chapter 7, in part, is currently being prepared for submission for publication of the material. Xiaoxi Wang, Forrest Valdez, Viphretuo Mere, and Shayan Mookherjea, The dissertation author was the primary author, and together with his adviser, led the research efforts for this work.

Chapter 8, in part, is currently being prepared for submission for publication of the material. Xiaoxi Wang, and Shayan Mookherjea, The dissertation author was the primary author, and together with his adviser, led the research efforts for this work.

VITA

2012   Bachelor of Science in Electrical Engineering, Massachusetts Institute of Technology

2017   Master of Science in Electrical Engineering (Photonics), University of California San Diego

2022   Doctor of Philosophy in Electrical Engineering (Photonics), University of California San Diego

PUBLICATIONS

Xiaoxi Wang, Forrest Valdez, Viphretuo Mere, and Shayan Mookherjea, " Monolithic Integration of 110 GHz Thin-film Lithium Niobate Modulator and High-Q Silicon Microring Resonator for Photon-Pair Generation," in Conference on Lasers and Electro-Optics, Postdeadline Papers, (2022)

Xiaoxi Wang and Shayan Mookherjea, " Scalable On-Chip Single-Photon Cross-Bar Switching," in Optical Fiber Communication Conference Postdeadline Papers 2022, (OFC 2022), paper Th4C.6.

Xiaoxi Wang and Shayan Mookherjea, "High-speed silicon microresonator modulators with high optical modulation amplitude (OMA) at input powers >10 mW," Opt. Express 30, 6826-6837 (2022)

Viphretuo Mere, Forrest Valdez, Xiaoxi Wang, and Shayan Mookherjea "A Modular Fabrication Process for Thin-film Lithium Niobate Modulators with Silicon Photonics," J. Phys. Photonics, J. Phys. Photonics 4 024001 (2022)

Xiaoxi Wang, Boris A. Korzh, Matthew D. Shaw, and Shayan Mookherjea, "Full-Speed Testing of Silicon Photonic Electro-Optic Modulators from Picowatt-level Scattered Light," in Optical Fiber Communication Conference Postdeadline Papers 2020, (Optical Society of America, 2020), paper Th4A.7.

Xiaoxi Wang, Boris A. Korzh, Peter O. Weigel, Deacon J. Nemchick, Brian J. Drouin, Wolfgang Becker, Qing-Yuan Zhao, Di Zhu, Marco Colangelo, Andrew E. Dane, Karl K. Berggren, Matthew D. Shaw, and Shayan Mookherjea, "Oscilloscopic Capture of Greater-Than-100 GHz, Ultra-Low Power Optical Waveforms Enabled by Integrated Electrooptic Devices," J. Lightwave Technol., Editorial Selected Papers, 38, 166-173 (2020)

Chaoxuan Ma, Xiaoxi Wang, and Shayan Mookherjea, "Progress towards a widely usable integrated silicon photonic photon-pair source," OSA Continuum 3, 1398-1407 (2020)

Xiaoxi Wang, Peter O. Weigel, Jie Zhao, Michael Ruesing, and Shayan Mookherjea, "Achieving beyond-100-GHz large-signal modulation bandwidth in hybrid silicon photonics Mach Zehnder modulators using thin film lithium niobate," APL Photonics 4, 096101, Editor's Pick, (2019)

Xiaoxi Wang, Boris A. Korzh, Peter O. Weigel, Deacon J. Nemchick, Brian J. Drouin, Andy Fung, Woflgang Becker, Qing-Yuan Zhao, Di Zhu, Marco Colangelo, Andrew E. Dane, Karl K. Berggren, Mathew D. Shaw, and Shayan Mookherjea, "Oscilloscopic capture of 100 GHz modulated optical waveforms at femtowatt power levels," in Optical Fiber Communication Conference Postdeadline Papers 2019, (Optical Society of America, 2019), paper Th4C.1.

Xiaoxi Wang, Chaoxuan Ma, Ranjeet Kumar, Pierre Doussiere, Richard Jones, Haisheng Rong, and Shayan Mookherjea, "Photon pair generation using a silicon photonic hybrid laser", APL Photon., 3, 10, pp. 106104.

Xiaoxi Wang and Shayan Mookherjea, "Optimizing Recirculating-Frequency-Shifter performance with Semiconductor Optical Amplifier gain assistance," in Conference on Lasers and Electro-Optics, OSA Terchnical Digest (online) (Optical Society of America, 2018), paper JW2A.63.

Chaoxuan Ma, Malhar Jere, Xiaoxi Wang and S. Mookherjea, "High CAR and low g(2)(0) of 1.55 μm entangled photon-pairs generated by a silicon microring resonator," 2018 Conference on Lasers and Electro-Optics (CLEO), San Jose, CA, 2018, pp. 1-2.

Chaoxuan Ma, Xiaoxi Wang, and Shayan Mookherjea, "Photon-pair and heralded single photon generation initiated by a fraction of a 10 Gbps data stream," Opt. Express 26, 22904-22915 (2018)

Xiaoxi Wang and Shayan Mookherjea, "Performance comparisons between semiconductor and fiber amplifier gain assistance in a recirculating frequency shifter," Opt. Lett. 43, 1011-1014 (2018)

Chaoxuan Ma, Xiaoxi Wang, Vikas Anant, Andrew D. Beyer, Matthew D. Shaw, and Shayan Mookherjea, "Silicon photonic entangled photon-pair and heralded single photon generation with CAR > 12,000 and g(2)(0) < 0.006," Opt. Express 25, 32995-33006 (2017)

Xiaoxi Wang, Chaoxuan Ma, Ranjeet Kumar, Pierre Doussiere, Richard Jones, Haisheng Rong, and Shayan Mookherjea, "Photon Pair Generation Using Silicon Photonic Microring and Hybrid Laser," in Conference on Lasers and Electro-Optics, OSA Technical Digest (online), Postdeadline Papers, (Optical Society of America, 2017), paper JTh5C.6.

Xiaoxi Wang and Shayan Mookherjea, "Fast circuit modeling of heat transfer in photonic integrated circuits," in Conference on Lasers and Electro-Optics, OSA Technical Digest (online) (Optical Society of America, 2017), paper JW2A.141.

Xiaoxi Wang and Shayan Mookherjea, "Silicon photonic add-drop microring filter banks with pinch-resistor characteristics," in Conference on Lasers and Electro-Optics, OSA Technical Digest (online) (Optical Society of America, 2017), paper SW1N.6.

<u>Xiaoxi Wang</u> and Shayan Mookherjea, "Compact High-extinction-ratio Silicon Photonic Variable Optical Attenuators (VOAs)," in Conference on Lasers and Electro-Optics, OSA Technical Digest (online) (Optical Society of America, 2017), paper SW1N.7.

<u>Xiaoxi Wang</u>, Anthony Lentine, Christopher DeRose, Andrew L. Starbuck, Douglas Trotter, Andrew Pomerene, and Shayan Mookherjea, "Wide-range and fast thermally-tunable silicon photonic microring resonators using the junction field effect," Opt. Express 24, 23081-23093 (2016)

<u>Xiaoxi Wang</u>, Ryan Aguinaldo, Anthony Lentine, Christopher DeRose, Douglas Trotter, Andrew Pomerene, and Shayan Mookherjea, "Compact silicon photonic resonance-assisted variable optical attenuator," Opt. Express 24, 27600-27613 (2016)

ABSTRACT OF THE DISSERTATION

Expanding Silicon Photonics Through Novel Components and Applications

by

Xiaoxi Wang

Doctor of Philosophy in Electrical Engineering (Photonics)

University of California San Diego, 2022

Professor Shayan Mookherjea, Chair

As silicon photonics has matured in the past decade, chip scale optics have become an enabling technology for data center, RF, high speed communication, and quantum optic devices, and the number of devices being deployed into the world has increased by orders of magnitudes. However, the limitations arising from inherent optical nonlinearities in the material and mechanisms of modulation are still problems. In the present work, we describe research done to

address some of the limitations across two areas: 1) designing foundry silicon photonic resonant devices to operate at their limits of optical power and compact scalable that address wavelength selective communication needs, and 2) not-etched nor patterned thin-film lithium niobate on top of foundry silicon photonic device through hybrid integration in a scalable manner, to enable high speed (>100 GHz) and high extinction devices. The latter part of this thesis presents novel photonic circuits in which we leverage the recently developed hybrid-silicon thin-film lithium niobate platform to tune the spectral properties of quantum light generated in a monolithic chip with the hybrid material, presenting a scalable means designing beyond the limitations of conventional silicon photonics.
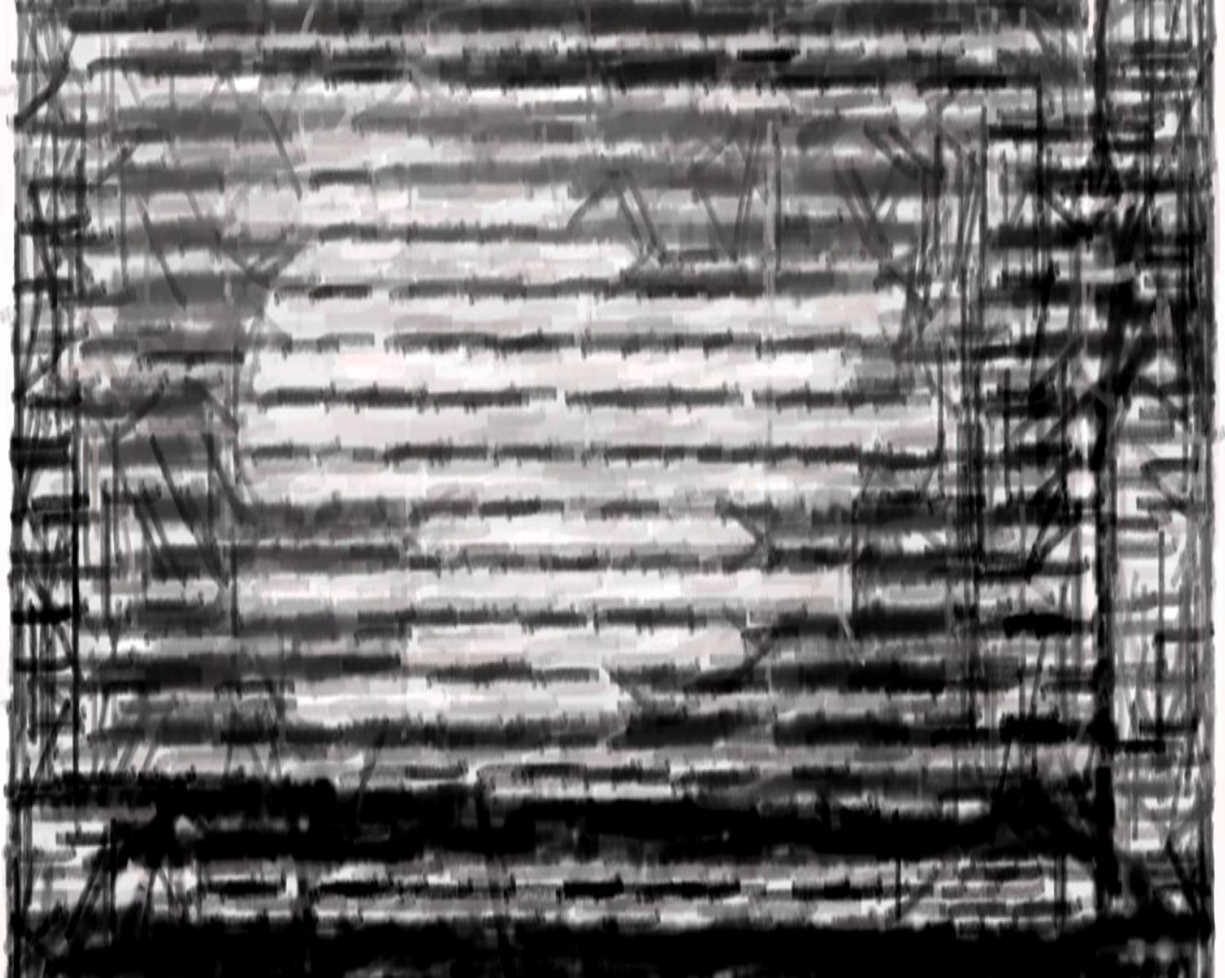
"A Neo-expressionist rendering of a bonded hybrid-lithium niobate silicon photonic chip exposing the scratches (of unknown origin) on the chip surface." art by Xiaoxi Wang, picture courtesy of Viphretuo Mere.

CHAPTER 1

Introduction

1.1 Silicon Photonics in Communication Links

The last several years have seen the proliferation of silicon photonics in not just many of the major leading silicon foundries, but also across many large and small semiconductor companies, as well as a growing community of different users [1]. The increasing breadth of adoption into different systems is a testament to the power of well-developed infrastructure and technologies spanning many decades across the microelectronics industry.

Meanwhile, the highest data-rates supported by silicon photonics have also increased, by more than an order of magnitude [2] than those demonstrated in the early half of the last prior decade. At the same time, the need for increasing bandwidths at lower operating power have not slowed down [3]. Given the advancements on the multiple fronts: custom users at different scales, rapid performance increases, and tighter integration across both different photonic devices, platforms, and electronics, it has become increasingly necessary to exploit more degrees of freedom of light and push the boundaries of what silicon photonics can handle.

One device that satisfies the need for low power consumption yet offers wavelength selectivity as a means to exploit multiple wavelengths as a degree of freedom is silicon photonic microresonator modulators based on carrier depletion. They are now increasingly adopted in a wide range of systems in modern communications, switching, and RF photonics. However, a current limitation of such devices is their ability to handle high optical power due to two-photon absorption and free-carrier generation [4], [5]. Due to these effects, silicon photonic microresonator modulators have traditionally operated at optical powers under a milliwatt (0.31 mW [6], 0.63 mW [7], and 0.30 mW [8] in prior published results). As integrated semiconductor lasers generate increasingly more optical power [4] than the sub-milliwatts in typical prior

microresonator reports, it is increasingly important to explore ways to improve high power operation of these modulators. For a certain data-rate and detection sensitivity, a higher optical modulation amplitude (OMA) directly translates into increased distance between the source and the destination. This can be critically helpful in improving the reach short-distance communications without using optical amplifiers or repeaters, or providing additional link margin for incorporation of optical switches or other devices. Chapter 2 gives an overview of these nonlinearities and Chapter 3 presents a resonant microdisc modulator with significantly higher OMA exceeding 4 mW at 13.5 mW of optical power input. Chapters 4 and 5 present elements that can be used in wavelength division multiplexing (WDM) system, that exploits some novel features for robustness.

Another path towards higher performance is presented in Chapters 6 and 7, where silicon is integrated with our recently developed thin film lithium niobate platform [9], [10]. Looking beyond what active silicon devices can handle, we exploit the high frequency capabilities of this material, while maintaining the ability to lithographically define features at the foundry level in silicon photonics through bonding. While the best-in-class modulators in this platform were recently developed, the work in this dissertation aims to develop devices and demonstrate capabilities that exploit the foundry silicon part of this platform, in results which have not been shown before.

The methods we have described in this work offers a path for synergistic advancement in hybrid development for combining best in class demonstrations from different material. Moreover, the work in this dissertation seeks to bring some of silicon's quantum optic capabilities onto this platform, as discussed in the next section.

1.2 Silicon Photonics for Single Photons

Quantum light sources that generate single and entangled photon pairs are key resources for quantum communication and computation, which are both undergoing a transformative phase from laboratory studies to large scale field deployments and systems [11], [12]. The ability to scale to larger qubit systems or systems with higher dimensionality is a key barrier to demonstrating quantum advantage—and scalable platforms that include sources of photons for carrying quantum information are increasingly needed. Even for platforms where quantum information is not encoded in photons [13]–[16], modular connections across nodes enabled by photons can offer paths to enabling large numbers of error-corrected qubits [17].

Silicon photonics, besides demonstrating large scale switching, routing, interconnects, and modulation platforms in the past decade, can also enable the generation of entangled and single photons through the χ^3 non-linear process of spontaneous four-wave mixing. Used this way, silicon photonic pair sources belong to the broad category of parametric quantum sources where pairs of photons are generated non-deterministically, as opposed to deterministic sources like quantum dots [18]–[20] or vacancy centers [21], [22] that generate single photons on-demand through deterministic processes.

Parametric sources from bulk crystals are among the most widely used sources of quantum light. Research in micro and nano fabrication in the recent decades have integrated these sources into chip-scale devices with tight optical confinement. Parametric sources of single photons have an advantage of non-cryogenic room temperature operation and paths of achieving indistinguishability, high purity sources of light [23]–[26], with methods of making them on-demand [27]–[30]. These light sources can be made from wide range of nonlinear material, some

of which are already common to silicon foundries, and chip scale demonstrations have increasingly reduced the bottlenecks to scalability. One remaining barrier to widespread adaptation of photons as quantum information carriers across large numbers of quantum information processing nodes is the indistinguishability of photons generated from multiple, different sources. However, fabrication variations from device-to-device present challenges, and the development of abilities to first tune the properties of the device is key to overcoming this barrier. For cryogenic quantum dot photon sources, very recent demonstrations of tunability on chip [31], [32] have advanced quantum interference capabilities. Room temperature parametric sources on the other hand have already demonstrated multiple photon sources showing not only quantum interference between independent devices, but also multi-qubit multi-photon higher dimensional entanglement [33]. Since these parametric sources result in photon pairs, an important condition that must be met for these parametric sources to ensure high purity and indistinguishability is separability of the biphoton states [34].

A continuous wave laser pumping a SWFM based source results in a highly entangled biphoton state, which will be projected into a mixed state on detection by a single photon click detector. Modern demonstrations of parametric sources can achieve separability through dispersion engineering and pulsed laser sources for spectral control [34], [35, p.]. However, the spectral and temporal properties of common pulse laser sources such as mode-locked lasers are not widely tunable, and so specific light sources must be selected after the parametric source is fabricated to match the properties of the nonlinear parametric device—non-ideal difference between the two can lead imperfect biphoton separability [36]–[38] [21-23]. Moreover, pulsed and mode-locked lasers themselves are challenging to integrate and are expensive devices to scale reliably. Modulators are one alternative to pulsed lasers used in both classical and quantum optical

communications, but so far, a device that can meet the high bandwidths required for precise picosecond temporal pulse tunability with high extinction and low loss, integrated with a parametric photon pair source to achieve separable states, has not yet been demonstrated.

Chapters 6-7 in this dissertation will describe the components that were designed for the first demonstration of a high extinction pulse carving modulator with more than 100 GHz of bandwidth in thin-film lithium niobate (TFLN) on a single chip with a high Q silicon microring resonators. It describes some of the work done to bring resonant microring entangled photon-pair generation devices, high quality filters, and silicon photonic circuits into our recently developed TFLN on SOI platform to show high quality control and tuning of photon pairs. Chapter 8 will describe silicon photonic devices used to switch single photons at high speeds, and detectors that can detect single photons at high time resolutions, along with a novel oscilloscopy application that extends the use of these quantum detectors for high speed detection and characterization of signals.
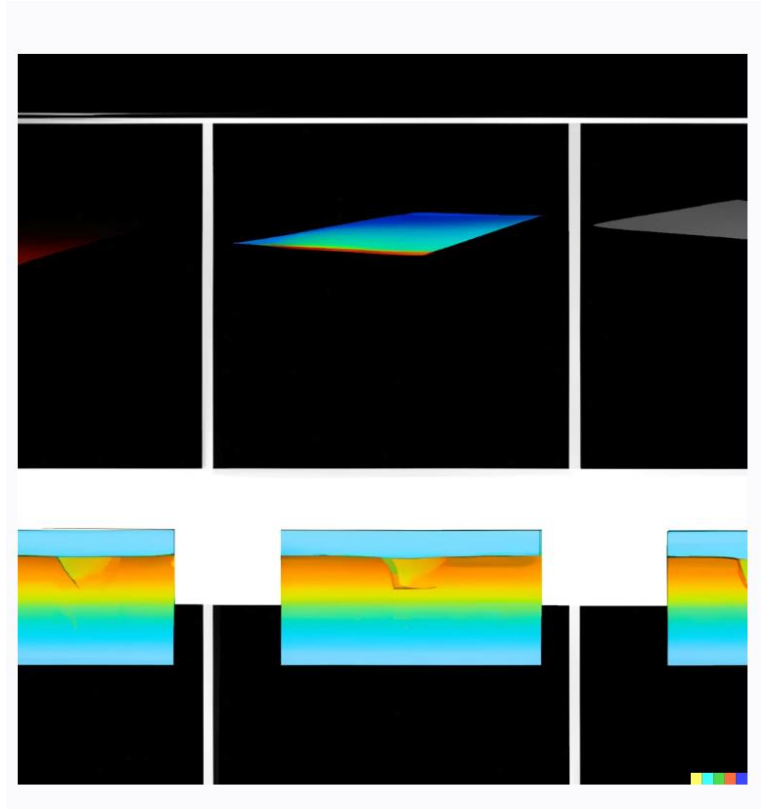
OpenAI DALL-E's interpretation of "Nonlinearities in Silicon Photonics", art courtesy of Luke Schiefelbein.

Chapter 2

Nonlinearities in Silicon Photonics

Silicon is a centrosymmetric crystal and the nonlinearities in the silicon photonics studied here arise from the third order nonlinear susceptibility, χ^3, where an induced polarization, expressed as Taylor series expansion,

$$\vec{P}(t) = \epsilon_0\left(\chi^1\vec{E}(t) + \chi^2\vec{E}^2(t) + \chi^3\vec{E}^3(t) + \cdots\right) \tag{2.1}$$

arises in response to an applied electric field $\vec{E}$, and ϵ_0 is the vacuum permittivity. Through χ^3, electric fields of different frequencies can interact with silicon and each other, through energy exchange, and fields can be generated at new frequencies. These χ^3 phenomenon are intensity dependent, and include four-wave mixing, spontaneous four-wave mixing (FWM), and two-photon absorption (TPA), which lead to the effects studied in this dissertation. It can also lead to self-phase modulation and cross-phase modulation, as well as free carrier dispersion and Raman scattering [39]–[41].

In the work here, we will most primarily look at FWM, its variants, and TPA. A conceptual cartoon of the energies and frequencies involved in TPA and FWM is shown in Fig. 2.1 (a)-(c).
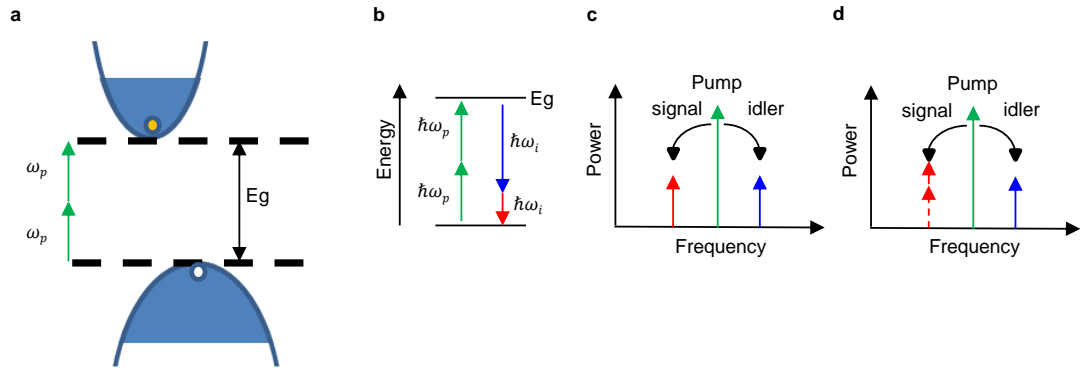
Figure 2.1: (a) Two-photon absorption (b) Energy diagram of four-wave mixing (c) Spontaneous four-wave mixing. (d) Stimulated four-wave mixing.

In the TPA process, light of energies less than the bandgap the silicon waveguide is absorbed when the energy of two photons is greater than the bandgap of silicon, $2\hbar v > E_g$. The two photons are simultaneously absorbed, and an electron is excited into the conduction band, creating an electron-hole pair, as drawn in Fig 2.1 (a). Subsequently, the mobile excited electrons and holes can be excited to even higher bands (lower for holes) through the usual linear single-photon absorption, in a process called free carrier absorption (FCA). Some types of four-wave mixing processes are shown in Fig 2.1 (c)-(d)—in a degenerate pump case, two pump photons at the same frequency are annihilated and a pair of signal and idler photons are created simultaneously. This can happen through a stimulated process, with a seed photon at the signal frequency stimulating the process, or spontaneously, with the vacuum state seeding the process. The process obeys energy conservation and so the location of the signal and idler frequencies indicated in the figures are determined by $\Delta\omega \equiv \omega_p - \omega_s = \omega_i - \omega_s$, and requires that the phase mismatch between the field vectors be small for efficiency, where the mismatch is $\Delta k = -2k_p + k_s + k_i$. From a classical perspective, the process can also be expressed as sum of four waves oscillating in a common nonlinear medium, where after expanding the relevant induced nonlinear polarization $\vec{P}_{NL} = \epsilon_0 \chi^3 : \vec{E}\vec{E}\vec{E}$, and summing four of these together, one can derive a set of coupled amplitude equations that reveal the sums of individual nonlinear mixing terms, one of which concerns the four wave mixing phenomenon above, as in [39].

For the discussions in this chapter, and brevity—to relate four-wave mixing and two-photon absorption numbers to χ^3, some important parameters that are often used to discuss nonlinear include the waveguide nonlinear parameter

$$\gamma = \frac{n_2 \omega}{c A_{eff}} \tag{2.2}$$

9

where A_{eff} is the effective cross-sectional area of the waveguide mode, c is the speed of light, ω the frequency, and n_2 is the widely used Kerr nonlinear coefficienct, that leads to an intensity dependent refractive index, and is related to the real part of the third order susceptibility as

$$n_2 = \frac{3}{4\epsilon_0 c n^2} \, \mathbb{R}(\chi^3) \qquad (2.3)$$

where ϵ_0 is the permittivity of free space, and n is the refractive index. As will be used later in this chapter, a parameter that characterizes the extent of TPA is called the TPA coefficient and is related to the imaginary part of the third order nonlinear susceptibility as

$$\beta_{TPA} = \frac{3\omega}{2\epsilon_0 c^2 n^2} \, Im(\chi^3) \qquad (2.4)$$

noting that the real and imaginary parts are connected through the nonlinear Kramers-Kronig relation[42] . A direct relation to the refractive index perturbation can also be derived as

$$n = n_0 + n_2 I + i\frac{\lambda}{4\pi}[\alpha_0 + \beta_{TPA}I] \qquad (2.5)$$

where α_0 encapsulates the linear absorption, and I is the intensity of the light, showing how the TPA coefficient is numerically related to absorption and the refractive index. Some common numbers cited for silicon are 8×10^{12} m/W for the TPA coefficient and 200 W^{-1} m^{-1} for the nonlinear parameter[43], [44], compared to 1.4 W^{-1} m^{-1} for Silicon Nitride [45]. The next sections in this chapter will describe four-wave mixing nonlinearities in the context of biphoton pair generation through SFWM, and nonlinear loss from TPA and FCA in the context of high speed resonant modulators.

2.1 Spontaneous Four-wave mixing

The classical form of coupled equations from expansions on sums of $\vec{P}_{NL} = \epsilon_0 \chi^3 \vdots \vec{E}\vec{E}\vec{E}$, as noted in [39] can be reframed in terms of the electric field operators, as shown in detail in [46].

For brevity, we note here the key parts that lead to the formulas which will be used in later chapters. The goal is to show the form of the biphoton states generated by the spontaneous four-wave mixing process, so that the equation can be used later to analyze characteristics and quality of the single and entangled photons being generated through a given process and device (these properties are discussed in Chapter 6). The nonlinear coupled equations of the interacting waves, expressed through the electric field operators, show the equations of motion that result from these interactions, so the first objective is to find the interaction Hamiltonians that produce these coupled equations. Eventually, the one that matters for SFWM (seeded by vacuum state) is the four-photon scattering (FPS) interaction Hamiltonian, given as

$$H_{FPS} = \alpha \epsilon_0 \chi^3 \int dV \left(E_s^{(-)} E_i^{(-)} E_p^{(+)} E_p^{(+)} + H.c. \right) \qquad (2.6)$$

where α is an scaling constant, $H.c.$ is the Hermitian conjugate, $E_s^{(-)}$, is the negative electric field operator for the signal photon with other terms having + superscripts denoting the positive electric field operator, and i and p denoting idler and pump. Then, this interaction Hamiltonion is applied to calculate state vector evolutions for the output of the nonlinear process

$$|\Psi\rangle = |0\rangle + \frac{1}{i\hbar} \int_{-\infty}^{\infty} H_{FPS} dt \, |0\rangle \qquad (2.7)$$

where $|0\rangle$ is the vacuum state, so it is superposition of the vacuum state and two-photon state. After writing the pump field as the form of the laser serving as the pump, along with the quantized electromagnetic fields of the signal and idler written in terms of the creation and annihilation operators, and then plugging into eq. (2.7) [46], one arrives at a state vector of

$$|\Psi\rangle = |0\rangle + \sum_{k_s, k_i} F(k_s, k_i) \, a_{k_s}^\dagger a_{k_i}^\dagger |0\rangle \qquad (2.8)$$

where the function $F(k_s, k_i)$ is named the two-photon spectral function and describes the biphoton amplitude as a function of the joint signal and idler spectrum. This shows how the signal and idler

photons can be gotten from biphoton state formed by this nonlinear process and is a very useful form that will be described in further detail in Chapter 7.

2.2 Nonlinear Loss

This section will describe some of the nonlinear loss and subsequent linear free carrier absorption losses and how it impacts a high-speed silicon resonant modulator, design and experiments of which Chapter 3 will describe. Since TPA loss is power dependent, the loss along a waveguide can be calculated as

$$\frac{dI}{dz} = -\alpha_{scatt}I - \beta_{tpa}I^2 - \alpha_{FCA}I \tag{2.9}$$

where the linear scattering loss, two-photon, and free carrier absorption losses are given in α in that order. Since α_{FCA} is related to α_{tpa} through a generation factor as

$$\alpha_{FCA} = (\sigma_N \tau_N^{eff} + \sigma_P \tau_P^{eff}) \frac{\beta_{tpa}}{2h\lambda v} I^2 \tag{2.10}$$

where σ_N and σ_P can be found from the constants in [47] for hole and electrons and τ's are their respective lifetimes, the equation can be integrated along the length of the device to find the final intensity and the loss [48].

For a time dependent loss from TPA, in modeling a dynamic system (i.e. resonant modulator) we can write a time dependent losses from [49] as

$$\gamma_{TPA}(t) = \Gamma_{TPA} \frac{\beta_{Si}}{V_{TPA}n_g^2} U(t) \tag{2.11}$$

$$\gamma_{FCA}(t) = \frac{\sigma_{Si}c}{n_g} N(t) \tag{2.12}$$

Effects on a resonant microring modulator

Now we will relate the losses to the behavior of a resonant microring or microdisc modulator. The equations of motion for the field inside a microresonator [50] are

$$\frac{da}{dt} = \left(\frac{-\gamma_{Total}}{2} + i(\Delta\omega + \Delta\omega_{laser} - \Delta\omega_{cold})(a_u + ia_v) + i\kappa(\sqrt{Pin})\right) \tag{2.13}$$

$$\frac{dT}{dt} = -\gamma_{th}T + \frac{\Gamma_{disk}}{\rho_{Si}Cp_{Si}V_{disk}}P_{abs} \tag{2.14}$$

$$\frac{dN}{dt} = \left(-\gamma_{r\_fc}N + \frac{\Gamma_{FCA}\beta_{Si}c^2}{2\hbar\omega_{laser}n_g^2V_{FCA}^2}U^2\right) \tag{2.15}$$

$$\frac{dV_{pn}}{dt} = \left(-\frac{V_{pn}}{\tau_{RC}} + \frac{V_{applied,PRBS}}{\tau_{RC}}\right) \tag{2.16}$$

$$\frac{\Delta\omega}{\omega_0} = \left(-\frac{1}{n_{Si}}\right)\left(\frac{dn_{Si}}{dT}\Delta T(t) + (\frac{dn_{Si}}{dNp} + \frac{dn_{Si}}{dNn})\Delta N(t)\right) + \frac{\Delta\omega_{0,mod}(t)}{\omega_0} \tag{2.17}$$

$$\Delta\omega_{0,mod}(t) = \left(\frac{d\omega_0}{dV_{pn}}V_{pn}(t) - V_{bias}\right) \tag{2.18}$$

$$\gamma_{Total} = \gamma_{TPA} + \gamma_{FCA} + \gamma_{lin} + \gamma_0 + \gamma_{rad} \tag{2.19}$$

$$U = |a_u + ia_v|^2 \tag{2.20}$$

$$P_{abs} = \gamma_{Total}\,U \tag{2.21}$$

where Γ_{disk} is the fractional energy overlap of the optical mode with the temperature within the silicon resonator, γ_{r_fc} is the free-carrier decay rate accounting for recombination and diffusion. $\gamma_{Total}, \gamma_{TPA}, \gamma_{FCA}, \gamma_{lin}, \gamma_0, \gamma_{rad}$ are the total losses: loss from TPA, loss from FCA, linear loss in the waveguide, loss from the designed coupling coefficient, and radiative loss from the bent mode. $\Delta\omega$ is the frequency shift determined in eq. (2.17), $\Delta\omega_{laser}$ is the shift in the position of the laser frequency relative to the initial laser frequency, and $\Delta\omega_{cold}$ is the difference between the frequency of the initial laser frequency and initial resonance frequency of the resonator. a_u and a_v are the real and imaginary parts of the circulating field, κ is the coupling coefficient, Pin

is the optical power in the input waveguide bus, γ_{th} is the thermal loss, V_{disk} is the disk mode volume, Γ_{FCA} is an overlap integral of the field in silicon normalized to the total field volume which is a modal confinement factor, V_{TPA}, V_{FCA} are effective mode volumes, U is the internal cavity energy V_{pn} is the voltage across the PN junction, τ_{RC} is the RC lifetime, $V_{applied,PRBS}$ is the applied input voltage, e.g. a pseudorandom bit sequence (PRBS), $\frac{dn_{Si}}{dT}$, $\frac{dn_{Si}}{dNp}$, $\frac{dn_{Si}}{dNn}$, are the changes in index caused by temperature, and hole and electron changes, respectively, and $\frac{d\omega_0}{dV_{pn}}$ is the modulation efficiency.

Setting the input as a PRBS, the model captures the wavelength direction in which the laser is increased into the resonance of the resonator and the shifts that it causes due to the bistability caused by the nonlinear losses and power dependence. This is shown in Fig. 2.2 from an coupled ordinary differential equation solver run in MATLAB, showing how the resonance of the ring is modulated by the voltage, but is shifted by the buildup in internal circulating power as the laser is walked on to the resonance of the ring from a specific direction in wavelength.
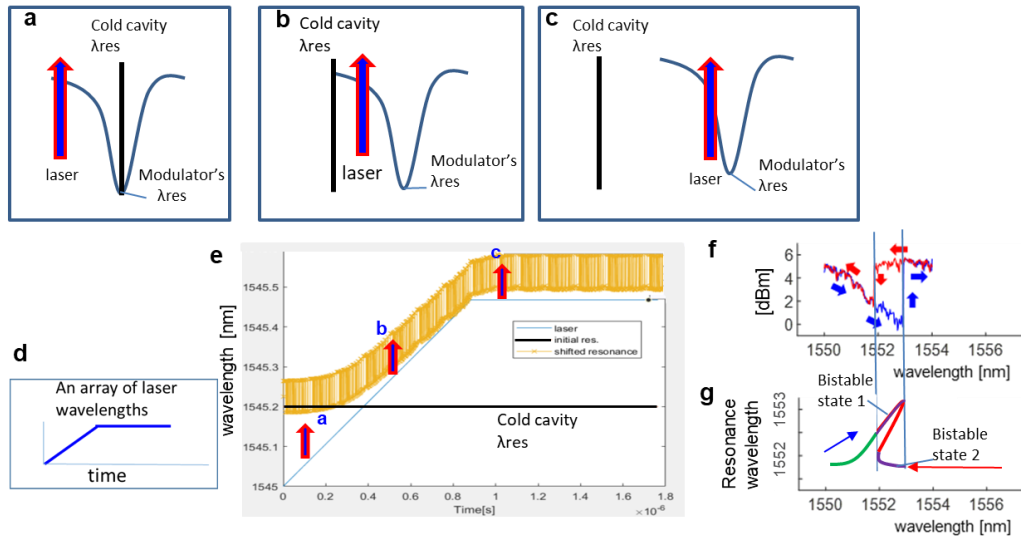
Figure 2.2: (a) Cartoon drawing showing the position in wavelength of the laser at the beginning of the simulation. (b) Cartoon drawing showing the position in wavelength of the laser at time "b" of the simulation. (c) Cartoon drawing showing the position in wavelength of the laser at time "c" of the simulation. (d) Cartoon of laser ramp, increasing in wavelength as time increases. (e) Screen capture of resonance shifts in simulation time. (d) measure data of resonator transmission from different directions of laser wavelength sweeps. (g) Diagram of location of possible resonator resonance wavelengths, showing the regions of bistability.
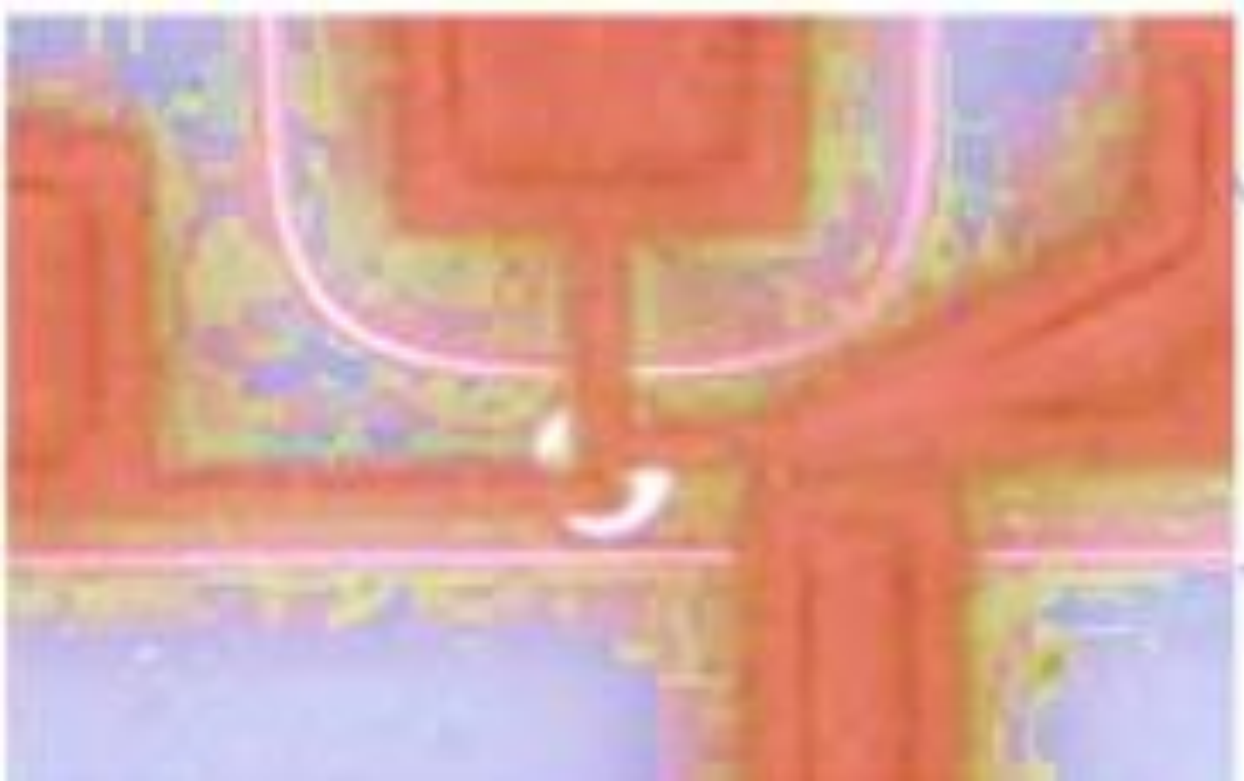
"An Impressionist rendering of a Disc Modulator under high optical power." art by Xiaoxi Wang

Chapter 3

High-speed silicon microresonator modulators with high optical modulation amplitude

The nonlinear, power dependent loss described in the previous chapter and the formulations of the coupled differential equations describing the equations of motion are used in this chapter to design a power efficient resonant modulator that can handle higher input powers than previously shown in resonant micro-scale modulators. A high-speed silicon photonic microdisc modulator is used with more than 10 mW optical power in the bus waveguide, extending the optical power handling regime used with compact silicon resonant modulators at 1550 nm. This chapter presents a design and experimental study that complements the modeling described in the previous chapter. We discuss the wavelength tuning range and biasing path required to shift the resonant frequency to the optimal point versus on chip power. We measure the optical modulation amplitude (OMA) along different biasing trajectories of the microdisc under active modulation and demonstrate an OMA of 4.1 mW with 13.5 mW optical power in the bus waveguide at 20 Gbit/s non-return to zero (NRZ) data modulation.

3.1 Overview

Carrier-depletion silicon photonic microresonator modulators are used as compact, energy-efficient electro-optic modulators for data communications, optical switching, and RF photonics [51]–[55]. One limitation of such devices at present is their optical power-handling capacity. Integrated semiconductor lasers can now efficiently generate and deliver more power in the bus waveguide than the sub-milliwatts of optical power that are typically used with silicon microresonator modulators [56], [57]. Such devices lose the ability to adequately modulate light at higher power levels because of a combination of effects including two-photon absorption (TPA), free-carrier generation (FCA), and a thermo-optic shift of the refractive index [43], [58]. Impaired

17

performance at higher power levels under-utilizes critical resources in an optical communication system and decreases the link transmission distance.

For the popular NRZ (non-return to zero) modulation format, the OMA (Optical Modulation Amplitude) is defined as the difference (P1-P0) between the average power level for the 1 and 0 bits. Sometimes, the normalized OMA is reported as (P1-P0)/Pin where P1 is the average high bit value, P0 is the average low bit value, and Pin is the input power before the modulator. OMA is a key parameter used in short-distance serial communications [59], [60], and is used as the figure-of-merit in this report. OMA is related to other quantities such as bit error rate (BER) and optical extinction ratio (ER) which are used to describe communication systems [61, p. 3], [62].

As the input optical power level to a silicon microresonator modulator increases, the OMA first increases, and then rapidly decreases because of the inability of the microresonator to modulate high optical powers. As shown in Fig. 1, the output light is modulated by the resonator because of the voltage-driven interference between the fraction of the input which does not couple into the resonator, and the fraction of the input which does couple into the resonator and experience an amplitude and phase shift before effectively coupling back out into the bus waveguide. At higher optical power, further amplitude and phase changes caused by nonlinear effects giving rise to optical waveform distortions have to be balanced by changing the fraction of input light that is coupled into it, i.e., the coupling coefficient or, equivalently, the bias condition. Note that in the devices studied here, the optical intensity in the resonator is significantly larger than in the bus waveguide, since the value of finesse (F, defined as the ratio of the free spectral range to the full width at half maximum) is as high as 245 at low power and 186 at the higher power level associated with the highest measured OMA. Thus, we still operate in a regime where resonant effects are

significant, and substantially (by approximately a factor of F/2) lower the electrical power consumption of a microresonator modulator relative to a traveling-wave Mach-Zehnder modulator, as has been studied extensively elsewhere [63, p. 56].

We study the trends observed at a data rate of 20 Gbit/s NRZ format digital modulation using a silicon photonic microdisc modulator operated near 1550 nm. We compare the trends at high data rates with slower 0.2 Gbit/s data rates, covering the different time scales with respect to the carrier dynamics in silicon [5]. An OMA of 4.1 mW was obtained at an optical power level of 13.5 mW (11 dBm) without using pre-emphasis or frequency shaping on the electrical driving waveform. Our results demonstrate a much higher OMA for electro-optic data modulation using silicon microdisc resonators at 1550 nm, which are usually operated with lower optical power levels (see Table 1). Given a certain data modulation rate and detection sensitivity (minimum detector power required to achieve a certain bit error rate), a higher OMA directly translates into increased distance between the source and the destination. This can be critically helpful in improving the reach short-distance communications without using optical amplifiers or repeaters, or providing additional link margin for incorporation of optical switches or other devices. A small increase of the OMA from 0.3 mW [8] to 0.38 mW, for example, can result in increasing the transmission distance by 5 km before dispersion impairments, based on a propagation loss coefficient in fiber of 0.2 dB/km, and a free space optical link can also benefit in a similar way. If the need for optical amplifiers can be avoided, the bandwidth span of wavelength-division multiplexed (WDM) communications can be increased. This is a problem for short-distance optical communications such as unamplified ultrawideband WDM links which anticipate using a wider spectral range than the gain bandwidth of amplifiers [64]. The results shown here on increased

OMA for high-speed silicon photonic microdisc modulators may benefit unamplified wideband WDM optical networks, among other applications.

3.2 Device Details

The modulator is a vertical PN junction microdisc, operated in carrier depletion mode under reverse bias, similar to [65], as pictured in Fig. 3.1(a). The modulator was partially doped so that dopants covered approximately one-half of the disc circumference. The microdisc diameter is 4 □m, giving a free spectral range (FSR) of about 59 nm, so that there is only one resonance in the C-band (and only one resonance in the L-band). Dopant levels were selected with sufficient bandwidth for 25 Gbit/s NRZ modulation, with the only difference among different test structures being the waveguide-to-resonator gap. The waveguide-to-resonator gaps were designed to be 280 nm for one design, while another design used 260 nm for a slightly larger waveguide-resonator coupling coefficient. The silicon photonic fabrication was performed in a multi-project wafer process at Sandia National Laboratories [66]. The VπL of our vertical PN was measured to be 1.25 V-cm, extracted from the resonance shift relative to the FSR, in a method like the one performed in [67].

Figures 3.1(b)-(e) show optical transmission spectrums measured with high resolution for the disc with a coupling gap of 280 nm, from low optical powers where resonator spectrum asymmetry is absent (panel b), to high optical powers where there is strong nonlinearity and a large bistable regime (panel e). Based on the measured transmission at low powers, loaded quality factors of 6200 were inferred. To generate the plots in Figure 3.1(c)-(e), a continuous wave (C.W.) laser was stepped from lower wavelength to higher wavelength at a tuning speed of 0.25 s per step

(blue), and then stepped in reverse from higher wavelength to lower wavelength at the same speed (red).
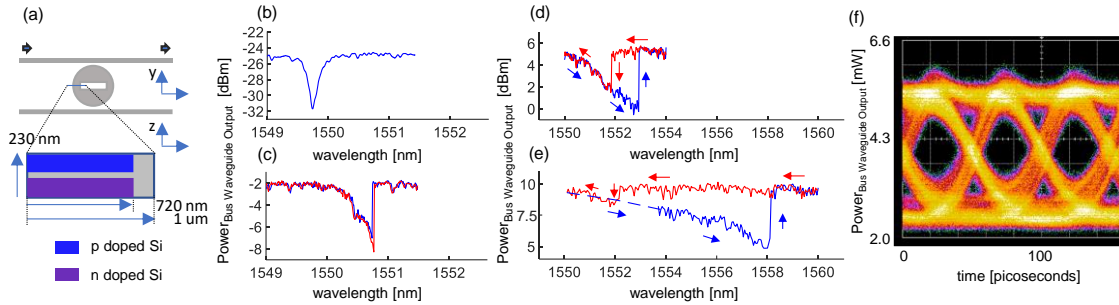
Figure 3.1: (a) Schematic of a microdisc modulator coupled to two bus waveguides. (b)-(e) Transmission spectrum as the on-chip optical power is increased. The blue and red lines show the measurements when scanning the laser in opposite directions. (f) 20 Gbit/s eye diagram measured on an optical sampling oscilloscope; y-axis is the optical power in the bus waveguide after the modulator.

3.3 Experiment

For high-speed OMA measurements, the tunable C.W. laser was used again as the source. For on-chip optical powers (in the bus waveguide) less than -2 dBm, no external optical amplifier was used. A polarization maintaining erbium doped fiber amplifier (EDFA) was used to achieve on-chip optical powers greater than -2 dBm. Polarization-maintaining fiber arrays were used to couple light to the chip. At low powers, the total (fiber to fiber) insertion losses through the chip was measured to be 9.8 dB. A high-speed arbitrary waveform generator (Tektronix AWG70000 series) was used to generate the pseudo-random bit sequence (PRBS7) pattern which drives the modulator. The electrical signal from the AWG was amplified to 3.2 Vpp using a high-bandwidth RF amplifier (Keysight N4985A 50 GHz Microwave Amplifier), and a high-speed bias T was used to apply a reverse bias of -3.25 V. At the output, a fiber-coupled C band filter with bandwidth about 100 GHz was used to filter out the ASE noise before detection.

Optical transmission was measured by capturing the optical trace on the oscilloscope and analyzing the waveform using software (MATLAB). A section of a representative trace is shown in Fig. 3.2 (c), (f), (i), and (l). Since the optical oscilloscope was not equipped with a bit-error rate tester, the conventional sampling mode cannot determine when a bit error occurs, and so cannot distinguish a high "1" bit from a "0" that has been distorted to a high optical power level. Therefore, we post-processed the acquired data in MATLAB, by folding over the traces for over 1000 bit periods, such as shown in Fig. 3.2(c), and also obtaining an eye diagram as in Fig. 3.2(e). As a check, these post-processed eye diagrams were seen to be similar to those captured using the conventional sampling mode of the oscilloscope (Fig. 1(f) for 20 Gbit/s NRZ modulation).
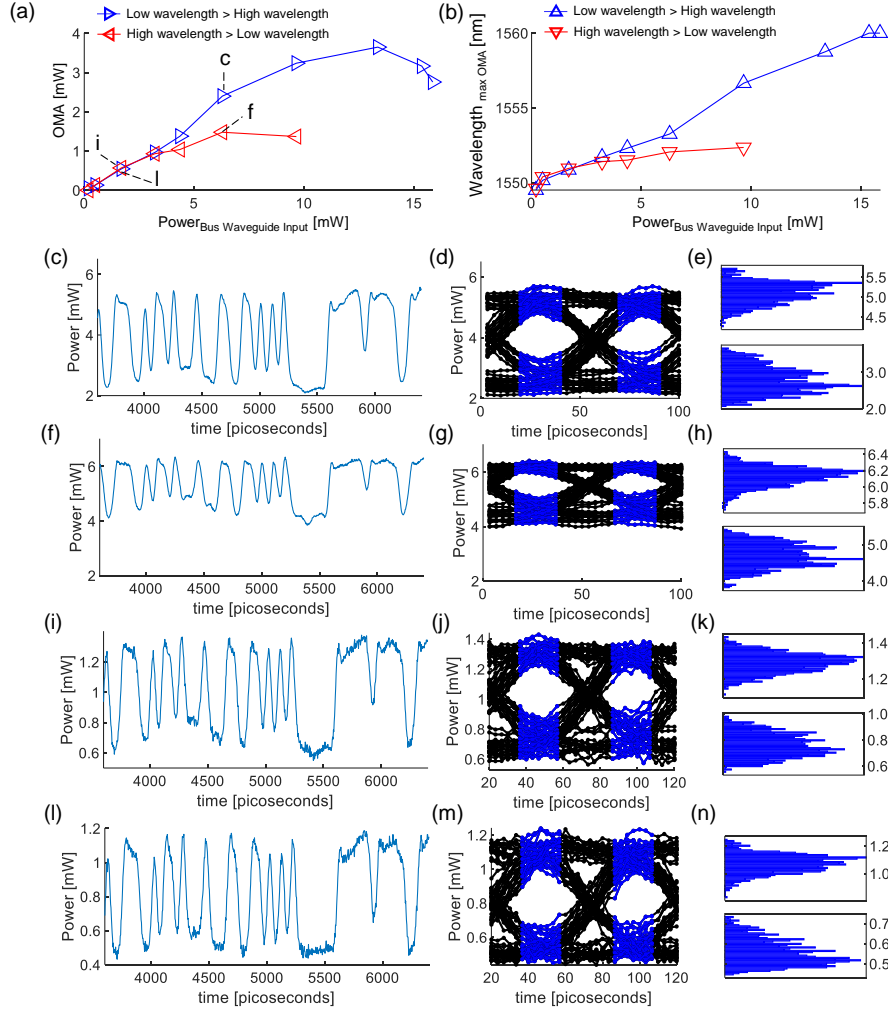
Figure 3.2: (a) OMA vs. optical power in the input bus waveguide, at 20 Gbit/s NRZ modulation while stepping the laser from lower wavelengths to higher wavelengths (blue points and line), and higher wavelength to lower wavelength (red markers and line). The labels "c", "f", "i", and "l" indicate points which refer to subplots with the same label. (b) Wavelength at which the optimal OMA was achieved. (c), (f), (i), (l) A portion of the time-domain waveform corresponding to the points labeled 'c', 'f', 'i' and 'l', respectively, in panel (a), with 6.3 mW bus waveguide input power for (c) and (f), and 1.7 mW bus waveguide input power for (i) and (l). (d), (g), (j), (m) A binary-mode eye diagram was constructed by folding and overlaying the traces in panels (c), (f), (i) and (l), respectively, across each bit period. The regions shown in blue are the sampling points from which the OMA was calculated. (e), (h), (k), (n) Histograms for the logical "1" and logical "0" bits at the sampled points which used to calculate the OMA.

To find the OMA of the disc modulator, the optical power level in the bus waveguide after the device was calculated. The insertion loss from the output coupling, fibers (1.26 dB), and filter (1.34 dB) was subtracted from the raw measurements to give the OMA values shown in Figure 3.2. The oscilloscope data from each eye diagram was processed in MATLAB to sample the center

of the eye, i.e., collecting all the datapoints shown in blue in Fig. 3.2 (d), (g), (j), and (m). To determine if the correct sequence of "1" and "0" bits was detected, a pattern match to the PRBS7 waveform was performed in MATLAB. The sampled measurement points were assigned to their respective bit as logical "1"s or "0"s. All sampled optical power levels corresponding to a logical "1" were histogrammed and contributed to the "1" level power used to calculate the OMA, and all sampled optical power levels corresponding to a logical "0" contributed to the "0" level power for OMA calculation, as shown in Figure 3.2 (e), (h), (k), and (n). An average was taken for each histogram and the OMA was calculated by subtracting the mean optical power value of the logical "0" bits from the mean optical power value of the logical "1" bits.

This process was repeated for each input optical power level in the range of 0.2 mW to 15.9 mW, and at each wavelength of the laser scans. To find the best OMA that could be achieved at a given optical input power, the tunable laser was scanned from a wavelength that was a few nanometers lower than the cold-cavity resonance wavelength of the disc by increments of 0.1 nm until near resonance, and then incremented by 0.025nm until the laser wavelength is past the resonance to a few nanometers further. For each step, the ASE noise filter was programmed to follow the wavelength of the laser. The laser wavelength was then stepped backwards (from high wavelengths to lower wavelengths) to the starting point, and the oscilloscope data was saved and processed. The highest OMA across the wavelength scans was chosen for the plot shown in Fig. 3.2(a). At the same time, the biasing wavelength was plotted in Fig. 3.a(b). We verified that waveforms where the logical "0"s (or, equivalently, "1"s) are distorted to the point that they cross the middle threshold of the eye and would be incorrectly sampled as "1"s are not used to calculate the optimal OMAs, since these waveforms cannot contribute to error-free communications [67].

3.4 Results and Discussion

From Figure 2(a), we saw that the OMA increases with increasing optical power in a sub-linear fashion, up to a certain maximum value, and then decreases. At lower data rates (0.5 Gbit/s), such behavior has been attributed to the combined effects of two-photon absorption, free carrier absorption, and free carrier dispersion growing nonlinearly stronger at increasing optical power [5] and similar effects are also present at 20 Gbit/s but are manifest differently due to the different relative time scales of the data modulation and free carrier dynamics. To compare lower speed dynamics with 20 Gbit/s behavior, we performed a slower speed experiment to extract the OMA behavior versus optical power at data rates of 200 Mbit/s. Interestingly, the OMA of the slower 200 Mbit/s data rate was limited to below 1 mW. Typical free carrier lifetimes in silicon waveguides can be on the order of hundreds of picoseconds to a few nanoseconds whereas the thermal time constants are usually on the order of a few hundred nanoseconds to microseconds [68], [69]. At the higher data rates, the effects of nonlinearities at higher power are pattern-dependent, and the distortions from ideal "1" and "0" levels will become most evident for a long string of bits. In principle, this can be mitigated by run-length encoding, although no coding was performed in the experiments reported here. At the slower data rates, the distortions from bit to bit are themselves stronger and cannot be mitigated by coding.

3.4.1 OMA comparison between low-speed and high-speed NRZ data modulation

To demonstrate this difference in behavior of eye closure due to high optical power at 20 Gbit/s versus 200 Mbit/s, we plot the time domain waveforms in Figure 3.3(c), (f), (i), and (l) for the identical bit sequence over a longer span of bits. For 20 Gbit/s, Figure 3(f) shows the onset of

eye closure, and the difference between it and Figure 3.3(c) (an optimal OMA point) is clearly due

to pattern dependence, over a time span of a few nanoseconds, denoted by Δf1. In contrast to 20

Gbit/s data, Figure 3.3(l) shows that the onset of eye closure for 200 Mbit/s data is very different

for each bit, but also on the order of a few nanoseconds, denoted by Δl1.
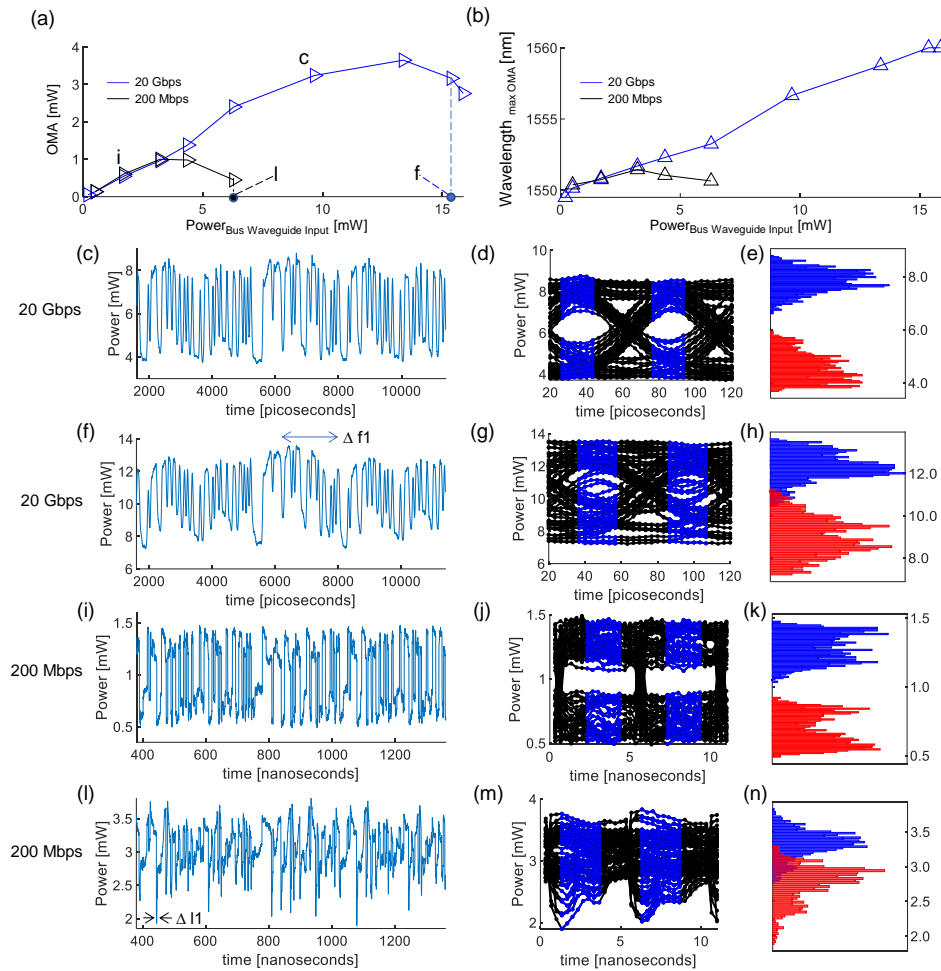
Figure 3.3: (a) OMA vs. optical power in the input bus waveguide, at 20 Gbit/s NRZ and 200 Mbit/s NRZ; the markers "c", and "i", correspond to panels (c) and (i), respectively. "f" and "l" represent measurements at wavelength biases which eye closure would result, due to "1" ("0") bits being incorrectly sampled as "0" ("1") for every PRBS7 sequence. They do not contribute to the error-free OMA, and are plotted in panels (f) and (l) to show the onset of eye closure. (b) Wavelength at which the optimal OMA was achieved. (c), (f) A portion of the time-domain waveform at the optimal bias wavelength when the optical power in the input bus waveguide was 9.7 mW [panel (c)] and 15.4 mW [panel(f)]. (i), (l) Plots similar to panels (c) and (f), for 200 Mbit/s modulation, at input power levels of 1.7 mW [panel(i)] and 6.3 mW [panel(l)]. (d), (g), (j), (m) A binary-mode eye diagram was constructed by folding and overlaying the traces in panels (c), (f), (i) and (l), respectively, across each bit period. The regions shown in blue are the sampling points from which the OMA was calculated. (e), (h), (k), (n) Histograms for the logical "1" and logical "0" bits at the sampled points which used to calculate the OMA. Different colors are used to show the overlap, if it occurs.

26

Figures 3.3(a) and 3.3(b) summarize the major differences between higher data rate 20 Gbit/s waveforms and slower 200 Mbit/s with respect to increasing optical power. The 200 Mbit/s waveforms do not reach the higher OMA values achievable at 20 Gbit/s modulation. Because each bit and shorter (in lengths of bits) bit sequences of the slower waveforms distort strongly compared to the change in average power, one must detune the bias further (in the direction of decreasing wavelength) with respect to the shift in resonance wavelength caused by the increasing average power. This was observed in the models from [5], and is shown here in Fig 3.3(b): the black line denoting the optimal wavelength is not monotonic and decreases at the point where the OMA also starts to decrease. However, for the 20 Gbit/s modulation, the differences between unique segments of longer runs of pattern are smaller, and longer pattern difference cause eye closure. The difference between average power from distortion causing pattern segments is also less. The bias point does not need to be detuned as far to get to the optimal OMA, and so the optimal bias wavelength keeps increasing with the power as shown by the blue line in Fig. 3(b).

3.4.2 Biasing

To summarize the observations made in the previous section when discussing the OMA trends, at each optical power level in the nonlinear regime, the ideal biasing point of a microdisc modulator is (slightly) different in order to achieve the highest OMA. Figure 2(b) shows this behavior using a shift of the wavelength of the input laser. While keeping the modulator's on-chip thermal shifter at a constant voltage and temperature, and keeping the chip mount thermoelectric-cooler (TEC) at a constant temperature, the laser was stepped from a wavelength shorter than the cold-cavity resonant wavelength to a wavelength longer than the resonant wavelength, and then stepped backward.

27

Figure 3.22(b) shows that the optimal biasing point for the highest OMA changes from 1549.5 nm to 1556.7 nm across a span of below 1 mW to near 10 mW of optical power in the input bus waveguide and grows to 1558.8nm before the highest OMA is reached, a span of nearly 10 nm. The biasing trends for the slower data rate, Fig. 3.3(b), are different. There is a decrease in optimal biasing wavelength when the peak OMA is reached and then starts to decrease with increased power, due to the response times of the nonlinearities giving rise to the distortions as noted in the prior section. In these cases, the laser needs to be detuned further away (i.e., remain at lower wavelength and not bias closer to resonance) from the resonant frequency since the impact of the single bits and shorter bit sequences on eye-closing distortion is large, while the slower thermal shift towards longer wavelength continues. This may result in an inability to reach the wavelength at which the strongest resonant peaking in the modulation response occurs (i.e. $\omega_m=\omega_r-\omega_0$, where ω_m, ω_r, ω_0 are the modulation, resonator, and laser bias frequencies, respectively [7]). On the other hand, for the higher data rate modulation, one does not need to detune as much to reach the optimal OMA, since eye closure results from the cumulative effects of a much longer string of bits, which, by pseudorandom nature, has less variation from sequence to sequence. In other words, the timescale of change in optical power due to power dependent nonlinearities is much slower than timescale of bit "0" to bit "1" differences, so the bias wavelengths, at which the eye closes, tracks the resonance wavelength shifts due to increasing power more closely.

3.4.3 Direction of bias scan

When searching for the optimum bias point in the nonlinear regime, it is important to note that shifts to higher and lower wavelengths (or equivalently, to lower or higher reverse-bias voltages) can have asymmetric effects. Figure 3.2(c)-(f) shows scans in wavelength from a lower

wavelength to a higher wavelength), followed by a reverse-direction scan. These plots show the extent of wavelength tuning required to approach the optical power-dependent resonant wavelength in each direction. Figure 3.2(a) shows the maximum OMA that can be reached from the shorter-to-longer wavelength scan (shown by the blue left-to-right arrows), as well as the best OMA that can be reached returning to the initial wavelength with a decreasing-wavelength scan. As previously discussed [5], [70], the optimal operating conditions in a regime that is characterized by the bistable behavior of the resonator are found by scanning the laser from lower to higher wavelength. Figure 3.2 shows how the bistable regime grows with increasing optical power. At 10 mW of input power, the region of bistability is wide, and requires nearly 6 nm of wavelength shift or an equivalently large tuning of the temperature controller. In the measurements reported here, the optimum bias point was found through post processing, after the measurements were performed. An automated controller would search for the optimum bias point by exploring both sides of the resonance using a systematic trajectory, rather than blind bidirectional searching. Abruptly turning on a laser, as opposed to a swept-initialization case, can result in two impairments: (i) the loss of the ability to track the resonance and achieve the highest OMA or ER, and (ii) may result in self-modulation due to the interplay of heating and free-carrier dispersion over a range of the bias conditions. The development of a practical and robust bias controller in the high-power regime is an important future goal in this topic.

3.4.4 OMA Improvements

As the optical power increases, the loss inside the resonator also increases from the increase of free carrier absorption induced by TPA. In a microdisc resonator that was designed to be at critical coupling for optical power levels where TPA is low, at higher optical power when the

round trip loss is higher, the resonator becomes more under-coupled since the self-coupling (or through transmission) coefficient of the directional coupler between the bus waveguide of the resonator becomes larger than the roundtrip amplitude coefficient that describes the amplitude change in propagating through one round trip around the circumference of the microdisc [71]. The extinction ratio will then become smaller, and the OMA will decrease with increasing optical power, even if distortions from nonlinear power induced resonance shifts do not fully close the eye. This also means that a disc designed to be slightly over-coupled at low optical power may move closer to critical coupling when the optical losses in the resonator increase at higher optical power, and the extinction and OMA will improve.

We verify that a microdisc that is more over-coupled at low optical powers will have higher OMA at high power through a time-domain simulation in MATLAB following the methodology shown in [5], [50] which captures the nonlinearity-induced bistability behavior of the microdisc modulator. Figure 3.4 shows this effect on two microdisc resonators that are identical except for the bus-waveguide to resonator coupling gap. Figure 3.4(a) shows the result of our simulation using a 20 Gbit/s PRBS7 NRZ modulation, where the OMA is plotted versus input optical power, relative to its value at 10 mW input power. We observe that the OMA of datapoint "a2" is higher than datapoint "a1" by about 0.4 mW. The plot in Figure 3.5(b) shows the low-power static transmission response, with the initially over-coupled (at low power) disc having a power coupling coefficient, $|\kappa_2|^2$, 1.5 times larger than the coefficient of the critically coupled (at cold cavity) disc, $|\kappa_1|^2$. The power coupling coefficients are related to the time domain coupling coefficient, μ_1 and μ_2, of our time domain simulation as discussed in [72], and were fitted from the fabricated and measured devices, as discussed next.

Figure 3.4(c)-(d) shows the experimental results of two measured devices, identical except for the coupling gap. Figure 3.4(d) shows that the modulator with a 260 nm gap between the disc and the bus waveguide has a full-width-half-maximum (FWHM) of 42 GHz and Q of 4,500 and is slightly more over-coupled than the disc with a 280 nm gap, which has a FWHM of 31 GHz and a Q of 6,200. The extinction of the disc with 280 nm gap is also slightly larger. This results in the smaller gap disc showing a smaller change in transmission for a given voltage swing, or equivalently, for the same change in resonant wavelength, less change in transmission and a smaller modulation efficiency. This results in the smaller-gap, relatively over-coupled disc having smaller OMA at lower optical power. However, at higher power, the larger gap disc shows a larger decrease in extinction ratio at higher power and the OMA of the smaller-gap disc is higher than the OMA of the larger-gap disc at larger input optical powers, and is about 0.5 mW higher at the highest OMA points which are marked by the points "f" and "e" in Fig. 3.4(c). We measured 4.1 mW OMA at an input power of 13.5 mW. In agreement with the simulations, our measurements show that the disc with the smaller waveguide-resonator gap shows a more open eye diagram at higher optical powers. This device also shows a lower modulation loss (sum of insertion loss and excess modulation loss) of about 0.5 dB at point "f" (compared to about 1.5 dB of modulation loss for the 280 nm gap disk at point "e"), and a slightly higher extinction ratio of about 3.1 dB (compared to an extinction ratio of about 2.9 dB for point "e"). At lower optical powers, a silicon microring modulator operated at 25 Gbps was seen to have an excess modulation loss on the one level of approximately 3 dB, while achieving sub volt VπL [67]—trading off loss for increased dopant concentration can be used to increase modulation efficiency.
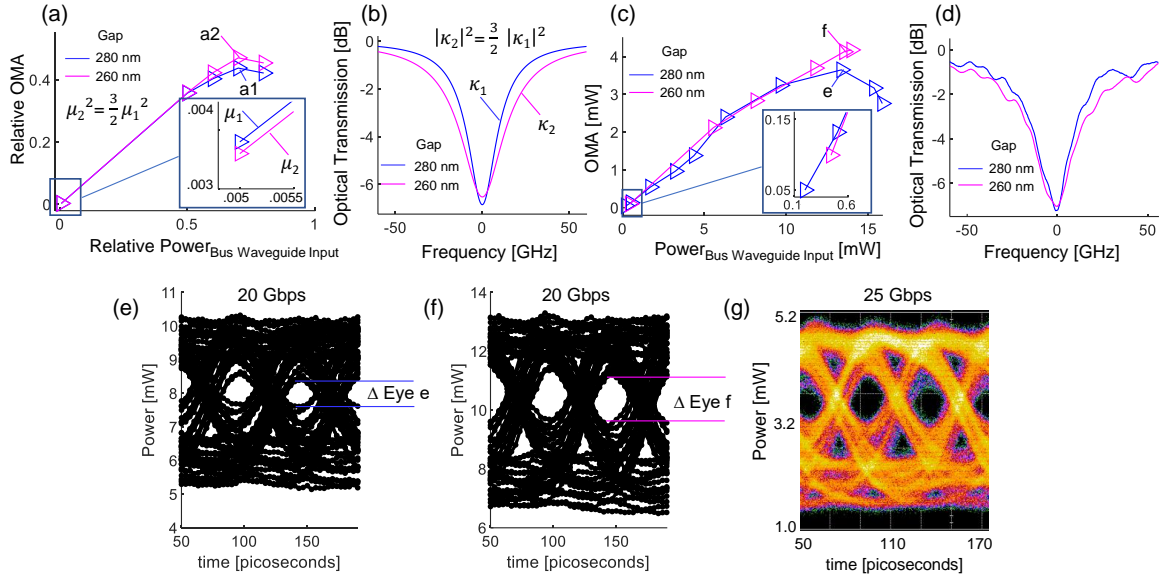
Figure 3.4: (a) Simulated OMA vs. optical power in the input bus waveguide for two discs, normalized to an input power of 10 mW. μ_1 and μ_2 are the waveguide-disc time-domain coupling coefficients of the two discs. The inset shows that the over-coupled disc (μ_2) has lower OMA at low power. The difference between the OMA at high power marked by "a1" and "a2" is about 0.4 mW. (b) Fitted transmission spectrum at low power for the two discs, where κ_1 and κ_2 are the field amplitude coupling coefficients. (c) Measured OMA vs. optical power in the input bus waveguide, at 20 Gbit/s NRZ of the two discs. The inset shows that the OMA of the 260 nm gap disc is lower at low power, in agreement with simulations. (d) Measured transmission at low power, sweeping the tunable laser from lower to higher wavelength. (e) Time-domain waveform measured on an oscilloscope of the 280 nm gap disc, folded by an integer number of the period in a post-processing step to show the extent of eye closure at 20 Gbit/s, at high optical power for the measurement point marked in Fig. 5(c). (f) Time-domain waveform of the 260 nm gap disk, at high optical power. The eye is more open and the difference between the minimum "1" and maximum "0", labeled as "Δ Eye f", is about twice as large as "Δ Eye e". (g) A 25 Gbit/s NRZ eye diagram measured for the 260 nm gap disc at higher optical powers with 12,000 points per waveform over 1,050 captured traces. The disc with the 260 nm gap can support higher data rates when the optical power is increased. The optical power shown is the power in the output bus waveguide after the modulator, when the input power in the bus waveguide was 6.3mW, and the OMA was measured to be 2.2 mW.

Higher OMA, extinction, and less eye closure at higher optical powers for the 260 nm gap disk results in a more open eye diagram at an increased data rate of 25 Gbit/s, shown in Fig. 3.4(g). The optical power shown is the power in the output bus waveguide after the modulator, when the input power in the bus waveguide is 6.3mW, and the OMA is measured to be 2.2 mW.

3.5 Simulation of power dependence

From the model discussed in section 2.2, simulations are run to show the effect of optical power loading from the nonlinearities in the resonator. Fig 3.5 shows a comparison of the dramatic effects on the optical waveform at lower speeds. Figure 3.6 shows the effects at 20 Gbps, and the simulated closure of the eye at 20 Gbps.
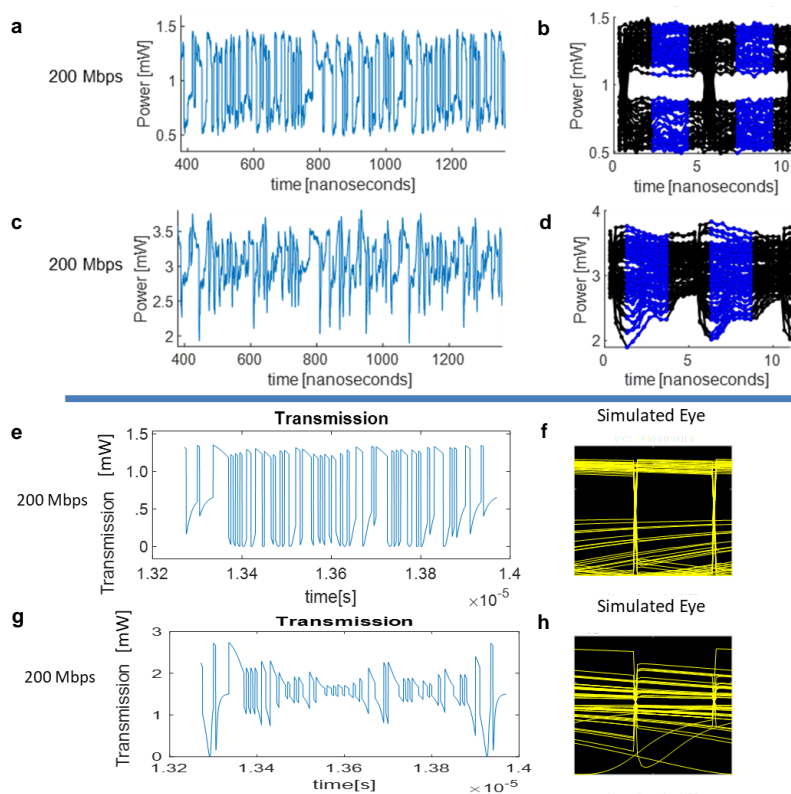
Figure 3.5: (a) Measured time domain waveforms at 200 Mbps at around 1.5 mW input power. (b) Corresponding eye diagram to (a). (c) Measured time domain waveforms at 200 Mbps at around 3.5 mW input power. (d) Eye diagram for (c). (e) Simulated time domain waveforms at 200 Mbps at around 1.5 mW input power. (f) Corresponding eye diagram to (e). (g) Simulated time domain waveforms at 200 Mbps at around 3.5 mW input power. (h) Eye diagram for (g).
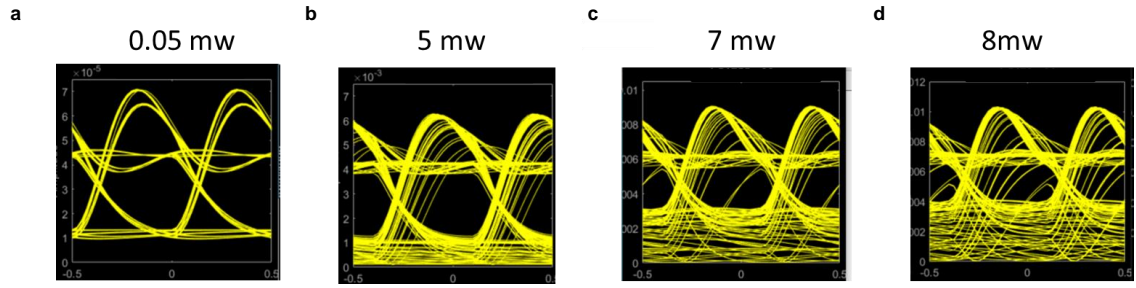
Figure 3.6: Simulated Eye diagrams (optical resonant peaking is present) for 20 Gbps waveforms at (a) 0.05 mW, (b) 5 mW, (c) 7 mW, and (d) 8 mW of input power.

3.6 Summary

We study the OMA in absolute units of Watts rather than normalized to an input value, and a list of previously reported OMA's in absolute values is given in Table 1. We prefer to report OMA in absolute rather than in normalized units, since it directly corresponds to link range in an unamplified communications link. However, in many reports, the OMA is absolute units is not available and reported OMAs are instead normalized to the input power, as (P1-P0)/Pin where P1 is the average high bit value, P0 is the average low bit value, and Pin is the input power before the modulator. A list of normalized OMA's is given in Table 2. Previously at 20 Gbit/s, an OMA of 0.47 normalized to the input power was reported [73]—while the input power level was not stated in that reference, the normalized OMA's from the OMA's in absolute power shown in Fig. 4 (a) range from 0.38 at input powers up to 6.3 mW, to 0.27 at the higher OMA's beyond 10 mW, and are comparable to state-of-the-art resonant modulators [70], [74].

34

Table 1. Optical Modulation Amplitude of resonant silicon photonic modulators

Modulator type	Modulation Speed	OMA	Input Power in W.G. Bus
Single ring [6], [75]	30 Gbit/s	0.31 mW	0.6 mW
Single ring [7]	32 Gbit/s	0.63 mW	0.8 mW
Single ring [8]	25 Gbit/s; 14 Gbit/s	0.30 mW; 0.21 mW	1.2 mW
Single ring [5]	500 Mbit/s	1.1 mW	2.6 mW
Single disc [This work]	*25 Gbit/s; 20 Gbit/s*	*2.2 mW; 4.1 mW*	*13.5 mW*

Table 2. Normalized Optical Modulation Amplitude of resonant silicon photonic modulators

Modulator type	Modulation Speed	OMA (Norm.)
Single ring [74]	112 Gbit/s (PAM4)	0.22
Single ring [76]	25 Gbit/s	0.26
Dual ring [77]	20 Gbit/s	0.30
Dual ring [78]	20 Gbit/s	0.10
Dual ring [73]	20 Gbit/s, 10 Gbit/s	0.56; 0.47
Single disc [This work]	*25 Gbit/s; 20 Gbit/s*	*0.27*

We have shown that a silicon microdisc modulator can achieve an OMA of greater than 4 mW at 13.5 mW of optical power in the bus waveguide at a data rate of 20 Gbit/s (NRZ modulation format) at wavelengths near 1550 nm. Simulations were performed to support the explanations for the differences in OMA versus input power trends that were observed at low (200 Mbit/s) and high (20 Gbit/s) modulation speeds, as well as coupling differences. A substantial wavelength shift, or an equivalent shift of the bias point using thermal or bias voltage tuning, may be required in order to achieve the best OMA performance, which could be achieved with further substrate removal [79]. Further studies can focus on an investigation of long-term drift and stability, an understanding of thermal issues (including heat spreading, crosstalk and control dynamics), and waveguide-fiber couplers which can tolerate high power with low insertion loss. Improved OMA performance at the several-milliwatts levels improves the utilization of available laser power and improves the link transmission distance in an unamplified optical communication system, and lessens the need for optical amplification which can decrease the spectral span of wavelength division multiplexing and decrease the wall-plug energy efficiency.

Acknowledgements
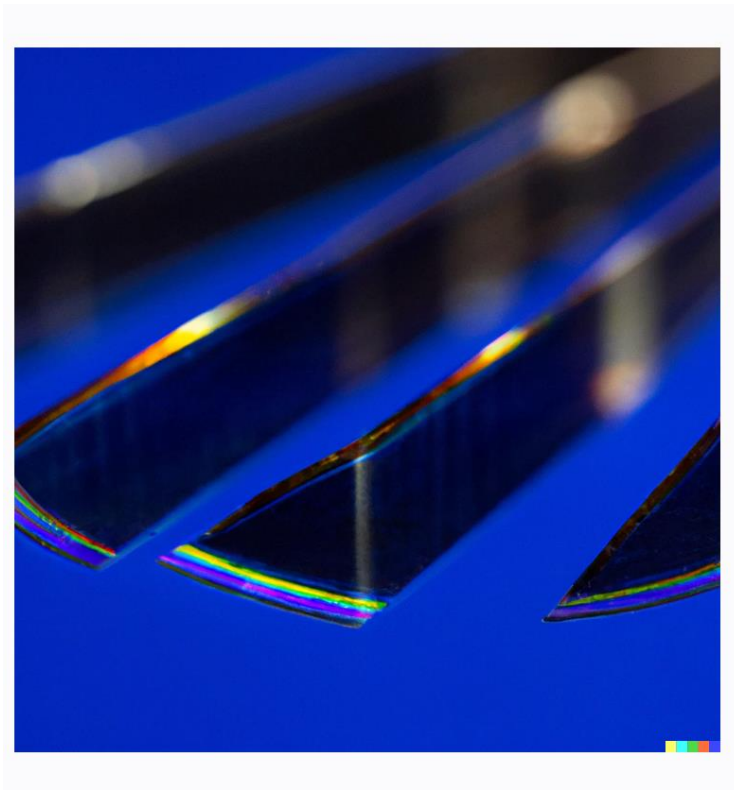
OpenAI DALL-E's interpretation of "Wavelength Selective Silicon Photonic Components", courtesy of Luke Schiefelbein.

Chapter 4

Wavelength Selective Silicon Photonic Components

4.1 Wide-range and fast thermally tunable silicon photonic microring resonators using the junction field effect

We describe here a p-n junction field-effect thermo-optic micro-heaters embedded into silicon microring resonators and used in tunable silicon photonic chip-scale optical filters. This research is based on two communication trends: (1) data networks need micro-second scale reconfigurability [80], and (2) to realistically enable wavelength-division multiplexing, optical components need the ability to tune over fairly wide wavelength ranges (tens of nanometers). Also, the fabrication technology should be simple, and photonic components should be robust to various kinds of driver circuits, including to over-driving techniques such as pre-emphasis which are used to extract higher performance from speed-limited systems ranging from audio frequencies to optical frequencies. This chapter discusses the aspects of a robust ring that is able to shift across a large wavelength range.

4.1.1 Background

Silicon microrings are important basic elements for integrated photonic devices, including filters, resonantly-enhanced detectors, wavelength converters, modulators, classical and quantum light sources [81], [82, p.], [83]–[85]. The resonator must be tuned typically—its resonance wavelength shifted onto a spectral grid or desired operating wavelength. Methods that have been developed for tuning Si microring resonators include photo-sensitive trimming[86] nano-scale oxidation [87], stress/strain effects and the incorporation of other materials as cladding [88], but the most popular approach is to use either the electro-optic effect or the thermo-optic effect, i.e., the change of the refractive index with injection or removal of charge carriers [47] or with change

of temperature [89]–[91]. Field effects in Si waveguides, though fast, are fairly weak, and are used mainly for data modulation. The thermal tuning effect are often used for microring tuning.

The most common approach to incorporating heaters in a foundry-fabrication Si photonics process flow, now well-described in textbooks [92], is to use a metal layer (i.e., after the silicon waveguide etch, dopant and contact formation steps) to define a structure such as a serpentine resistor above or near the Si microring, and drive current through the resistor. However, the hottest portion structure is separated from the optical mode by a distance of 1 µm or more, and the intervening oxide is a poor conductor of heat. Consequently, such heaters are typically slow and inefficient.

Figure 4.1 shows a sketch of a microring resonator with a tuning resistor near it; in this paper, the electrical current (I) and voltage (V) refer to the quantities indicated in the figure, and the optical measurements shown are those at the 'thru' or 'drop' optical ports of the device as indicated. The typical power levels are approximately 0.1-1 mW optical power in the waveguide, and 1-100 mW electrical power driving the resistor. Here, we form the heater by using a doped section of Si itself, through which current can be conducted. One approach is to form the heater (and the current path) transverse to the direction of light propagation [92, pp. 236-240]. Alternatively, a heater can be formed within the microring (or microdisk) resonator itself. Light stays on the outside of a bend [93], [94]or a ring [95] (e.g., a whispering gallery mode is confined to the periphery of a disk), and thus, a portion of the inner diameter can be formed into a resistor without incurring excessive optical loss by sitting directly in the path of the light. In this case, the current propagates along the microring resonator in the same direction as the light. Since the heating element is separated from the optical mode by only a few tens of nanometers (and heat has

to propagate only through silicon, not oxide), the resulting thermo-optic tuning effect is faster, and typically on micro-second scales.
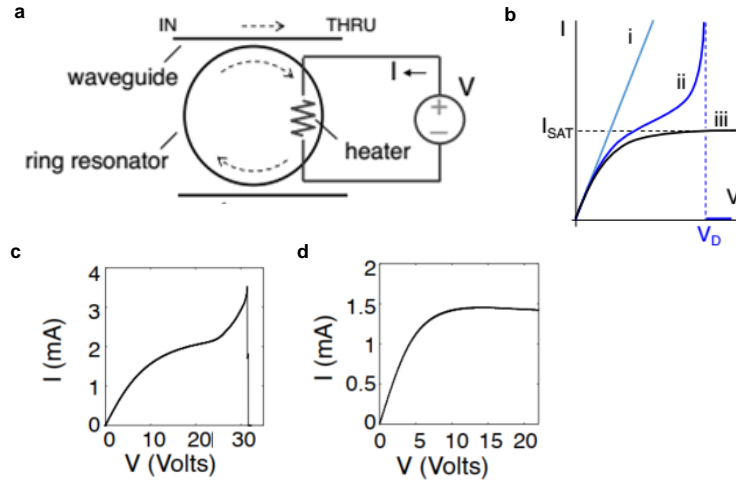
Figure 4.1: (a) Schematic diagram of a waveguide-coupled optical microring resonator near an electrical tuning micro-heater. The latter may be integrated into the microring (when the resistor is formed using doped Si segments), or may be a separate structure (when the resistor is formed using metal traces). The current (I) - voltage (V) relationship can take several forms, including (i) Ohmic, (ii) non-Ohmic, leading to runaway, breakdown and destruction at a voltage labeled VD, and (iii) transistor-like behavior with a 'saturated' constant-current source I_{SAT}. Panels (c)-(d) show experimental I-V data from structures on the chip for types (ii) and (iii).

Driving significant amounts of current (typically, 1 mA) through a small region (typically, a $0.1 - 0.2$ µm) of resistive silicon (or even metal, [91]) for prolonged periods of time can lead to degradation, electro-migration and device failure. Deep-sub-micron-scale heaters are highly nonlinear and show signs of runaway and catastrophic breakdown [see the sketch in Fig. 1(b) marked trace 'ii' and the experimental data on a test structure shown in Fig. 4.1(c)]. One reason this occurs is that the doped section of the microring is already designed to be more resistive than the tethers so that the applied voltage is dropped mostly in that section, and the decrease in carrier mobility with increasing temperature further raises its resistivity, leading to even more heating. A

40

transistor-like I-V relationship, with constant current beyond a certain saturation voltage [see the sketch in Fig. 4.1(b) marked trace 'iii' and the experimental data on a test structure shown in Fig. 4.1(d)] would not only serve to protect the device, but also allow a voltage pre-emphasis spike to be used for speeding up the response (as often seen, e.g., [89, p., Fig. 4]), and will linearize the wavelength shift with electrical power. Here, we show that such a structure can be achieved quite readily within the standard foundry fabrication processes used today in silicon photonics. We demonstrate the junction field effect (JFE) used in conjunction with bend-integrated micro-heaters in Si microring resonators, both for wide-range and narrow-range tuning, and with microsecond-scale time constants.

4.1.2 Device Details

The components were designed on silicon nanophotonic chip (see Fig. 4.2) that was fabricated as part of a multi-project run using deep ultra-violet lithography and Complementary MetalOxide-Semiconductor (CMOS) compatible processes at the Microsystems and Engineering Sciences Applications (MESA) facility at the Sandia National Laboratory. A p-type, $14-24$ Ω.cm resistivity (acceptor doping concentration approximately 1×10^{15} cm-3) silicon-on-insulator wafer with 250 nm active-layer Si thickness and 3 µm buried SiO2 thickness was used. A sequence of silicon etch steps was used to form the fully-etched and rib waveguides which were used in different parts of the chip, along with multiple steps of oxidation smoothening for waveguide sidewall roughness reduction and optical propagation loss mitigation. The waveguides were designed for low-loss transmission in the lowest-order mode of the transverse electric (TE) polarization defined relative to the device plane, and measurements of the transmission spectra

confirm that only a single mode-family was supported. Dopant implants were followed by a rapid thermal anneal (RTA) activation process, and by additional processing steps to form contact vias.
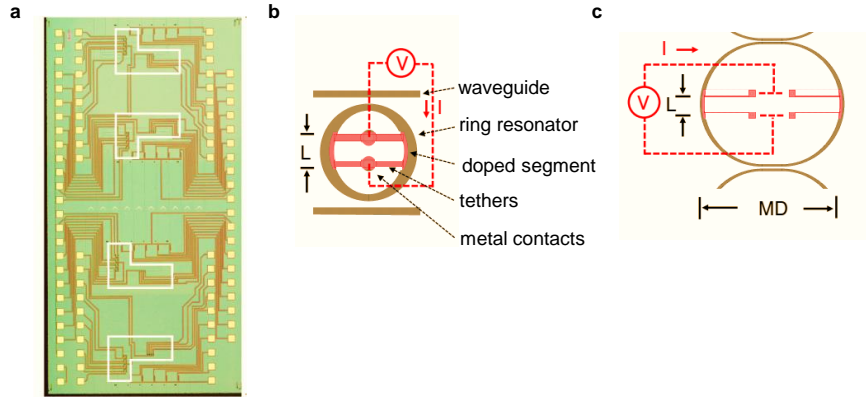
Figure 4.2: (a) A silicon photonic chip, which contained several banks of tunable microring filters (locations indicated by the white boxes), was designed and fabricated using the Sandia photonics process. (b) Diagrams of the two types of microheater-integrated microrings studied here; only the silicon mask layer is shown. The n-doped regions are indicated by red color within the gray regions which indicate the p-doped Si in the starting wafer. Numerical values of the major diameter (MD) and doped length (L) are provided in the text. The dotted red lines schematically indicate the electrical connections made to drive current through the microheaters.

A single metal layer was used for low-resistance ohmic contacts, electrical connection pads, and test resistor structures. After a deep silicon etch to expose facets for edge-coupling, the wafer was singulated into chips for testing. Electrical contacts were made by wirebonding to a printed circuit board. Of interest here are two types of microheater-integrated microring resonators shown in Fig. 4.2. The smaller microring resonators have a major diameter (MD) of 4:8 µm, and a waveguide width which varied between 325 nm and 650 nm. These microrings have a free spectral range (FSR) exceeding 40 nm (i.e., only one resonance within the C-band telecommunications wavelength), and a passband wide enough to drop at least 800 GHz. Another type of microring resonator was larger, with major diameter (MD) 29 µm, and whose waveguide

width varied between 400 nm and 800 nm. these rings had a smaller FSR (850 GHz) and narrower (but still flat-top) passbands, wide enough for only one channel on the 100 Ghz ITU-T telecommunications grid. (The FSR and bandwidth specifications were inherited from the specifications of the "MORDIA" network testbed [96, p. 4] for which project the chip shown in Fig. 4.2 was designed.) At the widest points of the waveguide, a fraction of the waveguide width was implanted with n-type dopants over a length (L) of approximately 1:7 µm and 3:4 µm for the smaller and larger microrings, respectively, to form resistive heaters. Both microrings received Arsenic (As) dopants with implant energy 380 keV and at an areal concentration of 4×10^{13} cm^{-2}, which results in nominal resistivity of 1300 Ω/sq. Also shown in Fig. 4.2 are the outlines of the Si segments labeled "tethers" which were doped more heavily and with a different dopant species to provide a lower-resistivity contact (approximately 30 Ω/sq.) to the via and metal wiring. From separate test measurements on a different part of the chip, we measured a contact / wire-bonding resistance of less than 10 Ω. In this configuration, nearly all the applied voltage was dropped over the integrated micro-heaters.
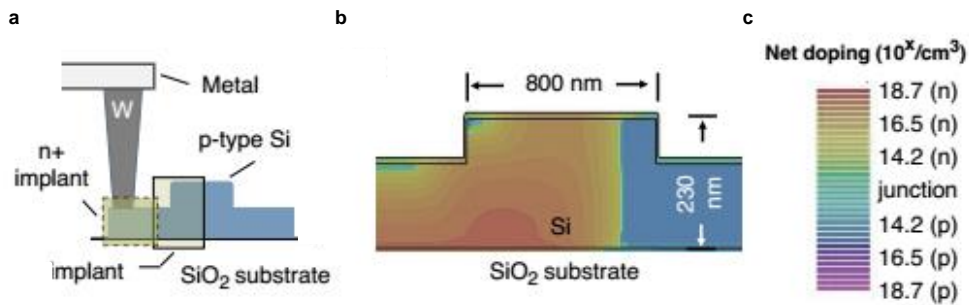
Figure 4.3: (a) Schematic diagram of the waveguide cross-section (not to scale). By partially counter-implanting (n-type) a section of the p-doped wavguide, a quasi-lateral p-n junction is created. (b) Simulation of the doped profile using ATHENA (Silvaco) for a representative waveguide section of width 800 nm in which the right-side one-half width (400 nm) was masked off for the implant. Spreading and diffusion of the implanted species results in a metallurgical junction that lies inside (under) the masked-off region. The colorbar shows the exponent of the net carrier density (units: cm^{-3}).

Figure 4.3(a) shows the cross-section of a representative implanted waveguide (schematic drawing, not to scale). Note that in the fabricated microrings, only n-implants were used in the microring section itself, and the n+ implants, tungsten (W) vias and metal traces were used near the tethers. Figure 4.3(b) shows results of a cross-sectional 2D process simulation (net doping, calculated using ATHENA Silvaco software) of the n-implant in the region indicated by the solid box with light yellow transparent coloration which is labeled 'n implant' in Fig. 4.3(a). The p-doped starting-wafer and n-implant conditions result in the formation of a p-n junction within the cross-sectional extents of the waveguide. The optical mode in the microring thus "sees" both net p- and n-doped regions with not dis-similar concentrations (approximately an order-of magnitude higher on the n side, but the optical mode sits closer to the outer edge, i.e., the p-side). This section is part of the waveguide cross-section in the widest portion of the microrings,and the direction of current flow is along the n-implanted region only, and perpendicular to the cross-sectional cut that is shown. The device thus resembles a depletion-mode junction-field effect transistor (JFET) and the diffused pinch-resistor [97], which are formed by implanting a conducting channel with a counter-doped layer deposited over it, thus narrowing or "pinching" the resistive channel depending on the base voltage. The "drain" and "source" terminals are the two contact points to the implanted resistor, across which the I-V data presented below was measured. The "gate" consists of the large island of p-doped Si which forms the un-implanted portion of the microring. We have fabricated no explicit gate contact, since doing so would significantly perturb the optical mode, which propagates around the outer periphery of the circular optical pathway. Nevertheless, carriers have a finite lifetime in the ring, in part due to recombination with the photons of the resonant mode, as well as collisions with the etched sidewalls (width-to-height aspect ratio is approximately 3:1 or 4:1 in the two types of microrings). The gate may be considered to be weakly

(capacitively) coupled to ground, as indeed are floating gates used in memory or logic cells. Depletion regions are not totally devoid of carriers, and in the saturated regime of a JFET, drain-source current continues to flow as the drain-source voltage is increased. Indeed, this is a most useful regime of operation, in which the device operates as a constant-current source.

4.1.3 Measurement and Results

I-V measurements of these integrated micro-heaters were carried out using a Source Measurement Unit (Keithley 2450). Whereas I-V measurements in Fig. 4.1(d) were taken without optical light, the data shown using square- and diamond-shaped markers in Fig. 4.4 were acquired when optical light was being guided on the chip, and at the same time as swept-wavelength optical transmission data was being recorded. Dashed red lines in Fig. 4.4(a) show the I-V relationship for microrings fabricated on a previous run (using the same physical geometry but a different species and energy of dopants) which resulted in a much higher (4-5 orders of magnitude) net carrier concentration on the donor side, compared to the acceptor side. Because of this imbalance, the impurities were not fully depleted, and the device behaved like a normal (nonlinear) resistive heater. Attempts to tune those microrings widely resulted in the current quickly exceeding the desired value, and the device was easily destroyed without much tuning. Here, not only was a much wider tuning range possible, but the driving voltages could be pre-emphasized for sharper rising transitions (as discussed below) without damaging the device.
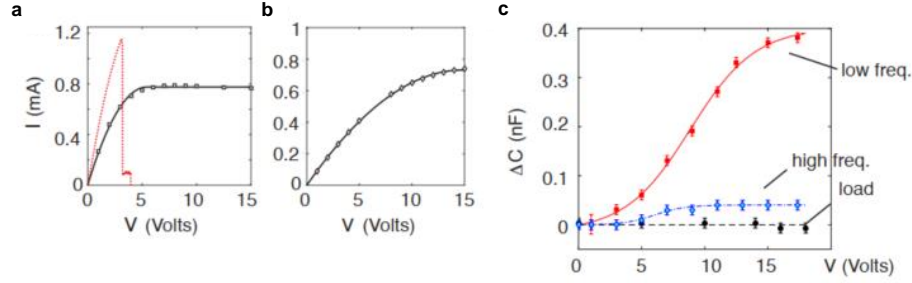
Figure 4.4: (a) The I-V measurement (small squares) for the small microrings was well fitted by the JFET I-V equation as described in the text. The dashed red line shows the I-V measurements of a similar microring but with different dopants which exhibited device destruction before saturation. (b) The larger microrings, with a longer 'channel' L, also were fitted by the same equation, with different parameters. (c) At low frequencies (< 75 Hz), the capacitance for 3 banks of dual-ring filters driven in parallel (red data points and sigmoidal fit) showed an increase with voltage. At high frequencies (100 kHz), the effect was less noticeable (blue points and fit). The black trace shows there was no change in capacitance with voltage of a loading circuit use in parallel with the device under test (see text for description). Errorbars show the uncertainty (noise) in the measurement.

We note that there are several similar points between the I-V relationships of the integrated microheater and that of a JFET. The fitted lines in Figs. 4.4(a) and 4.4(b) follow the usual JFET equation, $I = k(V_{GT}V_{min} - V_{min}^2/2)$, where k is the gain factor in JFETs and is a fitted parameter in our model describing the heater efficiency (i.e., the slope of the conductance at small voltages), $V_{GT} = V_G - V_T$ in terms of the gate voltage, V_{GT} and threshold voltage V_T (neither quantity is defined in the geometry of our device, and therefore, V_{GT} is a fitting parameter here), and $V_{min} = \min(V_{GT}; V_D; V_{DSAT})$, where V_D is the applied voltage to the heater, and V_{DSAT}, the drain-source saturation voltage in the JFET here refers to the fitted parameter value at which the I-V relationship saturates ($V_{DSAT} = 5.4$ V and 14 V for the small and large microrings, respectively). As one expects, the longer length of the resistive section in the larger microrings shows "long-channel" I-V relationships compared to the smaller microrings, which saturates earlier. Moreover, the fitted gain factor k can be used to define an equivalent transconductance $g = 2k\ V_{GT} = 0.6$ mA/V which

46

is not far from the typical transconductance value (1-2 mA/V) for MOSFETs in a similar technology process node, and is also comparable with the estimate $g \approx 2 \, (kI_{DSAT}) \approx 0{:}44 \, \text{mA=V}$ [98]. The applied drain voltage in excess of VDSAT is dropped across the depleted section of the channel. In both microrings, I_{DSAT} is limited to less than 1 mA, which protects against the catastrophic damages experienced in earlier measurements [see the red line in Fig. 4.4(a) as well as Fig. 4.1(c)]

Since the p-doped 'gate' region is physically much larger in size than the n-implanted channel (e.g., the circumference of the small microring is 30 µm of which the doped regions account for 3:3 µm), the former accumulates sufficient charges, at room temperature, on the opposite side of the metallurgical junction to form a measurable capacitor, i.e., positive and negative charges separated by a short distance. Accordingly, we expect to see increased capacitance with increased voltage as the channel gets pushed further into pinch-off. In agreement with this intuition, Fig. 4.4(c) shows measurements of three such dual-microring filters (a total of six microrings) driven in parallel, so that the capacitances add. (We have verified that driving fewer, e.g., one or two, microrings proportionately decreases the magnitude of the change.) This measurement was performed using a precision LCR meter (Quadtech 7600 Model B) with the device-under-test placed in parallel with a loading circuit that consisted of a polyster film capacitor and a series resistor, which did not change over the range of applied voltages [black markers in Fig. 4.4(c)]. The average value of these measurements was taken as the reference value from which the change in capacitance of the micro-heaters was defined. The data is plotted along with error bars defined as one standard deviation of the measured values over 64 averages. The fitted lines are based on the following functional form

The red-colored data points were measured at a low frequency (67 Hz) whereas the blue-colored data points were measured at a higher frequency (100 kHz) where the effect was less noticeable (as typical with field-effect impacted electron transport channels), but still evident. Notice that the measured capacitance increases with voltage, whereas the voltage of a capacitor affected by ferroelectricity or crystalline stress, such as a ceramic disc capacitor made of barium titanate decreases with voltage, an effect not observed here in any microring.

4.1.4 Temporal Characteristics

When driven by a pulsed waveform, an order-of-magnitude estimate of the intrinsic switching times can be calculated from a linearization of the resistance and capacitance change over the range of applied voltages,

$$R_{eff} \approx \frac{(R_{min} + R_{max})}{2}$$

Which is approximately $(1.7\,k\Omega + 5.9\,k\Omega)/2 \approx 3.8\,k\Omega$, and $\Delta C = 0.12$ nF, which predicts a rise/fall time (10%–90% transition) of approximately $\tau = 2.2\,R_{eff}\Delta C = 1.0$ µs. This is of the same order-of-magnitude as the rise and fall times of the measured optical transmission through the devices at a fixed wavelength.

Under both large-signal and small-signal driving conditions, we measured the transmission of a semiconductor laser tuned to a wavelength on the shorter-wavelength edge of a filter resonance (near 1535 nm). For the large-signal driving waveforms (amplitude 10 V), voltage pulses were provided by a pulse generator (BNC Nucleonics, Model 6040/201E, 100 Hz trigger, 4 ms pulse width), with a pre-emphasis on the leading edge as shown in Fig. 4.5(a). As discussed earlier, since current is approximately constant over the voltage values that define the pre-emphasis peak

(approximately a 5 volt range from 10 V to 15 V), the devices are not damaged, unlike the previous generation of microheaters without the JFE effect. To avoid loading the time-constants by the relatively long wirebonds in the packaged devices, a bare-die chip was used for these measurements, and voltage was applied using a multi-contact wedge (Cascade Eyepass). Data was acquired using a fiber-coupled detector with 100 MHz bandwidth d.c.-coupled to an oscilloscope. Stored data was processed offline to extract 10%–90% rise and fall transition times from the signal after smoothing (moving window consisting of 2% of the dataset) using weighted-linear-least-squares local regression (quadratic polynomial model).
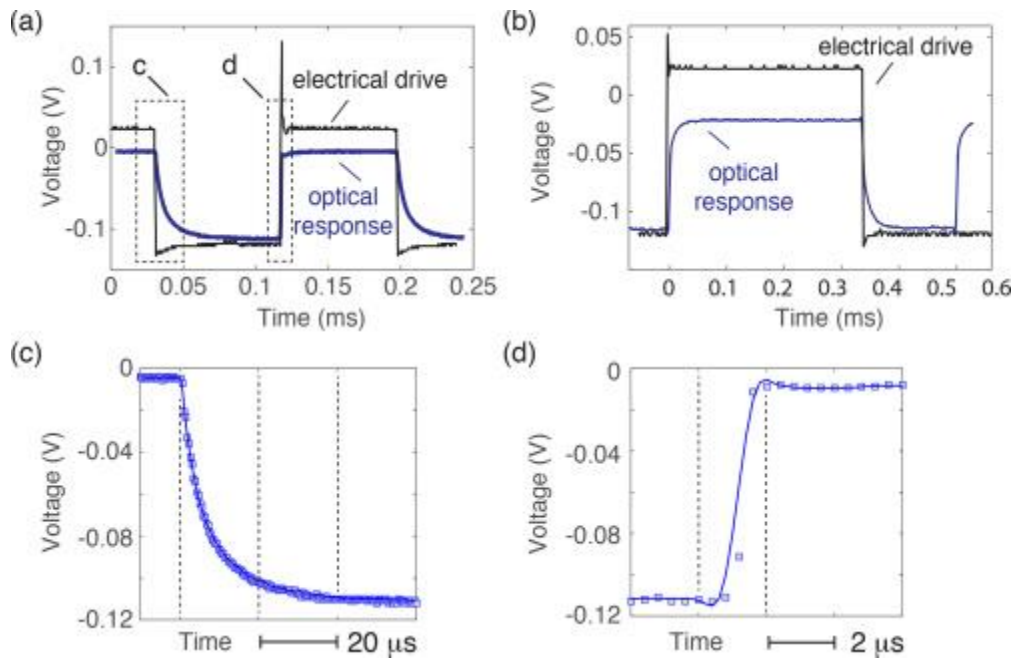
Figure 4.5: Pulsed electrical waveform driving the microheater (black line showing a vertically-scaled replica for comparison; original waveform was 10 Vpp excluding pre-emphasis), and measured optical response (blue line, measured amplitude at oscilloscope). (a) For the smaller microrings, the 10%–90% transition rise and fall times were measured to be 0.6 μs and 19 μs. The optical waveforms in regions indicated by dotted boxes are shown in detail in subsequent panels. (b) The larger microring resonators (consistent with the smaller-sized heaters relative to their size) showed 10%–90% transition times of 24 μs and 47 μs for the rise and fall transitions. (c), Magnified view of the optical waveform (squares) and fitted line for the falling edge, with a 10%–90% transition time of 19 μs (16 μs from an exponential fit). (d) Magnified view of the optical waveform (square) and fitted line for the rising edge, with a 10%–90% transition time of 0.6 μs.

49

The measured 10%–90% transition time was 0.6 μs and 19 μs for the rise and fall transitions. When driven by voltage pulses, the rising-edge transition corresponds to the 'forced response' of the device to the voltage step, whereas the falling-edge transition is measured when the device relaxes to its original state, and thus, corresponds to the 'natural response'. Heat dissipation pathways on this chip have not been optimized and can be improved. (Alternatively, two devices can be used in combination to achieve sub-microsecond transitions on both the rising and falling edges [99].) For a lower-amplitude (small-signal) driving voltage (2 V peak-to-peak, without pre-emphasis), the rising-edge 10%–90% transition time was 4 μs. As discussed below, the large-signal driving transitions result in a wavelength shift of about 25 nm; and the resulting tuning speed of 25 nm in 0.6 μs is the fastest reported for thermally tuned microrings. (Carrier-injection or depletion effects can be faster still, but result in much smaller wavelength shifts [6].) We did not measure the temporal characteristics of the larger microrings since they were designed only for quasi-d.c. shifts, and not for fast tuning.

4.1.4 Optical Characteristics

As part of the integrated Si photonic chip, both the small and the large microrings were used in second-order (cascaded) filter configuration. For coupling from sub-micron scale waveguides to fibers at one edge of the chip, the silicon waveguides were designed with a taper down to a tip width of about 0.2 μm for mode-matching to lensed, tapered fibers. At the present time, we used a standard fiber array (fiber core diameter 9 μm) and incurred substantial coupling losses (estimated 10 dB/facet). These measurements were carried out mostly over the wavelength range corresponding to the C-band telecommunications wavelengths used in our testbed (1520 nm to 1565 nm, extended past 1580 nm to clearly show the FSR of the small microrings). A single-

polarization swept-wavelength laser was used to characterize optical transmission. The state-of-polarization (SOP) of the light entering the chip was scrambled, and since the waveguides only transmit TE polarization, this incurred 3 dB insertion loss.

Shown in Fig. 4.6(a) are transmission measurements of a wide-passband filter made using the smaller thermally-tuned microring shown in Fig. 4.3(b), at voltage levels of 0 V, 5 V, 10 V and 15 V. We observe the peak shifting to longer wavelengths and no decrease in the height of the peak, which is consistent with the thermo-optic phase-shifting mechanism, whereas the carrier-injection mechanism results in a shift to shorter wavelengths, and considerable attenuation of the peak transmission [92]. The 0 dB baseline in Fig. 4.6(a) was measured by a separate calibration path on the chip using similar photonic components in the lightpath except for the ring filter. The zero-voltage loss is −8.4 dB per ring, much higher than designed; we believe that the positioning of the n-type implants in these microrings was too close to the optical mode, and the waveguide-ring coupling coefficient was incorrect (see Section 3). By fitting a Lorentzian to the data, we measured the peak shift with applied power (voltage times current) to the microheater. The fitted line in Fig. 4.6(b) has the functional form $\Delta\lambda=aP_{mw}^{b}$, with fitted parameters a = 3.6 nm/mW and b = 0.55. Taking a linear approximation to the tuning curve between $\Delta\lambda$ = 0 and 25 nm, we calculate a tuning efficiency of each heater to be 3.2 µW/GHz, a factor-of-two improvement on other recent reports [100] and nearly a factor-of-ten improvement on traditional metal heaters. Another way of stating the efficiency is in (inverted) units of nm/mW: these heaters have an efficiency of 2.9 nm/mW up to a shift of about 12 nm, which is about one-half the reported value of 4.8 nm/mW for highly-optimized conventional heaters but with heat-confinement trenches over a similar tuning range [101] (similar work was reported in [102]).

51
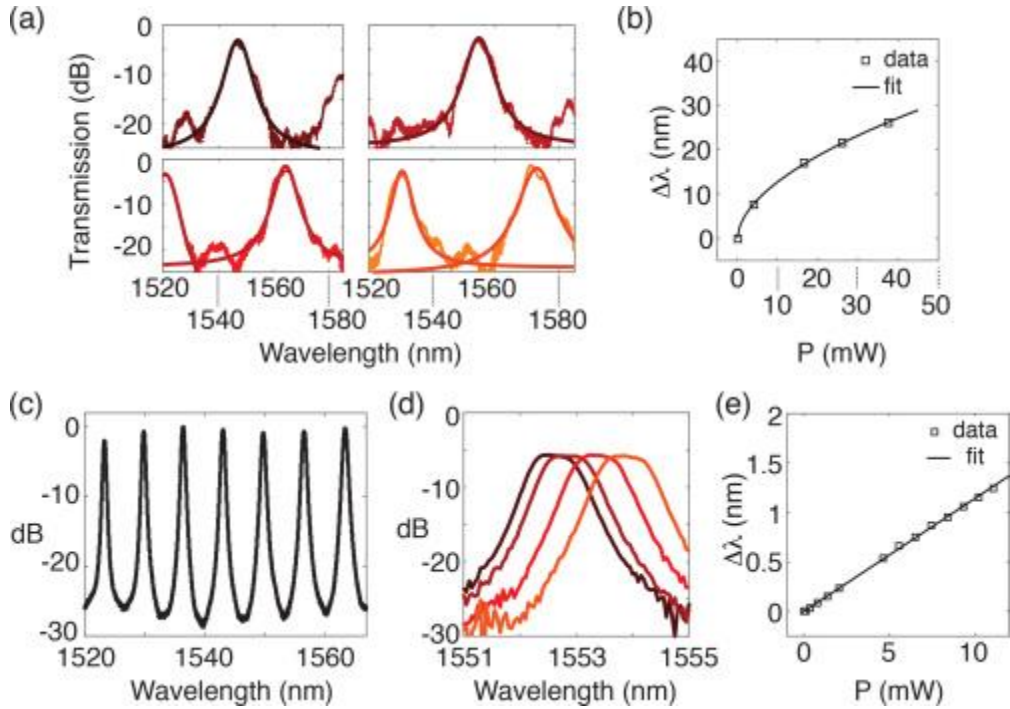
Figure 4.6: (a) Transmission spectrum at the drop'port of a dual-ring tunable filter made using the smaller microrings. Shown in panels (i)–(iv) are four measurements of wide range tuning at voltage levels of 0 V, 5 V, 10 V and 15 V, respectively. Measurements are shown by dots, and a Lorentzian fit by a solid line of the same color. (b) The peak wavelength of the fitted Lorentzian is plotted versus electrical driving power $(V \times I)$. (c) Transmission spectrum at the drop port of a dual-ring tunable filter made using the larger microrings. (d) Shown are four measurements of fine-tuning of the filter with increasing voltage levels (0 V, 5 V, 10 V and 15 V, respectively). (e) The peak wavelength of the fitted Lorentzian is plotted versus electrical driving power $(V \times I)$.

A similar dual-ring filter, but formed using the larger thermally-tuned microrings, was also measured. Because the circumference was larger, the FSR was smaller, as shown in Fig. 6(c), but the filter exhibits uniform response with a peak-valley contrast of 25 dB over a wide wavelength range for reasons explained in section 4.1.5. Figure 4.6(d) shows measurements of thermally-tuned responses around one resonance, with flat top characteristics preserved during tuning. The zero-voltage insertion loss IL was about −2.5 dB per ring. The tuning characteristics are shown in Fig. 4.6(e); we calculate an efficiency of 33 μW/GHz, which while comparable to standard designs [92], does not represent maximum heater efficiency. Here, the length of this current-carrying

segment (approximately 7 μm) was only a small fraction of the circumference (approximately 160 μm); this dual-bank filter was designed for finely-tunable flat-band transmission, e.g., tracking dynamic wavelength shifts over a few nanometers in transceivers without precise stabilization.

4.1.5 Conclusion

An iterative cycle of design, fabrication and measurement can be used to improve the performance of components when parameter extraction can be performed reliably and robustly from the data. The transmission spectrum of a microring resonator can be analyzed using a matrix model [103] to identify two dimensionless coefficients: $|t|$, the magnitude of the transmission coefficient of the ring-waveguide coupling matrix, and the single-pass round-trip propagation coefficient of the microring, α, which is related to the per-length propagation coefficient a (units: cm−1) by $\alpha = \exp(-aL)$ where L is the circumference of the microring. The measured spectrum was segmented into each individual FSR, and a nonlinear curve-fitting algorithm was used to fit the matrix model, extracting a value of $|\alpha|$ and $|t|$ for each FSR, by minimizing the sum of squared-errors on a linear scale (since the transmission peaks are measured with less noise). Although a simple matrix model cannot reproduce every artifact of the measurement, the fit shown in Fig. 4.7 is satisfactory near all peaks, and in most valleys as well.
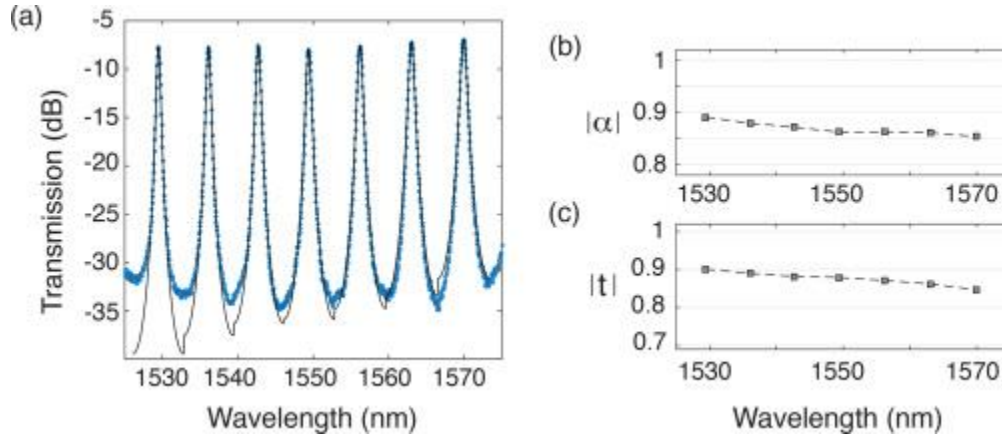
Figure 4.7: (a) Transmission spectrum of filter using the larger microrings at 0 V (blue dots) and the fit (black line) using the model described in the text. Shown are the extracted values of (b) the round-trip loss $|\alpha|$ and (c), the magnitude of the ring-waveguide coupler's transmission coefficient $|t|$ versus wavelength

Data extraction from the transmission spectrum of the larger microring shows successful design close to the desirable critical-coupling condition (single-pass round-trip loss in the ring equals in magnitude the transmission coefficient of the ring-waveguide coupler which results in maximum on-off filtering contrast. The slopes of the wavelength variation (i.e., dispersion) of the loss and coupling coefficients were also matched, and consequently, the transmission spectrum in Fig. 4.6(a) showed a clean response with more than 25 dB peak-valley contrast over more than 40 nm. We achieved this by measuring a first fabricated batch of devices ([96], which had lesser contrast, approximately 10 dB), performing parameter-extraction and analysis, and then fabricating a second batch of devices with improved performance.

However, the small microring has a very large FSR, and there is insufficient information in the transmission spectra measured with our tunable laser [there is only one FSR shown in Fig. 4.5(a) to clearly separate the role of the coupling coefficients and the propagation loss. Our measurement and design effort here is not yet complete: although we achieved an on-off contrast exceeding 15 dB at a wavelength separation of ±10 nm from the peak, the insertion loss was high

as discussed earlier. With improved designs, we may be able to demonstrate higher-order filters using the small microrings, with flat-top transmission characteristics, similar to the performance shown here for the larger microrings, or improved results obtained elsewhere [104], [105].

Since the change of the refractive index of silicon with temperature is known (dn/dT = 1.9 × 10^{-4} /K), and the waveguide cladding, made of silicon dioxide, is a poor conductor of heat, it may be argued that measurement of the transmission spectrum taken at different temperatures can be used to estimate the temperature [90], [106]. However, these heaters only cover a small portion of the circumference, and heating is highly non-uniform and local. On the other hand, quantities measured from the optical spectrum like FSR, resonance-shift etc. are intrinsically averaged over the light path, including the hot and the cold sections. Thus, although temperature increases of 250°C and 17°C can be calculated for the widest tuning ranges in Figs. 4.6(b) and 6(e), respectively, they do not actually correspond to the devices under test.

Heating results in a change of the index of refraction of the constituent waveguides, and therefore, also of the FSR of microring resonators. If the temperature-induced change in the effective refractive index, neff, is large compared to the temperature-induced change in the dispersion of the effective refractive index (i.e., of λ × dneff/dλ), which is the case for these waveguides, then the fractional change of the FSR due to the temperature change is equal in magnitude, and opposite in sign, to the fractional change of the effective index, i.e., ΔFSR/FSR ≈ −(Δneff/neff). The latter quantity is itself equal to the fractional (wavelength) shift of the resonance peak, i.e., Δλ/λ0, where Δλ is the measured wavelength shift of a resonance as shown in the vertical axis of Figs. 4.6(b) and 4.6(e), and the resonance wavelength $\lambda_0 \approx 1.55$ μm. Thus, the fractional change in the FSR is approximately 2% in the case of Fig. 4.6(b), and less than 0.1% in the case of Fig. 4.6(e).

In summary, we have presented a design for integrated micro-heaters incorporated inside silicon microring resonators which are used in filter banks, which include a junction field effect. These structures achieved a transistor-like I-V relationship, and allow driving the heaters with a pre-emphased pulsed waveform without damage. We demonstrated microsecond scale rise/fall times, and tunability over both wide and narrow spectral ranges with attractive characteristics (tuning range, efficiency, filter shape, ease of fabrication etc.) that are desirable for integrated silicon photonic components used in future microsecond-scale circuit-switched data networks. Although more work remains to be done in both measurement analysis and component re-design to improve the insertion loss and demonstrate higher-order filtering using the large-FSR tunable microrings, we believe that these types of micro-heaters may be a useful component in the silicon photonics toolkit.
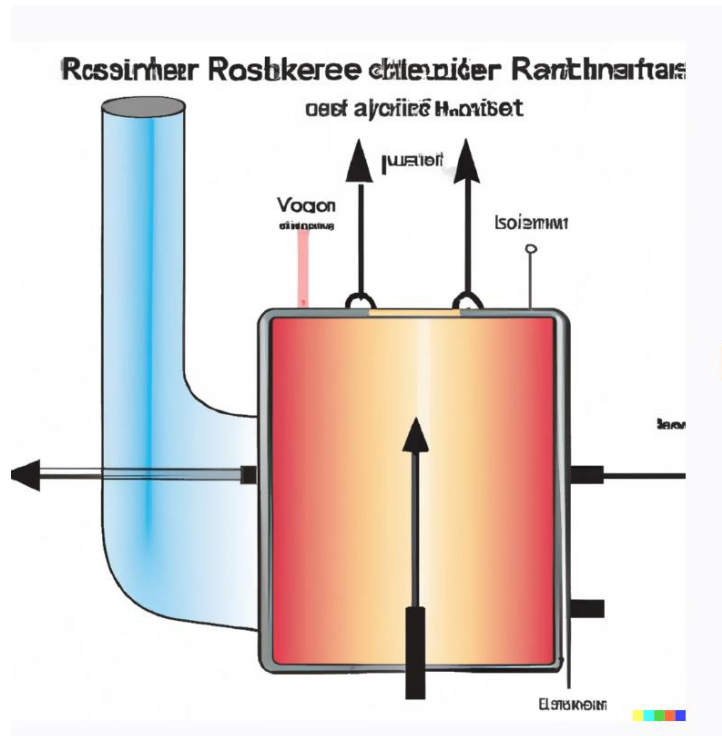
OpenAI DALL-E's interpretation of "A recirculating frequency-shifter based multi-wavelength source", courtesy of Luke Schiefelbein.

Chapter 5

A Multi-wavelength source for WDM Optical

Channels

Recirculating frequency shifter (RFS) loops can be used for electronically-programmable, variable-spacing multi-line spectrum generation, which can benefit the development of fully-flexible optical communications and other frequency comb applications. In this chapter we report on and explain the observation of significant performance variations between chip-based gain in semiconductor optical amplifiers (SOA) and fiber-based gain in erbium doped fiber amplifiers (EDFA) when used as the gain element in the RFS. Previously, SOAs and EDFAs have been demonstrated in different RFS experiments and studied separately from each other, and discussion mainly focused on the noise from amplified spontaneous emission (ASE). We show that SOA effects including four wave mixing (FWM) can be measured which impose limits to the wavelength spacing of the combs, and that this effect is mitigated by increasing the RF drive frequency of the RFS and operating SOA in deeper saturation.

5.1 Background

Electronically programmable multiline optical tone generation from a single c.w. laser is useful for a variety of applications, including carrier generation in multichannel communications, frequency comb generation, and other applications [107], particularly in size- or energy-constrained systems [108]. In most coherent communication link applications, such as optical orthogonal frequency division multiplexing (OFDM) super channels, each of these lines will be separated and modulated, and practical considerations of available chip space, driver complexity, and energy consumption currently set the sweet spot of variable tone count to up to about 10 or so lines, which is the experimental regime studied here. Several popular ways of creating compact frequency combs that are current research topics include mode-locked lasers [109], nonlinear mixing in resonators [110], optical modulation after the laser in which harmonic terms become

58

combs [111], and—as in this study—modulation after the laser with gain-assisted optical recirculation and reseeding. This method, generating multiple tones by a recirculating frequency shifter (RFS), in which a single laser seed is modulated after the laser to generate a new tone at the modulation frequency, and then recirculated in a loop to generate a further number of tones, is highly controllable and has shown successful OFDM superchannel results [112], where an excess of 26 dB optical signal-to-noise ratio (OSNR) resulted in recoverable signals, and OSNR in the 30–40 dB range showed error-free performance, with 12.5 GHz channel spacing.

Compared with mode-locked lasers and resonator-based combs, the primary advantage of the RFS stems from the comb generation taking place outside of a resonant cavity. This makes stabilization and frequency locking simpler and dynamically readjusting tone number and their spacing possible. Compared with purely electro-optic modulation-based multichannel tone generators, which depend on strong electrical radio-frequency (RF) drive overdriving the modulator [111], [113], the RFS provides gain assistance in the loop, so that only the next neighboring wavelength needs to be generated by the RF drive. This generally simplifies the suppression of the harmonics and provides better flattening of tone-to-tone variation without using line-by-line filtering and attenuation or complex wave shaping. Unlike true frequency combs, the individual tones that are generated in a recirculating frequency shifter (RFS) approach are not phase-locked, which in fact has certain advantages in terms of stability and overall system efficiency, for applications such as multichannel communications that do not require global phase coherence.

In most RFS demonstrations, to recover the loop losses before reseeding the next tone, erbium-doped fiber amplifiers (EDFAs) are typically used over semiconductor optical amplifiers (SOAs) as the loop gain element due to the higher output saturation power, gain, and lower noise

59

figure [114]. However, in applications where a compact device is critical, and size and weight requirements are stringent, electrically pumped SOAs are much smaller than optically pumped EDFAs. Aside from compactness, SOAs being chip-based can allow better control of optical path length and phase variation, especially if integrated with the other components.

A monolithic gain-assisted RFS microchip in silicon photonics has not yet been demonstrated. In InP technology, such a structure has been shown [115], where the report focused on optimizing the (quantum-confined Stark effect) modulator rather than the SOA and its dynamical properties. Other studies of the RFS, which were demonstrated with commercial off-the-shelf devices and SOAs [116], analyzed comb imperfections from the modulator and ASE. A one-to-one study with EDFAs replacing the SOAs in the same system, though, has not yet been shown. Some RFS studies also show the impacts of nonideal single sideband generation, imperfect filtering, and stabilization of the state of polarization [117], [118]. Modulation imperfections and ASE may be dominant, but when an SOA is used instead of an EDFA, as shown here, there are also important, measurable contributions from the nonlinear interactions in the semiconductor-based optical amplification, due to the fundamentally different gain dynamics and nonlinear optical mixing that occur in the SOA.

In this report, we thus investigate the differences in performance between SOAs used as the loop gain element versus EDFAs, under the same RFS loop operating conditions and all else being identical. First, we compare the flatness of the tones and the OSNR under different regimes of gain saturation for the optical amplifiers at 10 GHz channel to channel spacing. We then find that, under closer channel-to-channel spacing, the SOA has nonlinear four-wave mixing (FWM) terms, which contribute greatly and prevent stable combs from being generated—and need to be accounted for in addition to the ASE. We also demonstrate that, under deep saturation, the FWM

60

terms contribute far less to the operation of the RFS and allow for closer frequency spacing between tones.

5.2 Experiment

The experimental setup of our RFS loop is shown in Fig. 5.1. The initial seeding tone was provided by a tunable C-band laser diode set to 1550 nm. The light was coupled into the RFS loop through a 3 dB coupler and into a fiber-pigtailed lithium niobate I/Q modulator (Thorlabs-Covega LN86S-FC). The output of the modulator is a single sideband (SSB) optical signal, which is connected to a C-band 100 GHz bandpass filter (using the input and drop ports of an Optoplex reconfigurable optical add/drop multiplexer, ROADM). The flat region of the BPF covered 70 GHz (measured at the −3 dB points), which eventually limits the total number of RFS tones that can be generated. The polarization state at the output of the filter was adjusted to optimize the power into the optical amplifier. An SOA was used (Thorlabs BOA1004) with maximum small signal gain of 27 dB, saturation output power at −3 dB of 16 dBm, and noise figure of 7.9 dB. Alternatively, a low-noise EDFA (Pritel FA Series pre-amplifier) was used, which had small signal gain of 35 dB, saturated output power of 18 dBm, and noise figure of 5 dB. An optical isolator and polarization controller were used after the optical amplifier in both cases.
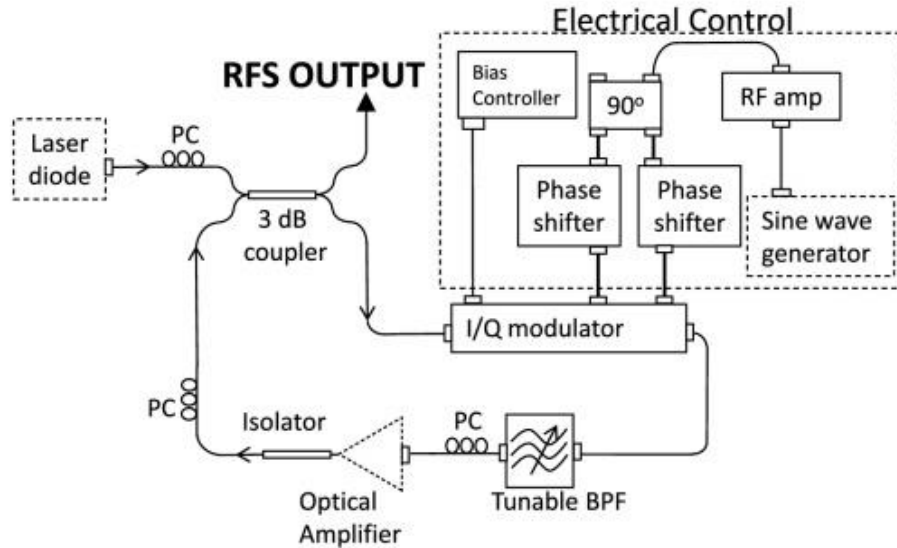
Figure 5.1: Diagram of the experimental setup.

To bias and drive the I/Q modulator as a SSB modulator, a bias controller (YYlabs D0158 module) was used to bias the upper and lower Mach–Zehnder modulators (MZM) at a 90 deg phase offset. Each MZM was biased so that the carrier was suppressed. For SSB operation, one MZM was driven by a 10 GHz RF signal, while the other MZM was driven by second 10 GHz RF signal at 90 deg offset from the first MZM drive. The two RF signals were generated by a single RF sine-wave generator (NI QuickSyn Lite Frequency Synthesizer) after amplification by an RF modulator driver (Optilab MD-20) and splitting by a RF 90 deg hybrid 3 dB coupler. The measured output of the SSB prior to filtering and amplification showed 39 dB of carrier suppression, 35 dB of undesired sideband suppression, and 31 dB suppression of the third-order harmonic tone.

To generate a programmable number of additional tones, the optical amplifier had to recover 21 dB of cumulative optical loss through one round-trip of the RFS loop (−7 dB first order sideband conversion efficiency, 6 dB insertion loss through modulator). First, with the SOA as the loop amplifier and a 0 dBm seed laser signal, the current in the SOA was increased (to about 300 mA) so that the gain equaled the round-trip loss in the loop for the total input power the SOA

received, bringing up the generated tones to the power levels shown in Fig. 5.2. Next, the SOA was replaced with the EDFA (drive current to the pump diode of 150 mA)—with all devices at the same settings—and with the exception that the polarization controllers were readjusted to provide the optimal power through the polarization-sensitive modulators, ensuring that the output powers and harmonics out of the SSB modulator were exactly the same as before when the SOA was used.

CH	1	2	3	4	5	6	7	8	AVG
SOA	39.9	37.9	36.8	35.7	35.2	34.5	34.5	34.0	36.0
EDFA	40.9	39.9	39.4	39.0	38.9	38.9	38.5	37.3	39.1
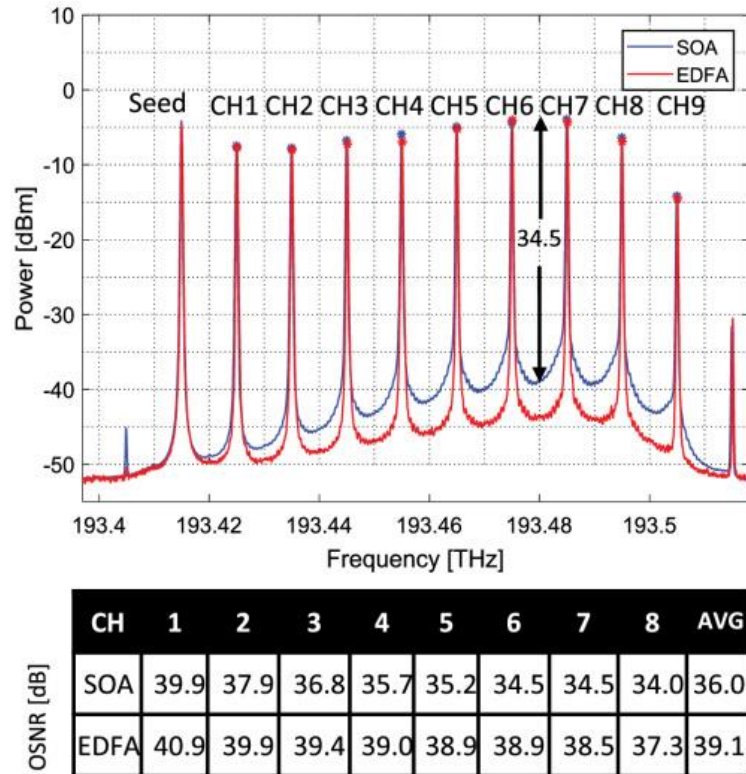
Figure 5.2: RFS tones generated with SOA compared with EDFA. Amplifiers are operating right before the 3 dB saturated gain point and not driven deep into saturation. EDFA flatness: Min, −1.89 dBm; Max, 1.58 dBm; Mean, 1.29 dBm. SOA flatness: Min, −3.21 dBm; Max, 2.57 dBm; Mean, 1.62 dBm (deviations from mean peak power).

The output of the RFS was then measured on a high-resolution optical spectrum analyzer (OSA, Finisar WaveAnalyzer), and the OSNR was determined on the OSA by a six-point moment weighted signal power density interpolation method, with noise bandwidth set to measure halfway in between channels, according to the resolution bandwidth (FWHM) of 150 MHz, and with a

spectral sampling resolution of 20 MHz. We observe that the EDFA performs slightly better than the SOA, for example, with the seventh channel (right before the 3 dB drop-off from the BPF edge) having an OSNR about 4 dB better than the SOA. In this configuration, both amplifier types demonstrate good OSNRs in our setup. The flatness is also shown in Fig. 5.2, with min and max defined as the worst-case deviations from the mean-of-peak-powers across channels one through seven (in the flat region of the BPF). The mean deviation number is taken as the mean of the absolute values of the differences from each channel to the mean-of-peak-powers (a reference point). The flatness of the tones by EDFA amplification is slightly better at 1.29 dB, compared with the flatness of the tones by SOA amplification at 1.62 dB.

5.4 Four-Wave Mixing Parasitics in SOA Gain Operation

Interesting results occur when the channel-to-channel frequency spacing is decreased (which is one of the main attractions of the RFS approach compared with other techniques of comb generation, e.g., based on micro-resonators that have a fixed free spectral range). Figure 5.3(a) shows the RFS output using the SOA and, then again, by using the EDFA (overlaid), when the SSB modulator is driven by a 5 GHz RF signal. We see that the OSNR of the SOA is measurably inferior to that of the EDFA and slightly worse than before at 10 GHz channel spacing at the same channel (e.g., Channel 7 OSNR for SOA versus EDFA is worse by 2 dB compared with the earlier 10 GHz experiment). The SOA generated tones are also less flat than the EDFA generated.
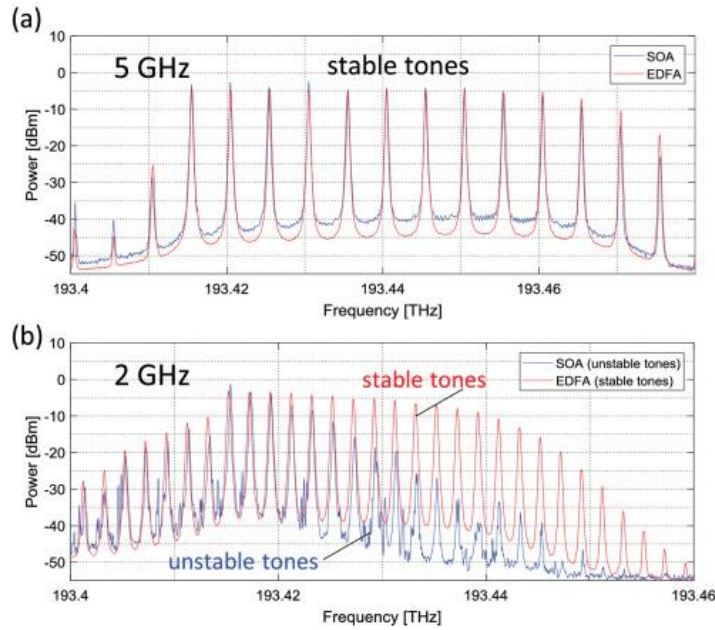
Figure 5.3: RFS output with (a) 5 GHz tone spacing, showing stable tones for both SOA and EDFA, and (b) 2 GHz tones showing stable tones only for the EDFA and failure of RFS loop and instability for the SOA. The bandpass filter was adjusted to keep the same number of tones in the flat bandpass region that the amplifier sees.

When the channel spacing is further decreased to 2 GHz, the RFS output with SOA used for loop gain shows temporally unstable tones, and instability is observed even with a low gain, i.e., before the gain is increased high enough to compensate for total loop loss, as shown in Fig. 5.3(b). Further increase of gain results in even more extreme fluctuations and failure of stability. Swapping the SOA with an EDFA—and keeping all other settings and devices constant as before—we recover stable tones with good OSNR.

A primary mechanism driving this divergent behavior between the two optical amplifiers is the degree of nondegenerate FWM that occurs between closely spaced tones in SOAs but not in EDFAs. Unlike the gain process in EDFAs, SOA gain dynamics are strongly dependent on carrier densities. When two signals are brought into an SOA (pump and probe) and phase-matching conditions between pump and probe are stronger at closer frequencies, the carrier density is

65

modulated by a beat frequency and gives rise to sum and difference frequencies. Figure 5.4 shows experimental measurements on the conversion efficiencies, defined at the output, of these undesirable FWM frequencies and how they would affect the RFS. Here, to look at the contribution of the FWM—under the same SOA operating conditions and optical power into the amplifier as it sees when used in the RFS loop—the SOA was biased at a current of 305 mA in Fig. 5.4(a). Then, two input optical signals were amplified by 21 dB, and a third c.w. laser signal a few nanometers away was used to bring the total optical power into the amplifier up to the respective levels the SOA sees during RFS loop operation. The FWM conversion efficiencies (C.E.) that approximate the FWM terms during RFS loop operation were seen to increase from −36.4 dB at 10 GHz to −26.3 dB at 2 GHz tone spacing when the SOA is not deeply saturated. This extra 10 dB of FWM C.E. contributes to pushing the RFS into catastrophic instability when the SOA is used.
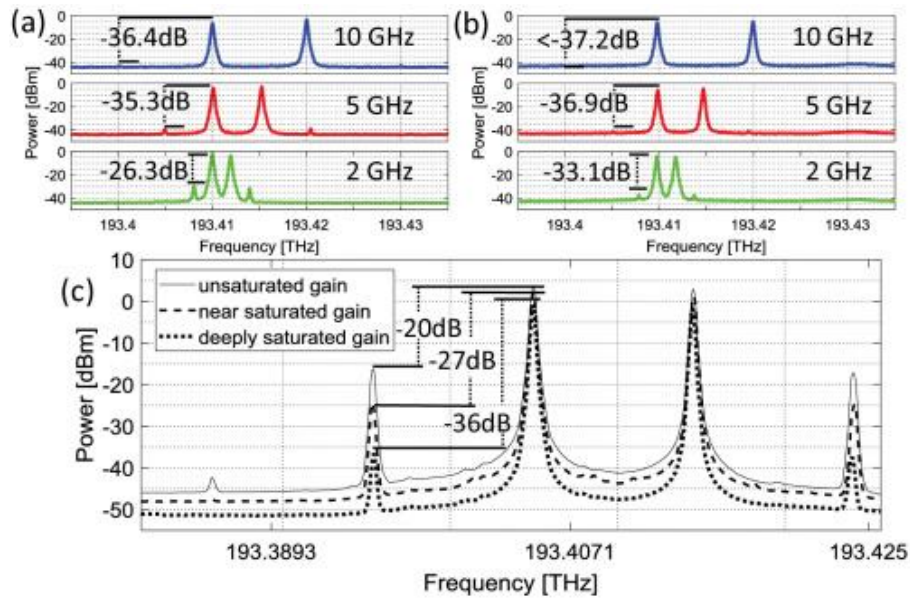
Figure 5.4: (a) FWM C.E. of the SOA before the 3 dB saturated gain point, corresponding to Figs. 5.2 and 5.3. The FWM increases by 10 dB from 10 GHz to 2 GHz spacing. Saturation power: 9 dBm, output power: 7.5 dBm, small-signal gain: 24 dB. (b) FWM C.E. of the SOA in deep saturation, corresponding to Fig. 5.5; the FWM terms are pushed down, resulting in better tone quality. Saturation power: 16 dBm, output power: 18.5 dBm, small-signal gain: 27 dB. (c) Extent of change in FWM C.E. from different SOA operating regimes, showing that operating the SOA in deep saturation is desired.

5.5 Deep Saturation Regime of SOA Operation in the RFS

Another important result from the experiments is the behavior of the SOA in the deep saturation regime and its impact on RFS tone generation. From the FWM perspective, the FWM C.E. in an SOA increases by a cubic relationship with gain, and there is weaker carrier density modulation by the pump probe beat term in saturation. Therefore, as Figs. 5.4(b) and 5.4(c) show, the conversion efficiencies decrease when the SOA is pushed into deeper saturation. Moreover—from the perspective of noise—in deeper saturation, the amplifiers act as a power limiter suppressing power fluctuations; for the SOA, the carrier densities and the gain are reduced. Given these fundamental mechanisms, we expect to see less undesired parasitic terms contributing to the RFS tones and better OSNR when the amplifier is driven deeper into saturation. Indeed, as Fig. 5.5 shows, we experimentally find that the flatness of the tones has decreased to below 1 dB, and the OSNR has increased several decibels. To push the amplifier deeper into saturation, the seed was increased by 6 dB, and the SOA was biased at 600 mA to accommodate for the increased input power and provide the same gain. The experiment was repeated by swapping the SOA with the EDFA biased at 500 mA to provide the same amount of gain.
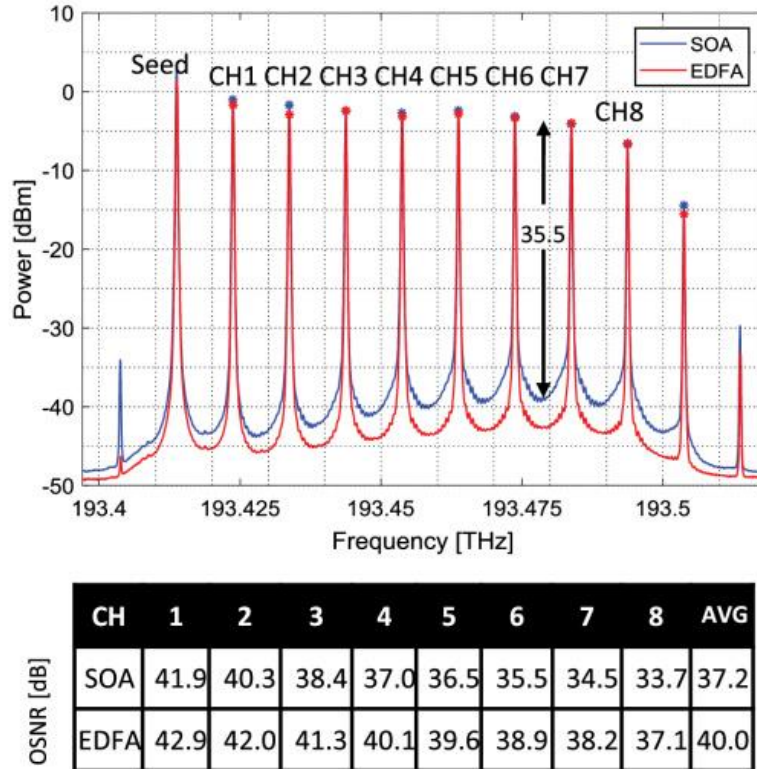
Figure 5.5: RFS tones generated with SOA compared with EDFA. Amplifiers here are operating deep in saturation. The OSNR is higher, and the tone variation flatter. EDFA flatness: Min, −1.23 dBm; Max, 1.09 dBm; Mean, 0.51 dBm. SOA flatness: Min, −1.48 dBm; Max, 1.61 dBm; Mean, 0.70 dBm (deviations from mean peak power).

To show that the tones generated by the RFS are indeed stable when a deeply saturated SOA is used for loop gain and is comparable with tones generated by EDFA under the same RFS operating conditions, we performed a different experiment for a time-domain characterization. Here, we measured eye diagrams for both the SOA and the EDFA by picking off one tone (the worst-case tone in the flat BPF region) from the generated comb, modulating the single channel by a 10 G PRBS signal (PRBS 7), and measuring the output after the modulator on a oscilloscope (Infiniium 86100D DCA-X). The filters used after the loop to separate out a single channel were cascaded filters of the same type as used in the loop. Due to the roll-off of the band edge of the filters, the tones were driven this time at 18.5 GHz to get a single tone as clean as possible, and

the 100 GHz (70 GHz −3 dB) filters were purposefully offset from each other. This cut down the signal power by more than 20 dB, so an extra optical amplifier was needed at the output. Regardless, the tone generated from the SOA and the tone generated from the EDFA was amplified by the same amount both in loop and after loop, and all variables were held constant—so we expect the relative comparison of SNR to be valid. It is expected that the SNR and relative intensity noise (RIN) of a single RFS tone will be improved with better filtering.

Δ(SOA-EDFA)	SOA	EDFA
Δ SNR : -1.8	SNR:11.23	SNR:13.03
Δ RIN : 0.5 dB/Hz	RIN:-119.7 dB/Hz	RIN :-120.2 dB/Hz
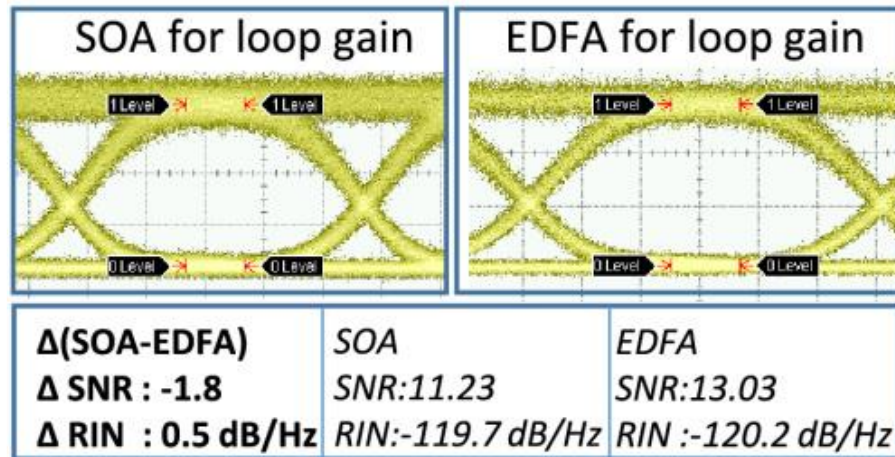
Figure 5.6: Eye diagram of single tone extracted by filters and then modulated by an MZM driven by an NRZ10 Gbps PRBS7 signal and measured on a wide-bandwidth sampling oscilloscope.

Once the tonal quality was improved using a c.w. laser, we were then able to run the RFS by replacing the c.w. laser with a 10 Gbit/s NRZ PRBS data-carrying seed channel, and pick off one of the replicated tones and view it on a sampling oscilloscope. As Fig. 5.6 shows, a clear eye diagram was obtained in both cases.

5.6 Summary

In conclusion, we have investigated the performance differences between SOAs and EDFAs as loop gain amplifiers in the RFS loop for multicarrier tone generation in greater detail. In particular, we find limitations to the spacing of the tones when using the SOA that is not present when using the EDFA, arising from nonlinear interactions caused by the carrier and gain dynamics in the semiconductor. This prevented tone generation when the spacing was 2 GHz or less in our setup. We have also demonstrated some of the key differences between operating the SOA in more linear gain regions and in deeply saturated regions and how those different operation regimes affect the tone generation in the RFS. The performance of the RFS with SOA driven to saturation approached the performance of the EDFA. These results will serve as useful guidelines toward on-chip integration of gain and proper selection of the saturation point of the SOA, which will be essential alongside the filtering and modulation characteristics, to achieve a high-quality (high OSNR) spectrum.

Acknowledgements
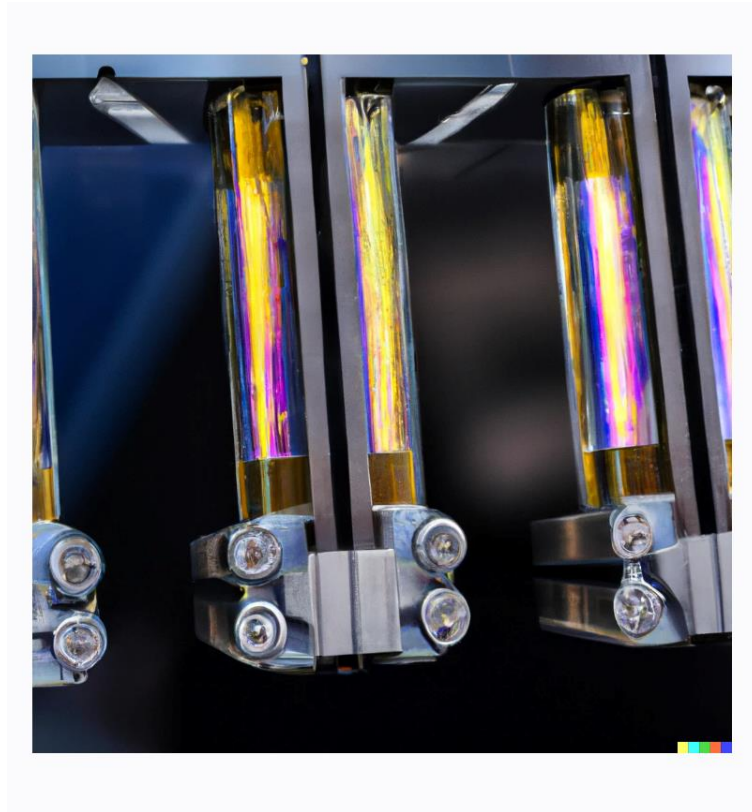
OpenAI DALL-E's interpretation of "Silicon Photonic Quantum Optic Sources and Devices on a Hybrid Silicon-Lithium Niobate Platform", courtesy of Luke Schiefelbein.

Chapter 6

Silicon Photonic Quantum Optic Sources and Devices on a Hybrid Silicon-Lithium Niobate Platform

6.1 Introduction

Advancements in the last several years in thin-film lithium niobate (TFLN) photonics have improved the state-of-the-art in high-bandwidth and low-voltage integrated electro-optic modulator (EOM) devices [119]–[124]. In current research, there is interest in the combining TFLN EOM's and other types of photonic components which need not, or cannot, be fully realized using TFLN alone. Silicon photonics already has a library of integrated device components which can be fabricated in large volumes using cost-effective wafer-scale processing without having to develop a custom procedure. These useful components can perhaps be realized and iteratively improved at a lower cost and more easily using conventional integrated photonics than in novel thin-film electro-optic materials. Our approach, discussed in this chapter, adds EOM functionality selectively where needed as part of a larger photonic integrated circuit[9], [125], [126]. Among the passive components that can be added are directional couplers, microring resonators and coupled resonator optical waveguides (CROWs) with either low-quality-factor (Q) or high-Q characteristics. When integrated with TFLN EOM technology in a way that minimizes impairments such as coupling loss and back-reflections, this combination of passives in Si photonics and the EOM devices using TFLN can provide a low-cost, yet high-performance integrated photonics platform.

By controlling the dimensions of the Si waveguide, the mode fraction contained in TFLN can be varied over a wide range without having to etch or pattern TFLN. In this way, the TFLN electro-optic modulator devices discussed here are based on hybrid optical modes, in which light is partially contained in the TFLN layer and partially in an underlying rib waveguide formed in silicon. We describe a fabrication process in [10] for a back-end integration process based on low-temperature bonding of TFLN dies. Fig. 1(b), shows a device made in this platform, with a

72

"Microchip #2" which consists of TFLN layer over oxide and a silicon handle, bonded over a selected portion of a larger Si photonics die, labeled "Microchip #1". The cross-sectional schematic is shown in Fig. 1(a) and typically uses a Si layer thickness of about 150 nm, which is thinner than the thickness of 230 nm – 250 nm used in a stand-alone Si photonics process at wavelengths of 1500 nm – 1600 nm.
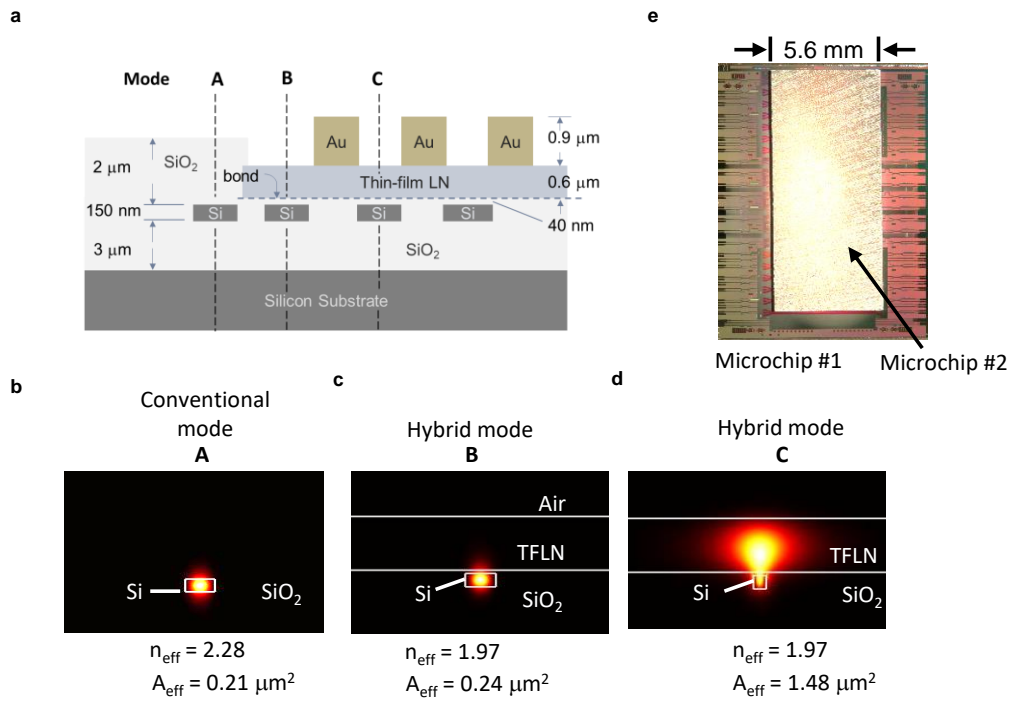
Figure 6.1: (a) Cross-section of thin-Si platform using an unetched TFLN layer in a portion of the hybrid chip. (b) Photograph of a bonded chip. Microchip #1 is a Si photonic chip on which all the waveguiding features are defined. Microchip #2 contains the TFLN layer and is bonded upside-down before the handle is removed for electrode fabrication. (c) Optical modes in the three cross-sections labeled "A", "B", and "C" in panel (a). These images show the magnitude of the simulated Poynting vector of the TE-polarized fundamental mode.

Many ways of incorporating high-bandwidth TFLN EOMs with Si photonics have been reported in the last ten years. For example, in [127], partially-etched TFLN was adhered to a silicon microchip using a low-refractive-index epoxy. In [128], partially-etched TFLN was bonded using benzocyclobutene polymer over etched silicon waveguides, which requires precision aligned bonding. In [121], a TFLN slab was rib-loaded with silicon nitride which was deposited using

plasma-enhanced chemical vapor deposition (PECVD) which can be achieved at relatively low temperatures (about 300ºC), followed by patterning the silicon nitride layer. In place of silicon nitride, deposited tantalum oxide can be used for a similar purpose of confining the optical mode[129], or amorphous silicon [130], [131]. In our approach, a layer of crystalline Si, part of a silicon-on-insulator (SOI) wafer, is processed using a wafer-scale photonics foundry process, then the wafer is segmented into individual dies for bonding to TFLN using plasma-activated oxide bonding [9], [125]. The TFLN layer is not etched or patterned, and precision alignment is not required during bonding. No polymers are used in bonded stack. Electrodes can be formed on top of TFLN after handle removal as indicated in Fig. 6.1 or buried in the SOI stack as part of the SOI foundry process [131].

As shown schematically in Fig. 1, our platform consists of two crystalline materials, silicon and x-cut thin film lithium niobate, whose refractive index is higher than that of the dielectric cladding materials SiO2 (for conventional components) and air (for the EOM section). We use hybrid modes, in which light is distributed between TFLN and Si (and the cladding) and the mode fraction in TFLN can be controlled by the size of the features in Si. This is shown in Fig. 1. We have shown less than 20% or more than 80% of the light (Poynting vector magnitude of the TE-polarized fundamental waveguide mode) at 1550 nm can be contained in the TFLN layer without etching it. The mode labeled "B" in Fig. 1(c) uses wider Si rib features and is useful for input/output transitions from the feeder waveguide mode which is labeled mode "A". Mode "C" in which about 80% of the light is in LN uses a narrow rib width for the electro-optic phase shifter section. All three modes use the same Si layer thickness so that only one lithography step is needed, which reduces fabrication cost and complexity. The single-height Si waveguide continuously connects the EOM device to the other devices such as splitters and filters without breaks and

interruptions. This reduces back-reflections and phase jumps (in transmission) that can be found at abrupt, butt-coupled interfaces. A study of the tapers and transitions was previously carried out: the transition between modes A and B can have a low calculated reflection coefficient of about 0.1 dB - 0.2 dB over a wide range of wavelengths between 1260 nm and 1650 nm, and the transition between modes B and C is adiabatic and has very low loss [132].

In this chapter, design of the individual components discussed above will be described and demonstrated. Moreover, we will show that this platform is capable of demonstrating high quality single photon generation, due to the low loss and low dispersion that it is capable of. Chapter 7 will then describe the first demonstration of photonic integrated circuits combining the elements in this platform to show high speed pulse carving for spectral control of single photons out of these chips.

6.2 Extending Silicon Photonic Quantum Sources onto a Hybrid Silicon-Lithium Niobate Platform

6.2.1 SFWM Silicon Photon Pair Sources

In this section, some background of silicon photonic entangled photon pair sources will be described, along with some definitions, and figures of merits that describe the characteristics of SFWM resonant sources that will be discussed later in the device design in this chapter, as well as the following Chapters, 7 and 8.

Silicon photonic micro-resonator sources generate photon pairs at a rate,

$$r = \Delta v [\gamma P^{res}(\lambda) L_{eff}^{res}]^2 \, sinc^2 \left(\beta_2 \Delta \omega^2 \frac{L^{res}}{2} + \gamma P^{res} L_{eff}^{res} \right) \tag{6.1}$$

where r is called the pair generation rate, Δv is the resonance linewidth, γ is the waveguide nonlinearity, $P^{res}(\lambda)$ is the resonance power build up factor of the ring, L^{res}_{eff} is the effective length accounting for the loss limited lifetime (or Finesse) of resonator, and L^{res} is the propagation length of light inside the resonator, for a given lifetime, $P^{res}(\lambda)$ is determined by Lorentzian lineshape and Q of the ring which is affected by group index, coupling strength, and loss, as in [133]–[135]. The sinc squared term reflects the dependence on phase matching, and β_2 is the group velocity dispersion at the pump, and $\Delta\omega^2$ is the square of the angular frequency separation between the pump and idler (or signal). This rate is one of the important figures of merits, and increasing it is one of the goals of research in quantum sources. Experimentally, the pair generation rate in practice can be determined by the relationship to measured coincidence count rate C, and loss through the respective channels,

$$C = \eta_1 \eta_2 r \tag{6.2}$$

where r is the on-chip pair generation rate from eq. 6.1, and $\eta_1,\ \eta_2$ are the total losses through the two channels including detection efficiency. Under ideal conditions where the biphoton state is perfectly coupled into two channels with the channels having identical photon flux and loss [136] (something that can be more easily met when the generated photons are degenerate and share spatial and frequency modes, but perhaps not as easily met where the generated photons are not, and the exact "on-chip" differences in efficiencies through the two channels are not as easily known), the pair generation rate can also be found as,

$$PGR = \frac{R_1 R_2}{C_{12}} \eta_h \tag{6.3}$$

where R_1 and R_2 are the singles counts in the two channels, C_{12} is the coincidence counts, and η_h is the heralding (Klyshko) efficiency. The Klyshko efficiency is defined as,

$$\eta_h = \frac{N_{AB}}{(N_A \times D)} \tag{6.4}$$

where N_{AB} is the average rate of coincidence detection, N_A is the is the average photon detection rate on the heralding detector, and D is the detection efficiency of the heralding detector. The pair generation rate is related to another commonly used metric, called the brightness, which is found as the photon-pair rate per unit spectral bandwidth (GHz) per unit input pump power (squared, for SWFM sources), in units of pairs.s^{-1}.GHz^{-1}.mW^{-2}. This figure of merit takes into account the bandwidth of photon generation into account while describing the rate of photons generated, since some of the important devices that single photons may interface with (e.g. atomic memories [17]) operate in a narrow spectral band.

Another important figure of merit for single photon sources is the coincidence-to-accidental-ratio, or CAR. It is a measure of the signal to noise ratio for photon pairs and is defined as

$$CAR = \frac{C_{coincidences} - C_{accidentals}}{C_{accidentals}} \tag{6.5}$$

where $C_{coincidences}$ is the raw detected coincidence counts and $C_{accidentals}$. are the accidental coincidences.

A widely used and important function that can be used to distinguish between thermal, coherent, and ideal single photon states is called the second order correlation function, $g^{(2)}(\tau)$— in the general sense, it is a correlation function on the amplitudes of fields rather than the intensities, as in a first order correlation. It can be expressed as

$$g_{j,k}^{(2)}(r_1, t; r_2, t+\tau) = \frac{\langle E_j^*(r_1,t)E_k^*(r_2,t+\tau)E_k(r_2,t+\tau)E_j(r_1,t)\rangle}{\langle E_j^*(r_1,t)E_j(r_1,t)\rangle \langle E_k^*(r_2,t+\tau)E_k(r_2,t+\tau)\rangle} \tag{6.6}$$

where the angled brackets denote an ensemble average. In the classical case, $E^*E = I$, intensity, and in the quantum case, E^*, and E can be replaced with $\hat{E}^{(-)}$ and $\hat{E}^{(+)}$, called the negative-frequency and positive-frequency part respectively, of a quantized field, and where $\hat{E}^{(+)}$ contains only annihilation operators and acts on the vacuum state to produce zero. For the special case of a single mode, and where $\tau = 0$, we can write

$$g^{(2)}(0) = \frac{\langle \hat{n}(t)(\hat{n}(t)-1)\rangle}{\langle \hat{n}(t)\rangle^2} \tag{6.7}$$

This is the most relevant expression for characterizing the single-photon source and can be related to photon number probabilities, to give

$$g^{(2)}(\tau) = \frac{N_{AB}(\tau,\Delta\tau)}{R_A R_B T \Delta\tau} \tag{6.8}$$

where N_{AB} is the number of coincidence counts recorded by a time tagger, at the histogram bin centered at delay τ with width $\Delta\tau$, and R_A, R_B are the single counts in the two channels, and T is the total integration time. Standard ways of setting up the scheme with multiple photon detectors are described in [137] as well as one detector[138]–[140] In other work, performed prior to the chips in this chapter, we performed $g^{(2)}(\tau)$ measurements on similar silicon photonic pair sources on a different chip in 230 nm thick waveguides showed these sources are capable of very low $g^{(2)}(0)$, with the three detector heralded setup [141], and are shown in Fig. 6.2 (a). Fig. 6.2 (b) shows $g^{(2)}(\tau)$ measurements on attenuated laser pulses propagating through a chip that will be described in Chapter 7, calculated from eq. 6.6, Fig. 6.2 (c) shows two detector setup measurements of $g^{(2)}(\tau)$, where instead of the signal photons coupled into 50/50 beam splitter (or idler) going into two photon detectors, signal photons go into one detector, and idler photons go into the other. This is called $g_{SI}^{(2)}(\tau)$, and from eq. 6.5 and eq. 6.8, we can see that $g_{SI}^{(2)}(0) = 1 + CAR$, and when accidental counts are low in comparison with true coincidences, i.e. $g_{SI}^{(2)} \gg$

78

1, then $g_{SI}^{(2)}(0) = CAR,$ this relationship is used for the subsequent descriptions of CAR in this chapter, after normalization.
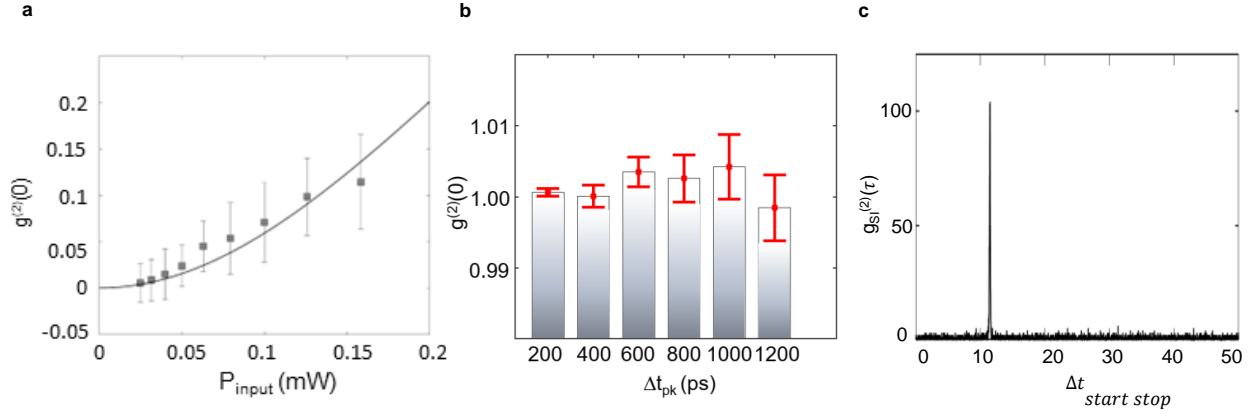
Figure 6.2: (a) a representative second order autocorrelation function at zero delay measured with a three detector setup in a prior study. (b) a representative second order autocorrelation function of attenuated laser pulses after traversing through a device (discussed in Chapter 8). (c) a representative second order correlation between the signal and idler.

It is important to verify the entanglement of photons as well. The entanglement that is studied through the photons in parts of this dissertation are time-energy entanglement, where the degrees of in an entangled state, e.g. $\frac{1}{\sqrt{2}}(|00\rangle_{\omega_s\omega_i} + |11\rangle_{\omega_s\omega_i})$, are directly related to time and energy, and where the emitted photon show strong correlations in their emission time or frequency. A way to test time-energy entanglement is through a Franson interferometer [142], where entangled photons travel through unbalanced interferometers and the phase shift in one path is varied, in two separate interferometers for the unfolded case (measurement setups which are shown further in Chapter 8). This interferometer can test two-photon quantum interference, provided that the two interferometers are nearly identical to each other, meaning that differences between the long(short) path in one versus the long(short) path in the other, are not distinguishable by the timing resolution of the detectors; the imbalance between the short and long paths also need to be long enough so that there is no single photon interference, and any interference can be attributed

to the two-photon interference of the entangled pair (quantum interference). It can be shown [143]–[145], that the output of the interferometer is a state

$$|\Psi\rangle_{out} = \frac{1}{\sqrt{2}} (|\Psi_s\rangle_1 |\Psi_s\rangle_2 + |\Psi_l\rangle_1 |\Psi_l\rangle_2) \tag{6.9}$$

where S is the short path, L is the long path, the idler is denoted "1", and the signal "2". If a phase shift $\Delta\phi$ is applied to the long paths, then

$$|\Psi_l\rangle_1 |\Psi_l\rangle_2 = |\Psi_s\rangle_1 |\Psi_s\rangle_2 e^{i\Delta\phi} \tag{6.10}$$

and thus

$$|\Psi\rangle_{out} = \frac{1}{\sqrt{2}} [\, 1 + e^{i\Delta\phi}] |\Psi_s\rangle_1 |\Psi_s\rangle_2 \tag{6.11}$$

$$\langle\Psi|\Psi\rangle_{out} = \langle\Psi_s|\langle\Psi_s|\Psi_s\rangle_1 |\Psi_s\rangle_2 (\, |1 + e^{i\Delta\phi}|^2) \tag{6.12}$$

writing the coincidence counts as

$$Coincidence \equiv \langle\Psi|\Psi\rangle_{out} \propto \frac{1}{\sqrt{2}} [\, 1 + e^{i\Delta\phi}] |\Psi_s\rangle_1 |\Psi_s\rangle_2 \tag{6.13}$$

we get that the coincidence counts are proportional to the cosine of the phase shift

$$Coincidence \equiv \langle\Psi|\Psi\rangle_{out} \propto \frac{1}{\sqrt{2}} \big[\, 1 + e^{i\Delta\phi}\big] |\Psi_s\rangle_1 |\Psi_s\rangle_2 = 2 + 2\cos(\Delta\phi) \tag{6.14}$$

The visibility, V, can then be fitted to this form from coincidence count measurements collected as,

$$d + a\cos\left(\frac{\phi}{\phi_0} + \varphi\right) \tag{6.15}$$

and defined as

$$V_{fitted} \equiv \frac{a}{a+d} \tag{6.16}$$

A raw visibility can also be quickly determined from measurements by taking the difference between the maximum and minimum coincidence counts, and normalizing by the sum of the max and min as,

$$V_{raw} \equiv \frac{\max(C) - \min(C)}{\max(C) + \min(C)} \tag{6.17}$$

where C is the collected coincidence counts. While one can infer from a visibility V > 70.7% that the photon pairs measured are quantum-mechanically correlated and serve as verification of entanglement [146], it doesn't provide a test of local realism. To provide a proof of Bell's theorem, i.e. that the measured states cannot be reproduced by local hidden-variable theories, one can perform a test to show a violation of the CHSH inequality [147],

$$S \equiv |E(\alpha, \beta) - E(\alpha, \beta') + E(\alpha', \beta) + E(\alpha', \beta')| \leq 2 \tag{6.18}$$

where $E(\alpha, \beta)$ is the correlation of the two-photon states, and found as

$$E(\alpha, \beta) = P_{S_1 S_2}(\alpha, \beta) + P_{L_1 L_2}(\alpha, \beta) - P_{S_1 L_2}(\alpha, \beta) - P_{L_1 S_2}(\alpha, \beta) \tag{6.19}$$

where $P_{S_1 S_2}(\alpha, \beta)$ is the probability of obtaining photons in a given state, collected from different time bins, for the angles α, β in the two interferometer arms. Experimentally, one should rotate the phases in the two interferometers so that the full set of four phase difference are measured, for example, phase settings of 0°, 45°, 90° and 135° where 180° results in a full period of the two-photon coincidence interference curve as will be shown in Chapter 8, where S > 2.

Purity is another important characterization of a quantum state, and plays an important role in the quality of the realized quantum interference. Chapter 7 describes in this in more mathematical detail.

6.2.2 150nm-thick Silicon Photon Pair Source

Here we show a design approach along with devices made and measured, in the 150 nm-thick silicon platform, to satisfy the resonant SFWM photon-pair characteristics described in the previous sub-chapter section. A waveguide mode simulation, for a waveguide of type "A", as

shown in Fig 6.1(b) for a single waveguide is run in Lumerical MODE across a span of wavelengths from 1500 nm to 1600 nm and the simulated effective indices and group indices are extracted, from which the dispersion can be calculated. The Si thickness is 150 nm and the width is 650 nm. The mode has an effective index of 2.28 and group index of 3.85 at 1550 nm wavelength, and small mode area of about 0.21 μm^2. This mode is well confined in the vicinity of the Si rib, and can support a bending radius of less than 5 μm with low optical loss [125][8]. A conservative radius of 10 μm is used in the microring design of the pair generation ring. Fig 6.2(d) shows the group-velocity dispersion parameter (symbol: D, units: $ps.nm^{-1}.km^{-1}$) based on a fourth-order centered differentiation of the calculated modal effective refractive index versus wavelength around 1.55 μm. than typical values D ~ +3,000 $ps.nm^{-1}.km^{-1}$ for a fully-etched Si waveguide of 525 nm width and 225 nm thickness, the values of D in the waveguides here about a factor of five lower [148]. The dispersion values are comparable to the material dispersion of silicon D ~ -900 $ps.nm^{-1}.km^{-1}$ indicating that the geometry does not play as strong of a dispersive effect in these waveguides as in conventional Si waveguides.
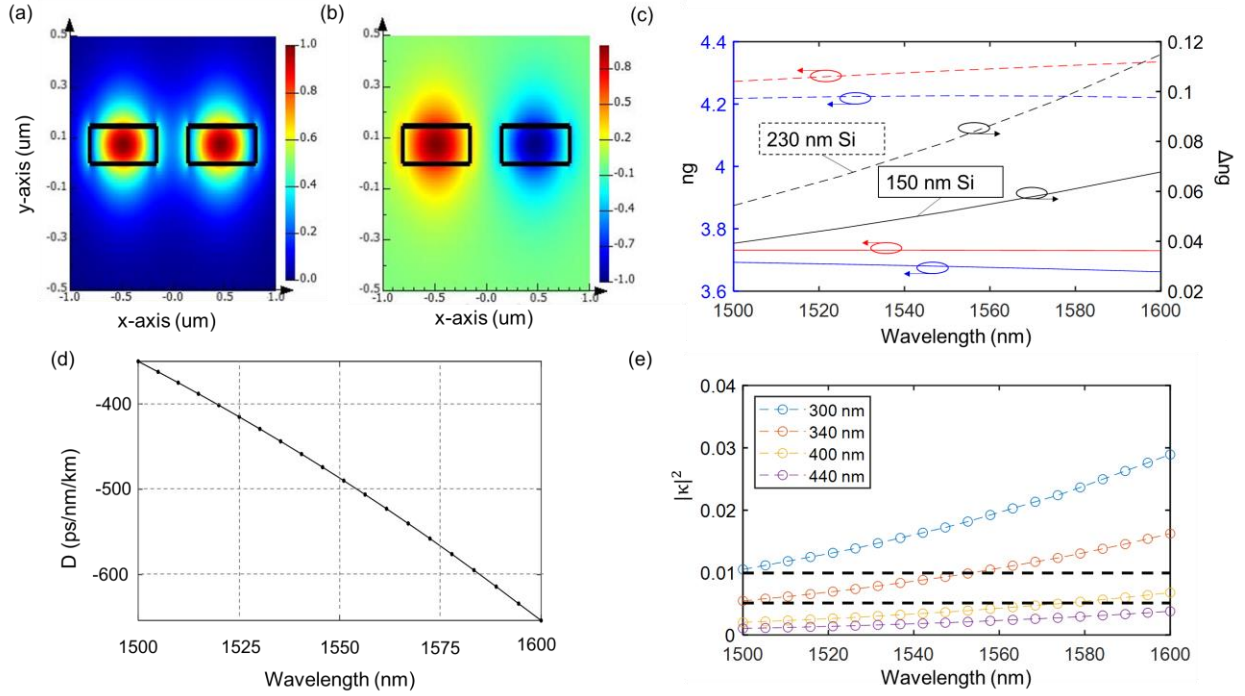
Figure 6.3: Mode field (E_x) profile of directional coupler's symmetric mode in the thin-Si waveguide [composed of single waveguides with Mode "A" in Fig. 6.1(c)]. (b) Mode field (E_x) profile of directional coupler's anti-symmetric mode. (c) Group indices of the symmetric mode (blue), and anti-symmetric mode (red), for the thin-Si directional coupler (solid lines) compared to conventional 230 nm height silicon waveguides (dashed lines). (d)) Calculated dispersion coefficient for the thin-Si waveguide [Mode "A" in Fig. 6.1(c)]. (e) Length-integrated directional coupling coefficients for different values of the gap between the two waveguides as indicated in the length. The design target ranges (0.005-0.01) are indicated by the dashed horizontal lines.

Broadband characteristics can also be achieved in this 150nm-thick silicon waveguide platform. Besides the lower dispersion characteristics, the mode field profiles of a directional coupler designed in this platform lead to parameters conducive to low coupling dispersion. Fig. 6.3 (a) and (b) show the symmetric and asymmetric modes of the coupler, respectively and their group indices, ng, in Fig 6.3 (c). The difference between the group indices, as well as difference between the effective indices, and length, contribute to the dispersion of the power coupling coefficient, $|\kappa|^2$, as discussed in [103]. The directional couplers in this platform show coupling dispersion, $d|\kappa|^2/d\lambda$, of about 0.1 μm^{-1} which is about one order of magnitude lower than $d|\kappa|^2/d\lambda$

of 8 μm⁻¹ of fully-etched Si waveguide couplers[103]. The differences in group index delta is reflected in the smaller differences in group index between the supermodes of the 150 nm thick silicon directional coupler—compared with the 150 nm thick silicon directional coupler, the 230 nm thick silicon coupler's group index differences are almost twice as large as that of the 150 nm thick version in this work. For a fair comparison, a slightly larger gap (by about 40 nm) was picked for the 230 nm thick silicon coupler to achieve the same effective index difference (coupler crossover length was held equal). Fig 6.3 (e) shows a family of coupling coefficients. .. For a high-Q micro-resonator, we seek a small value of $|\kappa|^2$, typically around 0.005 to 0.01 which is indicated by the dashed lines. For the microring designed in this work, the chosen gap was 400 nm.

Fig. 6.4 shows the design of the microring, made from two types of Bézier bends are shown in Fig. 3(a), labeled Type I and Type II. In the Type I design, the initial and final widths are 0.65 μm and the most aggressive (the two control points of a quarter bend are equal) Bézier bend design is used. In the Type II design, a less aggressive bend is used which is in-between the conventional (circular) ring and the Type I design[149], [150, p. 17].
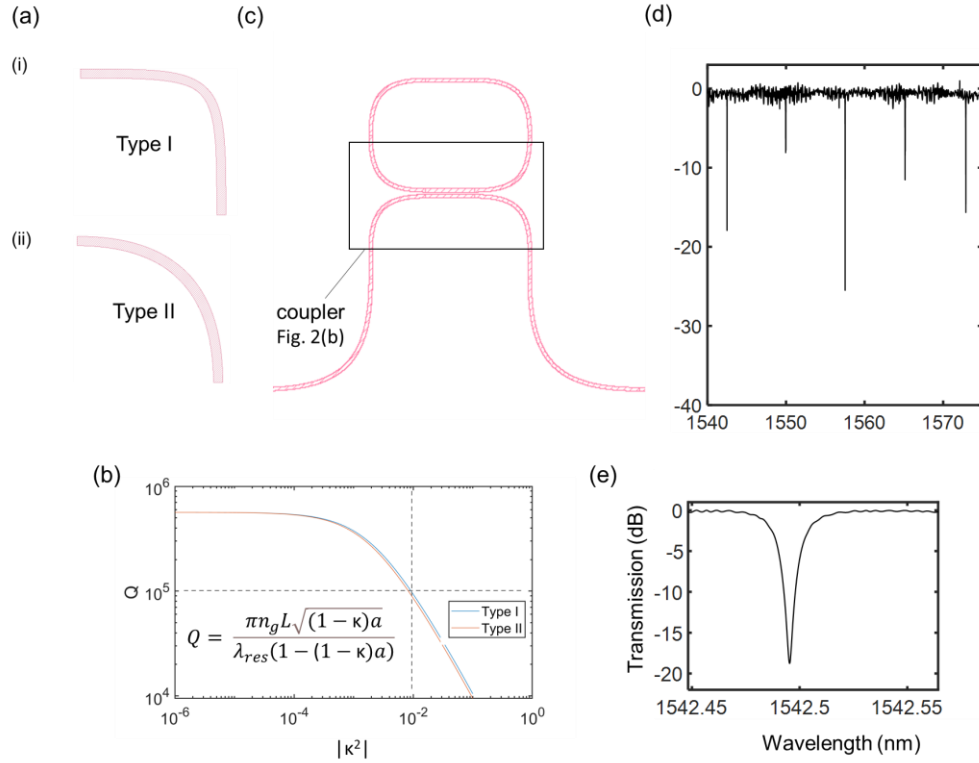
Figure 6.4: (a) Schematic drawings of two types of Bézier bends and their use in a waveguide-coupled microring resonator. (b) Calculated (loaded) quality factor (Q) versus the magnitude of the inter-waveguide coupling coefficient. (c) Schematic drawing of the microring device fabricated, composed of Type II bends (d) Measured transmission of the microring in (c). (e) Zoom in on the measured transmission of a high-Q microring using the Type II design, achieving a loaded Q of 1.4 x 105, close to the design target shown by dashed lines in panel (b).

To test the 150nm thick SWFM pair generation resonator chip, the microresonator was diced to allow easier access to test ports. Fig. 6.4(c) shows the layout of the ring that was tested and Fig. 6.4 (d) and (e) show a measurement of the transmission across five FSRs, and a zoom in on a resonance respectively under a low power measurement to avoid resonance bistability and two-photon absorption nonlinearities. The measured loaded Q is 1.4×10^5, which is close to the and suggests that the experimental optical propagation loss is under 1 dB/cm which was assumed in the model. This is consistent with earlier calculations which predicted a reduced optical propagation loss for thin-and-wide Si waveguides compared to the conventional (500 nm x 230

nm, height x width) design[151]. The measured Q's here are in fact comparable to those of the best microrings in our earlier work which we have reported as being useful for bright and efficient entangled photon-pair generation[141], [152].

Next, single photon measurements are performed to determine performance of the microring resonator as a SFWM photon pair source. The experimental setup is shown in Fig. 6.5; a continuous wave laser at the pump wavelength of about 1557 nm is coupled through a polarization maintaining fiber to a lensed tapered fiber and into a chip that was diced from the bonded TFLN modulator and silicon devices microchip. The diced-out remaining portion is shown in the cartoon drawing in Fig 6.5(a) and the input light is coupled in from the diced side into a straight waveguide—measurements taken from this side showed less resonance splitting and was used for subsequent measurements.
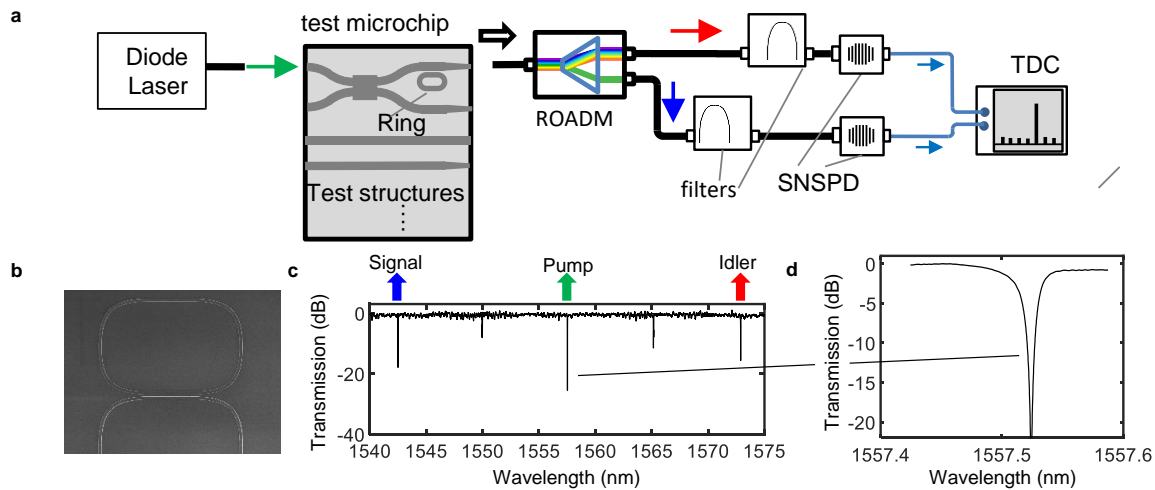
Figure 6.5: (a) Experimental setup used to measure the CAR. (b) SEM image of the microring resonator. (c) transmission of the microring resonator. (d) Zoom in of the pump resonance.

The pump laser coupled into the chip propagates through an MMI (used for testing purposes) and then into the single waveguide bus coupled ring resonator and out of the chip through edge tapers into PM lens tapered fibers. The pump, signal and idler are then coupled into

a series of 3-port reconfigurable optical add-drop multiplexers (ROADM) represented by the cartoon marked "ROADM" where the pump light is dumped and then the signal and idler are split into different fiber paths. The signal and idler are each filtered by sets of bandpass filters and into two superconducting nanowire single photon detectors (SNSPD), click detectors in a 1K Cryostat (discussed further in Chapter 8) that emit electrical pulses upon detection of a single photon. The electrical pulse is amplified cryogenically and propagates out of the cryostat and into a low jitter Time-to-Digital-Converter (TDC) that records the start-stop time between the electrical pulses triggered by the signal and idler pair of photons coming from our microchip. The microchip also had a set of test structures, through which the losses in path through which the photons propagated was able to be extracted. The measured coupling losses of the edge taper through lens tapered fiber to lens tapered fiber output, and the coupling losses of the non-tapered straight waveguide through lens tapered fiber to lens tapered fiber output were 5 dB and 9.2 dB, respectively. The MMI loss plus excess loss from waveguide bus after the tapers to the ring was 3.8 dB. The cumulative losses through the ROADMs, filters, and into the input fiber of the SNSPD was 16.2 dB and 15.3 dB for the signal and idler channels, respectively. The detector efficiencies of the SNSPD were characterized separately prior to the experiments with a calibrated low-noise floor average power low speed optical power meter, from the fiber input of the crystat to the respective SNSPD, and both detectors were measured to have detection efficiencies of 0.6. Fig 6.5(b) shows an SEM image of the microring resonator used for photon pair generation, and Fig 6.5(c) shows the transmission, with arrows labeling the pump, signal, and idler resonance. Fig 6.5(d) shows a zoomed-in higher resolution measurement of the resonance at the pump wavelength, measured to have a Q of around is 1.2×10^5.
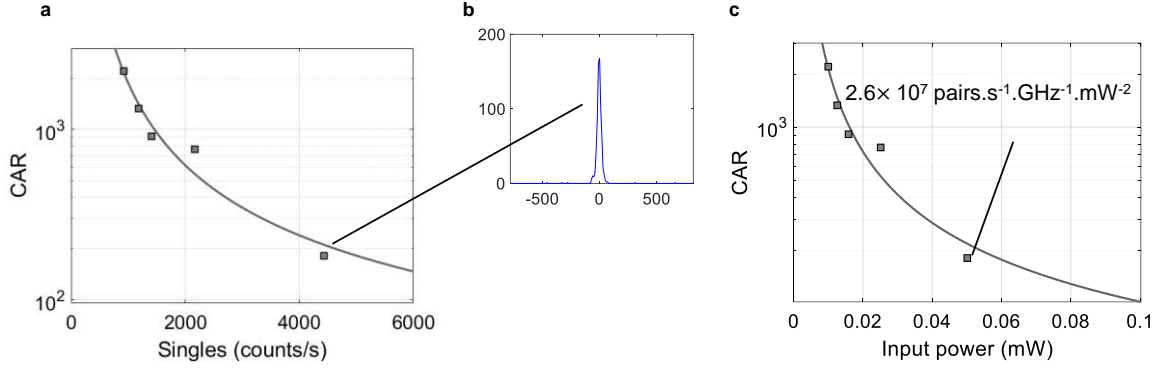
Figure 6.6: (a) CAR measurements (b.) second order cross correlation between the signal and idler for it's respective measurement point. (c) CAR scaled with loss, and the calculated on-chip brightness.

The start-stop timetags collected by the TDC are histogrammed at a bin widths of 20 ps, across 4000 bins to create the plot of g_{SI}^2, from which the CAR can be calculated for varying input power levels, shown in Fig. 6.6(b). From eq. 6.8, collecting the two channel coincidences over the single channel counts, the CAR versus raw count rates is plotted in Fig. 6.6(a). Taking the losses from the laser to chip, chip to fiber, filters, and SNSPD detection efficiencies, the on-chip power is calculated to give the plot of Fig. 6.6(c), from which the pair generation rate and spectral brightness can be calculated. The pair generation rate is calculated from eq. 6.xxx , by taking the product of the single's rates, dividing by the coincidence rate, and dividing by the input pump power. The CAR is shown in Fig. 6.6 is high but is several times lower than in our prior work [153] due to using less filters here, but can be substantially improved by adding laser pump filters to reject the amplified spontaneous noise (ASE) in future work. The raw Klyshko efficiency is estimated to be ~2%, taking the coincidence counts over the singles rate and then dividing by the detection efficiency. The on-chip Klyshko efficiency estimated this way is about 19%, and taken with the high extinction transmission, implies that it is closer to critical coupling than under-coupling[154], and suggests that higher Q designs with higher brightness can be designed, and that more complex coupling schemes to improve heralding efficiency while preserving high Q due to

the low losses on this platform are worth exploring [155]. For an on-chip coincidence rate of 1.0 $\times 10^5$ Hz, at an input pump power of about 0.05 mW, we find a pair generation rate of 41 ± 9 MHz.mW^{-2} (one standard deviation uncertainty), this is good compared to our demonstrated prior work (149 MHz.mW^{-2} and 1-10 MHz.mW^{-2} [133], [153]). Dividing the pair generation rate by the FWHM of the loaded quality factor, and by the square of the optical pump power in the feeder waveguide, we calculate the spectral brightness of the source to be 2.3×10^7 pairs.s^{-1}.GHz^{-1}.mW^{-2} which is the same order of magnitude and comparable to the spectral brightness in our best devices (7.1×10^7 pairs.s^{-1}.GHz^{-1}.mW^{-2} [153]).

In summary, we show the first silicon photonic SFWM pair-generation device integrated on a thin-film lithium niobate platform with low loss. These initial demonstrations show performances comparable to the best silicon photonic photon pair generation devices from out earlier work in 220 nm and 230 nm thick silicon. A combination of several factors: low loss, low group velocity dispersion, high Q, and broad-band characteristics leading to substantially more constant FSR's across a wide wavelength range all contribute to the promising performance shown in this study. Moreover, looking at Fig 6.5 (c) and (d), we see that at a loaded Q factor higher than prior work, the extinction is deeper—this shows that the coupling is closer to critical coupling than previously, and yet the photon pair generation rate for a given input power is higher, likely due to the lower GVD. This means that in future studies, the coupling strength can be lowered safely (with respect to fabrication tolerances), moving the design target into high Q regimes without suffering a large decrease in coincidence counts from SWFM phase-mismatch. This makes the microring designs in this platform useful, and as will be shown in later chapters, can be incorporated with many other high performance and high speed devices.

6.3 Resonant Filters on the Hybrid Silicon-Lithium Niobate Platform

This section describes resonant ring filters that were designed in the hybrid silicon-lithium niobate platform, with the low dispersion, broadband waveguide characteristics as described in the earlier section 6.2.2. A schematic of a second order coupled-microring optical filter is shown in Fig. 6.7(a), the design is a simple prototype of a more general class of optical filters based on coupled-resonator optical waveguides (CROWs) that can be used as integrated optical filters with a lower back-reflection than in-line waveguide gratings. These kinds of filters have been combined with nonlinear optical microrings performing frequency conversion and filtering without requiring a separate chip for this purpose [156]. We have previously shown that rather than cascade a large number of resonators in one continuous segment, improved performance can be achieved by concatenating multiple shorter segments [85]. Hence, the performance of elementary coupled-ring filters (as short as two rings in this case) is of interest. Here, we use the thin-Si platform and relatively strongly coupled resonators, with each racetrack using the same four Type II Bezier bends with a nominal radius of 10 mm, but with a longer straight section of 20 mm and a narrower gap of 0.3 mm. From simulations, this should achieve a relatively flat-top response with a full-wdith at half-maximum (3 dB) bandwidth of greater than 100 GHz (about 0.8 nm) at 1550 nm.

An experimental measurement is shown in Fig. 6.7(b) for a wide range of wavelengths measured using a swept-wavelength laser, and in the vicinity of 1550 nm in Fig. 6.7(c). The grey line shows the transmission through a test waveguide in the vicinity of the coupled-microring filter with the same length of input and output feeder waveguide ports, so that the insertion loss of the filter can be obtained by comparison. The measurement of the reference waveguide shows some ripple from Fabry-Perot effects from the edges of the test chip; these are extraneous to the design. This ripple is also superimposed on the filter transmission and has not been factored out. Therefore,

the actual transmission response near the peak of 1551 nm is likely to be slightly flatter than shown in this raw data.
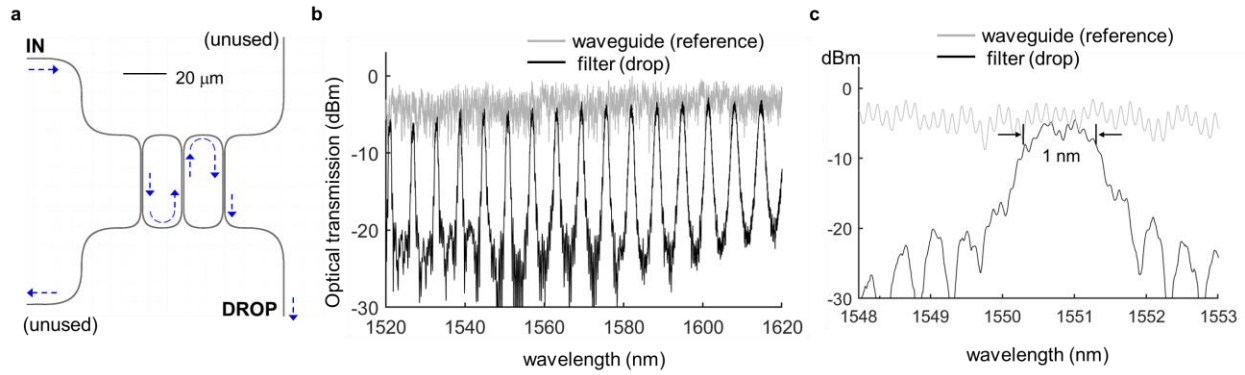
Figure 6.7: (a) Schematic drawing of a coupled-microring filter. (b) The drop-port transmission is measured and compared with the transmission through a conventional waveguide on the same chip. (c) A magnification of the transmission around 1550 nm.

Within the range of wavelengths from 1520 nm to 1620 nm (which span the C and L bands), the band-center insertion loss (IL) ranges between 0.57 dB to 1.15 dB, with an average of 0.9 dB. This is similar to the insertion loss our group reported earlier for coupled silicon microrings in the conventional silicon platform [156]. The free spectral range (FSR) is about 0.76 THz (5.77 nm) at 1550 nm with a bandwidth of about 125 GHz (1 nm), for an effective finesse (F) of about 6. A low value of F necessary in a silicon-based flat-top (Butterworth) optical filter to prevent a buildup of optical power in the rings which would cause nonlinear loss or phase shift, which is undesirable and would degrade the performance. The measured extinction ratio exceeds 30 dB at the lowest points of the stopband around 1550 nm as shown in Fig. 6.7(c)—it may likely to be higher as it may be limited by the detector noise. There are also some ripples in the stop-band of the coupled-resonator filter; these are usually the result of disorder and have been seen in other CROW structures in the conventional thicker Si platform as well [157], [158]. When multiple stages of

91

such filters are cascaded, these interference effects should be mitigated or eliminated. Consistent with the observation of low dispersion of the constituent waveguide discussed in in prior section, there is relatively little change in the FSR, which only slightly increases from 0.75 THz at 1530 nm to 0.77 THz at 1600 nm.

6.4 High Extinction Modulators on the Hybrid Silicon-Lithium Niobate Platform and their characterization

While lithium niobate modulators are among the most studied and deployed modulators in the world, an increasing amount of research in recent years in this material has been on thin film lithium niobate, where physical features and waveguides are made in or on nanometer (usually several hundred) thin layers of lithium niobate are. Following the discussions at the beginning of this chapter, here we describe modulators with hybrid optical modes of type "C" as was shown in Fig. 6.1(e). As opposed to the plasma dispersion effect that changes the refractive index in conventional silicon photon modulators using PN junctions, lithium niobate modulators change the refractive index through the χ^2 Pockels effect that occurs in non-centrosymmetric material.

6.4.1 Modulator Design and Measurement

In contrast with the earlier bonding studies between unpatterned LN and Si, [159]–[161] the approach we and others have used is to perform bonding after the waveguiding features have been fabricated, i.e., a silicon die with waveguides was fabricated through a silicon photonic foundry process, over which SiO2 is deposited, and planarization is performed using a chemical-mechanical polishing (CMP) process. We are able to bond over a large reticle-sized area (several square centimeters). [9], [125], [162] (Hybrid LN-Si microring resonators can use a much smaller

bonded area.33) In our approach, once the bonding of the LN film is complete, no further processing of the LN film is performed. In particular, there was no etching of LN which is performed in some approaches [127], [163]–[166] or sawing of the LN,36 or deposition and patterning of additional layers for optical waveguiding [129].
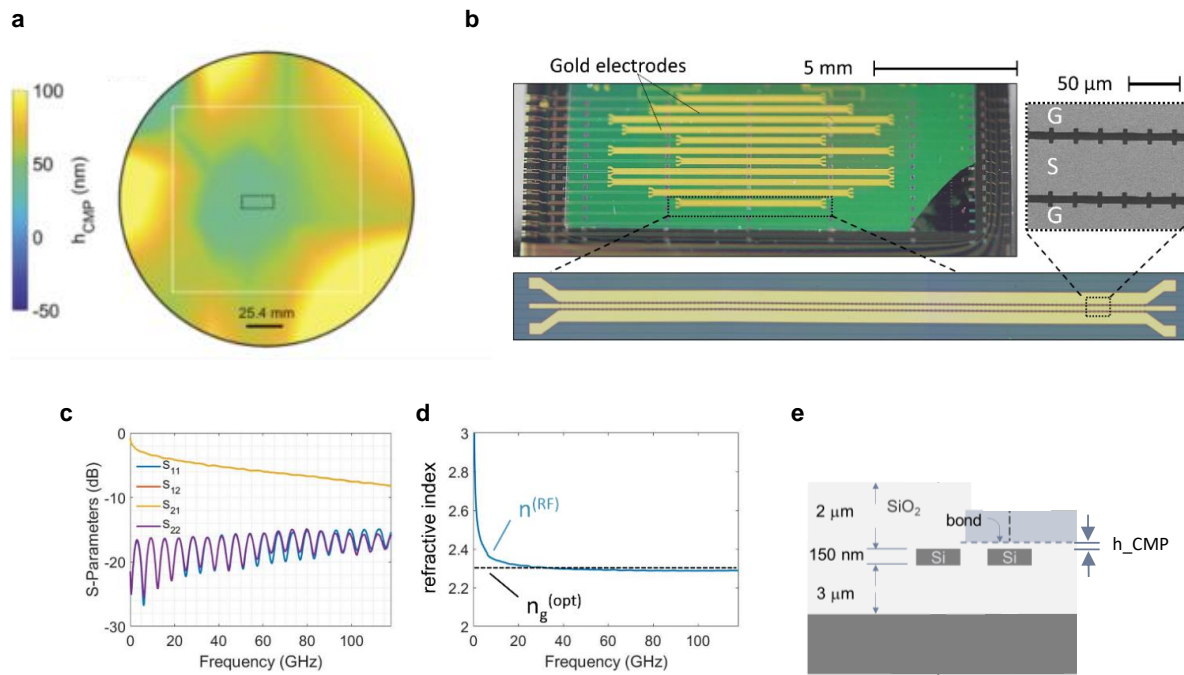
Figure 6.8: (a) Wafer CMP oxide height map extrapolated from measurements. (b) Microscope image of a hybrid Si/TFLN chip using the cross-section shown in Fig. 1. Insets show the traveling-wave electrode structures for a Mach-Zehnder modulator. (c) Measured S parameters up to 118 GHz (d) A representative plot of an inferred microwave refractive index (solid blue line) compared to the optical group index (dashed black line).

Design of modulator begins with identifying the height of the layers in the initial passive 150 nm-thick silicon, as shown in Fig. 6.8 (a), where the CMP oxide thickness was measured by ellipsometry. In a traditional high-speed LN modulator with diffused waveguieds and co-planar waveguide RF electrodes, the microwave index is slightly greater than 4, which is much larger than the typical value of the optical refractive index, which is around 2.2. The thicknesses of the

oxide buffer layer under the electrodes, and of the electrodes themselves, are increased, which increases the capacitance of the RF transmission line and decreases the microwave index, nm. Increasing the buffer thickness draws the RF field out of LN and into the buffer layer, which has a lower dielectric constant. Increasing the electrode's thickness pushes the RF field out of the buffer layer into air, increasing the effective area of the capacitor that is formed between the edges of the electrodes. While these effects improve the index matching, the modulator becomes less efficient. A traditional high-bandwidth LN MZI modulator can use gold electrode thicknesses of up to 19 μm, and only a few reports of such EOM's have demonstrated a 3-dB electrical bandwidth more than 50 GHz. In the hybrid modulator, like the thin-film LN modulator without the bonded Si rib waveguide [167] the situation is reversed: the microwave index is lower than the optical group index. With the inclusion of the Si rib waveguide, in particular, there is a relatively simple way of matching the indices. We defined the waveguiding features in the Si layer alone, with the only variations occuring in the width of the Si rib, and with no etching or patterning of the LN layer. In our test wafers, the Si layer thickness of 150 nm was achieved by thickness reduction from the original crystalline Si layer thickness of 230 nm in the starting SOI wafer, but could alternatively be achieved over specific sites by etching. Waveguide features were patterned by conventional Si processing, followed by oxide deposition and subsequent chemical mechanical polishing (CMP) and oxide thinning by a timed wet etch (diluted hydrofluoric acid) process. These are important steps in our hybrid integration process which is based on room-temperature oxide bonding (as contrasted, for example, with polymer adhesive bonding [128]).

Simulation results, run in MATLAB, to capture the frequency response of the traveling wave MZM with conventional CPW (non-segmented) electrodes are shown in Fig. 6.8 (a). The model extracts the simulated RF mode's index, losses from a 2D mode simulation and scales it

94

with the square root of the frequency, uses the extracted characteristic impendence from the 2D simulation, and plugs the numbers into the relations developed in [168], to give an estimate of the frequency roll off. The measured response of a modulator fabricated in this process with CPW electrodes is shown in Fig. 6.9 (b). 3D field propagating simulations necessary for the segmented electrodes pictured in Fig. 6.7 and the modulator used in Chapter 7 are not the subject of this dissertation and the segmented designs will not be discussed here.
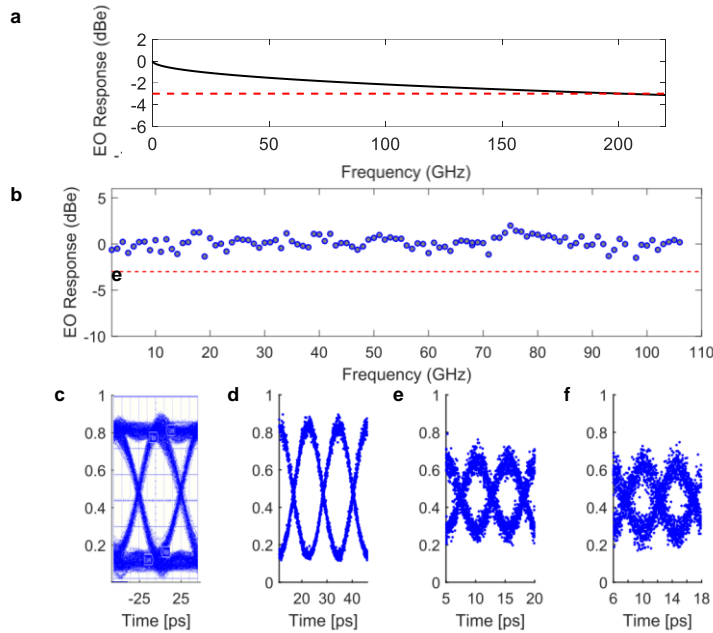
Figure 6.9: (a) Simulation of Electro-optic response for a hybrid lithium niobate MZM with CPW electrodes with an analytical formula written in MATLAB taking into the parameters simulated by 2D Lumerical simulations. (b) Electro-optic response of the hybrid lithium niobate MZM with CPW electrodes from sideband OSA measurements. (c) Eye diagram for 20 Gbit/s data modulation using a pseudorandom binary sequence. Modulation eye diagrams of large-signal RF sinusoidal modulation at increasingly high frequencies, (d) 40 GHz, (e) 90 GHz, and (f) 102 GHz. The vertical axis is in arbitrary units, proportional to optical power, with about 1000 points resolving the full scale. The offset of the horizontal time axis is arbitrary, with reference to a stable sampling clock at 80 MHz used in the sampling oscilloscope instrumentation.

The measurements on conventional CPW electrodes (not segmented) are also shown in Fig. 6.9 (b)-(f). We summarize some of the aspects of the basic characterization of the hybrid MZM which support the direct high-frequency measurements presented here [9]. From the

measured S-parameters, the microwave refractive index, nm, and the characteristic impedance, Zc, were calculated, using standard algebraic transformations and lossy transmission line circuit analysis [169]. A rf refractive index of 2.25 and characteristic impedence varied between 53.4 and 55.1 Ω from dc to 110 GHz are inferred from the data. If both index and impedance were perfectly matched (not true in the current designs), the RF-loss limited bandwidth would result in a 3-dB point of $\alpha m(f_{3dB,el}).L = 6.4$ dB. Our modulators which achieve greater than 100 GHz 3-dB electrical bandwidth have L = 0.5 cm. If we require that the 3-dB electrical frequency $f_{3dB,el} \geq 100$ GHz, then, we would need $\alpha_m(100 \text{ GHz}) \leq 12.8$ dB cm^{-1}. Measurements of the CPW showed $\alpha_m(100$ GHz) = 7.7 dB cm^{-1}, which is well under the limit. Thus, even with a small deviation from perfect index and impedance matching, RF losses in our devices using thin aluminum electrodes are not a limitation to achieve higher than 100 GHz 3-dB electrical bandwidths.

To show the time-domain modulation patterns, the drive voltage has to be a larger fraction of the half-wave voltage in order to result in open "eye" diagrams. We show these eye diagrams captured using a sampling optical oscilloscope. In Fig. 6.8(c), we show a modest-speed eye diagram (20 Gbit/s) using on-off keying (OOK) modulation, generated using off-the-shelf optical communications test equipment, with an arbitrary waveform generator (AWG) generating a pseudorandom binary sequence (PRBS) digital data sequence. No probe, cable or detector compensation, or pre-emphasis was applied in this measurement. In Figs. 6.9(d)–(f), we show the measured modulation patterns when driving the EOM with a sinusoidal waves of increasingly high frequency, extending beyond 100 GHz, which is well beyond the analog bandwidth of the arbitrary-waveform generators available today (Keysight M8194A, 45 GHz). At these extremely high frequencies, we used millimeter-wave discrete components to generate an RF modulation tone. Thus, these ultra-high-frequency eye diagrams lack the 0-level and 1-level traces (i.e., the

96

top and bottom parts of the eye), unlike the eye diagram in Fig. 6.9(c), but still reveal parametric information about the signal crossings, over- and undershoot, skew or asymmetry, and the opening. Although the eye opening gradually closes with increasing frequency, as expected, no skew, tilt, or vertical imbalance in the crossing point was evidenced. The extinction measured through a laser sweep to show DC transmission showed about 30 dB of extinction.

The microwave signal was generated from a swept-frequency microwave CW oscillator (Anritsu). For generating RF frequencies up to 40 GHz, an RF amplifier (MITEQ) which was band limited to between 26 GHz and 40 GHz was used. For generation of RF frequencies greater than 40 GHz, a multiplier chain was used, which consisted of an RF synthesizer, $6\times$ multiplier (AMC10, Millitech) which covers the frequency range 75 GHz–110 GHz (approximately), and GaAs and GaN amplifiers. The noise of these amplifiers is seen in the measured modulated waveforms, although the eye opening is still clearly visible at beyond 100 GHz. The output of the amplifier chain was coupled to a WR-10 waveguide, which was adapted to a 1.0 mm RF cable, incurring some loss in the signal power. The millimeter-wave signal was incident on the modulator microchip using 50 Ω ground-signal-ground (GSG) probes rated to 110 GHz. Calibration up to 110 GHz was performed using a high-frequency RF power sensor and calibration substrates. We report measurements at the discrete modulation frequencies available in these experiments which were determined by the band-selective RF amplifiers.
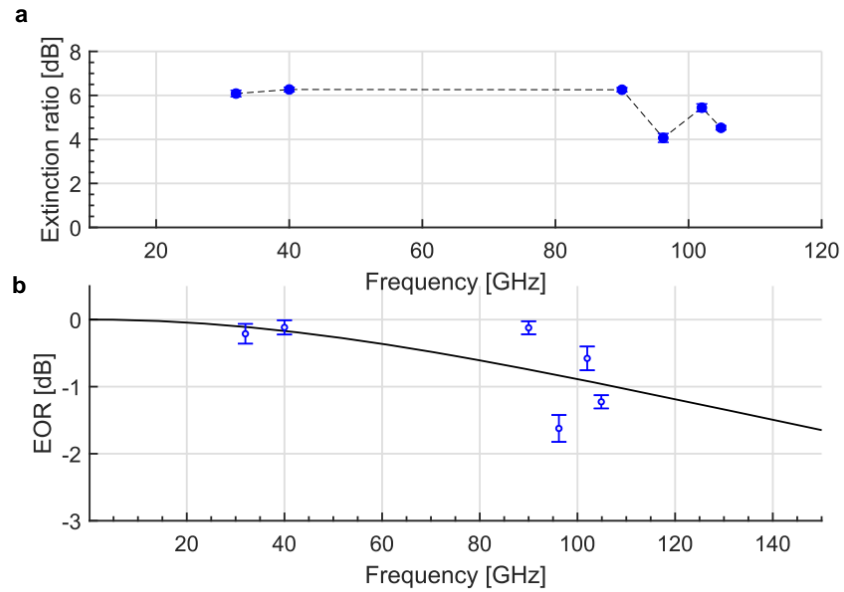
Figure 6.10: (a) Extinction ratio vs modulation frequency for beyond small-signal analog modulation at discrete frequencies up to 105 GHz. Available frequencies were determined by the band limitations of the RF and millimeter-wave amplifiers. (b) The Electro-Optic Response (EOR), defined in the text, which characterizes the response of the hybrid modulator. The black line is a single-pole, low-pass filter fit to the data, which indicates a 3-dB cutoff frequency of 141 GHz.

The signal to noise ratio (Q) of the modulation pattern diagrams is calculated to be 12.5 dB at 40 GHz, 7.4 dB at 90 GHz, and 6.1 dB at 102 GHz. Although the eye diagram closes somewhat at 100 GHz in comparison to lower frequencies, the opening shown here is significantly greater than in 100 Gbit/s (70 GHz analog bandwidth, $V\pi$ = 7.4 V) etched and bonded thin-film LN MZM's [128].

The measured modulated waveforms were computationally processed to infer the EOM characteristics. First, a nonlinear least-squares fit to each of the modulated traces was performed using a raised-cosine function [170], with an initial seed value for the fitting parameters (frequency and amplitude) obtained from a Fourier transform of the data. In Fig. 6.10(a), the vertical axis, labeled the extinction ratio, is defined as the ratio of the maximum to the minimum optical power of the modulation. Optical power was calculated by converting the number of counts to energy

and dividing by the collection time. Differences in the output of the RF amplifiers at different frequencies were accounted by measuring the RF power before the probe pads.

Separately, the instrument response function (IRF), i.e., the impulse response of the detector apparatus, was measured and fitted to an exponentially modified Gaussian function whose full-width at half-maximum was $t_{FWHM} = 6.3$ ps. The IRF is a jitterlike (zero-mean, finite-variance) noise contribution which results in spreading out the measured time-domain waveforms, i.e., an ideal delta-function-like sharp temporal response becomes spread laterally to neighboring time bins, and is reduced in amplitude at the peak time bin. Thus, the IRF results in reducing the amplitude measured in each temporal slice of the eye patterns shown in Fig. 6.10, compared to the "true" response of the device. We did not deconvolve the IRF in the modulation eye diagrams shown in Fig. 6.10, in order to show the raw measurements similar to the conventional oscilloscope (Agilent DCA-X), but in order to characterize the EOM response correctly, a correction factor is needed. The fitted amplitude of each sine wave was multiplied by a correction factor, whose value was calculated from the convolution between the fitted raised-cosine function and the measured IRF, with the latter being normalized to its probability density function. The correction factors were calculated to be $(0.203)^{-1}$, $(0.22)^{-1}$, $(0.30)^{-1}$, $(0.77)^{-1}$, and $(0.85)^{-1}$ for RF frequencies of 105 GHz, 102 GHz, 90 GHz, 40 GHz, and 32 GHz, respectively.

The electro-optic response (EOR) is defined as EOR = OMA(f_{RF})/OMA($_{DC}$), where OMA($f_{RF)}$ is the Optical Modulation Amplitude at the RF frequency (e.g., f_{RF} = 32, 40, …, 105 GHz), and OMA($_{DC}$) is its value at the DC voltage applied to the electro-optic modulator (the so-called biasing curve). The OMA is the defined in terms of the eye diagram (as usual) as the difference between the "1" and "0" power levels in Watts. Note that if the average power level varies between measurements (which is typical of using band-selective RF amplifiers to achieve

large-signal modulation), the inferred OMA will be mathematically different even if the modulator achieves the same extinction ratio (ER, defined as the numerical ratio between the "1" and "0" power levels). Thus, we recorded the drive voltage at each frequency at which these measurements were performed and used it to renormalize the OMA. To be fair, we normalized all the measurements to the "worst-case" measurement which took the longest measurement time (unsurprisingly, at the highest modulation frequency limited by the available equipment, 104.88 GHz) for which the peak-to-peak voltage applied to the MZM electrodes was 4.45 V. (For comparison, the peak-to-peak voltage for most of the range of the modulated-sideband measurement was between 0.7 V and 1 V.)

Once this renormalization is performed, ER then has a one-to-one mapping with the OMA so that the OMA used in the final EOR calculation is correctly referenced to a constant average power, and the frequency roll-off can be only then be correctly extrapolated. We fitted a single-pole low-pass response to the data, as shown in Fig. 6.9(b), which indicated in a 3-dB (electrical) roll-off at $f_{3dB(E)}$ = 141 GHz. This is qualitatively consistent with the RF modulated-sideband measurements reported earlier, which indicated a 3-dB roll-off at frequencies well beyond 105 GHz.

Acknowledgements
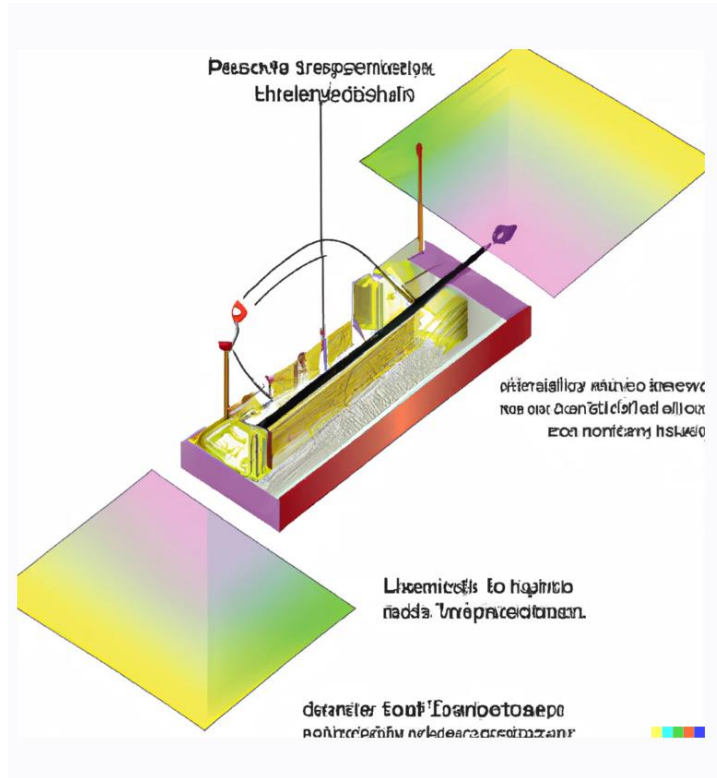
OpenAI DALL-E's interpretation of "Spectral Shaping of Photon Pairs on a Single Chip with 110 GHz Modulators and High Q Resonators", courtesy of Luke Schiefelbein.

Chapter 7

Spectral Shaping of Photon Pairs on a Single Chip with 110 GHz Modulators and High Q Resonators

The chip chip described in this chapter combines devices from a standard 300mm-wafer silicon foundry and TFLN, without etching features in the thin film lithium niobate. This work enables on-chip electronic programmability and tunability of the pulsed light pumping the parametric sources from c.w. lasers, which have already been integrated with silicon photonics and has been recently produced industrially in large scale. It brings together the best-in-class devices: high speed modulators capable of high extinction and low loss, where the phase modulation is not coupled to loss modulation, unlike high speed modulators in III-V and organic material [171], [172], with silicon photon pair sources high performing quantum properties, a material that has demonstrated some of the largest reconfigurable quantum processors to date [173]. The ability of silicon foundry processes to create large scale circuits with precision fabrication has also led to the demonstration of novel paradigms quantum optics and demonstrations such as recent work in topologically protected biphoton states and quantum light in silicon photonics[174], [175].

The results of this work on bonded thin film lithium niobate with silicon photonic quantum devices is a timely demonstration of how hybrid integration approaches (in this context meaning bonding, used in addition to common terminology that also encompasses transfer printing and pick-and-place [176]) presents a viable roadmap towards scalable quantum photonics and new avenues for wavelength-shifting of photons and quantum pulse gate operations [177].

7.1 Background: Spectral Purity of SFWM Microring Sources

This section describes the models used to compare the theoretical joint spectral intensities of the photon pairs from the microring resonator with the measured results. A microring resonator under cavity enhanced SFWM generates a biphoton state of the form

102

$$|\psi\rangle = |0\rangle + \xi \iint d\omega_s d\omega_i \; \Phi(\omega_s, \omega_s)|1\rangle_s|1\rangle_i \qquad (7.1)$$

where ξ is a scaling factor accounting for the photon-pair flux, $|\Phi(\omega_s, \omega_s)|^2$ is the joint spectral intensity and for which, $\Phi(\omega_s, \omega_s)$, the joint spectral amplitude, is

$$\Phi(\omega_s, \omega_s) = \int d\omega_s d\omega_i \, \alpha(\omega_p)\alpha(\omega_p + \omega_p - \omega_p)l(\omega_p)l(\omega_p + \omega_p - \omega_p)l(\omega_s)l(\omega_i)$$

$$(7.2)$$

where $\alpha(\omega)$ represents the pump laser's Gaussian mode spectral distribution and $l(\omega)$ is the Lorentzian spectra of the microring resonator [155], [178], [179]. The function for $l(\omega)$ used here span across the free spectral ranges covering the signal, pump, and idler wavelengths of interest, arising from the intracavity field,

$$l(\omega) = \frac{a^2 \, (1-t^2)}{1+a^2t^2 - 2at \cos\left(\frac{2\pi n_{eff}(\omega)}{\lambda L}\right)} \qquad (7.3)$$

where a is the round-trip field attenuation, t is the self-coupling coefficient, $n_{eff}(\omega)$, is the wavelength dependent effective mode index, and L is the optical pathlength. $\Phi(\omega_s, \omega_s)$ can also be written as

$$\Phi(\omega_s, \omega_i) = \sum_k \lambda_k \Psi_{s,k}(\omega_s)\Psi_{i,k}(\omega_i) \qquad (7.4)$$

decomposing the biphoton joint spectrum into orthonormal sets of signal and idler wavepacket modes, and the λ_k's are called the Schmidt coefficients, where their square can be interpreted as the generation of a photon pair in mode k. If there are many non-zero λ_k, then there is a large degree of spectral entanglement, low purity, and hence low separability. Fig. XXa shows theoretical joint spectral intensities
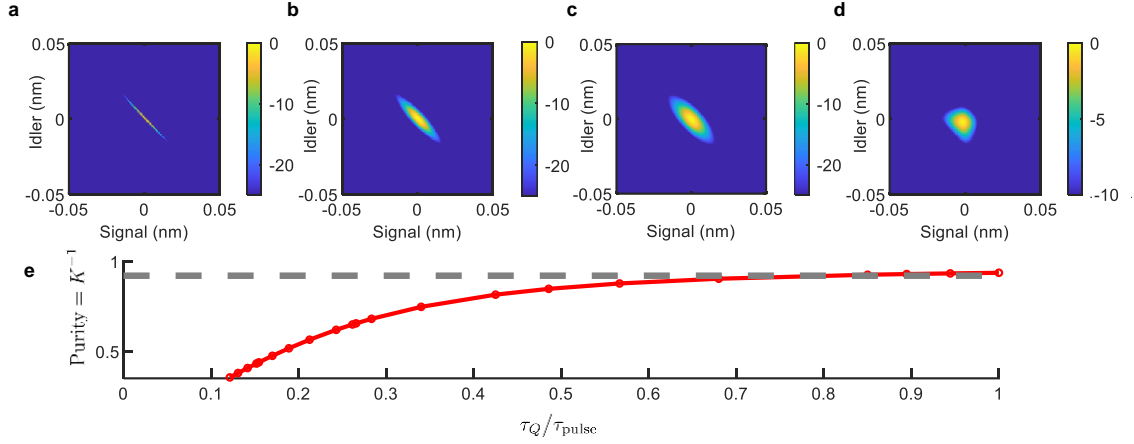
Figure 7.1: (a)-(d) Simulated plots of the joint spectral intensity, from CW (a), 560 ps (b), 320 ps (c), and 80 ps (d). (e) Purity extracted from the JSI pots.)

As noted in the form above, the separability of a biphoton state can be determined by performing a Schmidt decomposition on the joint spectral amplitude [180]–[183], treated here as the square root of the measured joint spectral intensity under an assumption of a flat spectral phase. Numerically, we take a singular-value decomposition (SVD) of the matrix of optical power values shown in the plot of Fig. 7.1 (a)-(d). A commonly used figure of merit describing the degree of entanglement and purity is the cooperativity or Schmidt number, K, where

$$K \equiv \frac{1}{\sum \lambda_n^2} \equiv \frac{1}{Tr(\hat{\rho}_s^2)} = \frac{1}{Tr\left(Tr_i(\hat{\rho}\hat{\Pi})^2\right)} \tag{7.5}$$

and where the Schmidt coefficients, λ_n, are the eigenvalues of the reduced density matrix of the state space. It is equal to inverse of the purity, which defined as is a trace over the squared density operator for the signal channel, $\hat{\rho}_s^2$. The quantum state $\hat{\rho}_s$ heralded by the idler channel is equivalent to the partial trace, Tr_i, over the trigger idler mode ; $\hat{\rho}$ is the density operator describing the biphoton state, and $\hat{\Pi}$ is the measurement operator describing the trigger-photon detection process of the single photon detector. K takes the value of 1 for the perfectly unentangled pure state. From the density matrix perspective, $K = 1$ means that tracing over the idler photon's state

104

space does not decrease the information about the signal photon. On the other hand, a biphoton state with a non-circular diagonal joint spectrum measurement will be projected by the measurement operator $\widehat{\Pi}$ into a mixed state. Performing (eq K) on the theoretical JSI's from (Fig) leads to (Fig..) from which (Main article fig.) is constructed, showing the increase in purity as the pulse width approaches the photon lifetime of the microring resonator used to generate the photon-pair, reaching the theoretical maximum of ≈92% purity.

7.2 Chip Design

The starting silicon die was fabricated from a 300mm silicon-on-insulator wafer from Sandia National laboratories, where a final CMP process thinned the oxide layer between the silicon waveguide and thin film lithium niobate. Ellipsometry data collected over the wafer is shown in Fig. 7.2 (a), showing the oxide height map. The oxide height for the selected die, shown by the dotted rectangles, is used to simulate the RF modes for the Mach-Zehnder modulator designs.
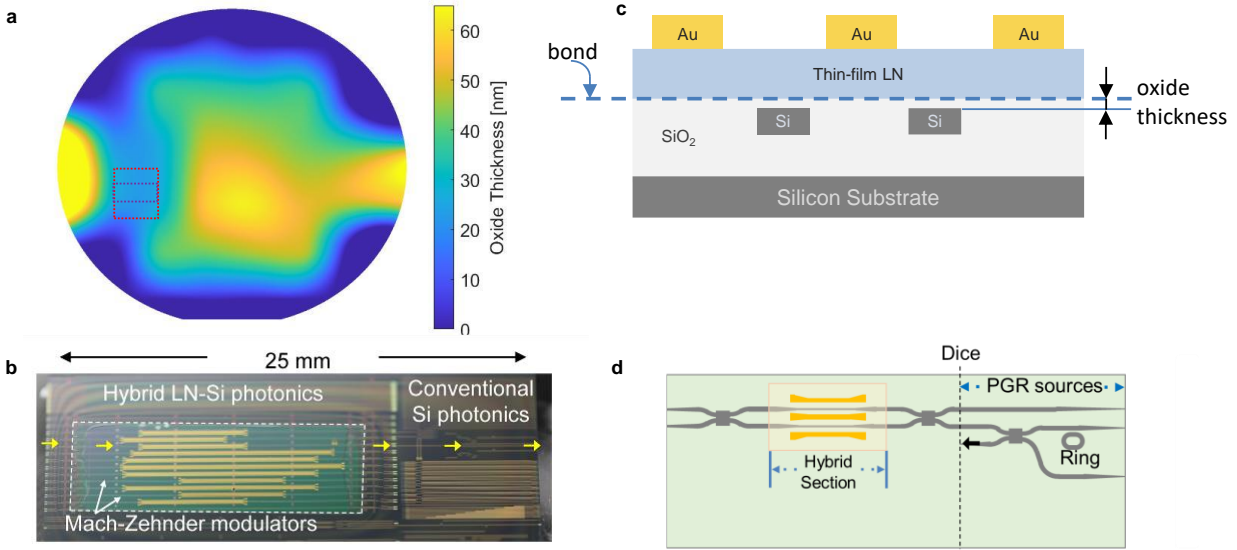
Figure 7.2: (a) CMP oxide height map. (b) Picture of hybrid LN-Si photonic chip, showing the regions of high-speed modulators and conventional silicon photonics. (c) Cartoon cross section of material layers. (d) Cartoon drawing of layout of the chip.

Fig. 7.2(b). shows a picture taken of the selected die. The yellow arrows mark the regions where the laser propagates from the into the hybrid LN-Si region and is modulated, back into the silicon waveguide regions, and into the area of the die where the conventional silicon photonic devices were designed. As shown in the cartoon in Fig. 7.2(d)., the laser propagates through a region with some test ports and into the ring designed for photon-pair generation and exits the chip through fiber couplers.

There are two distinct material regions. The first is where phase shift, modulation, and active voltage control of light is needed, the chip layer stack consists of materials shown in the last chapter by the cross section in Fig. 6.1(d), labeled as "cross section C". The second is where optical routing, splitting, filtering, and parametric generation of photons, here from spontaneous four-wave-mixing (SFWM), is performed, and the chip layer stack consists of materials shown by the cross section in Fig. 6.1(b), labeled as "cross section A". In both cross sections, only silicon is etched, but in cross section C, a die of thin-film lithium niobate (here 600nm thin) is bonded on

top regions where it is needed (after the wafer silicon processing was completed) through a direct bonding process (described in our prior work [10]) to define the hybrid silicon-lithium niobate mode.

Metal electrodes deposited on top of the cross section C region are used for applying voltage to control the optical phase. A microscope image of the high speed electrodes used for this chip is in Fig. 7.3(b), showing the segmented traveling wave electrodes for the Mach-Zehnder modulator (MZM). The control of the RF mode provided by the segmented electrode allows close matching of the RF phase and optical group velocities, while improving the modulation efficiency from our prior work—here the VpiL was measured to be 3.2 Vcm. About 85% of the mode area in this hybrid mode is in lithium niobate. Fig. 7.3(e) shows high speed measurements showing the 3 dB electro-optic frequency response of the modulator, showing a 3 dBe bandwidth of about 110 GHz. The frequency response was measured by a high resolution optical spectrum analyzer. The extinction ratio of the MZM was about 20 db.
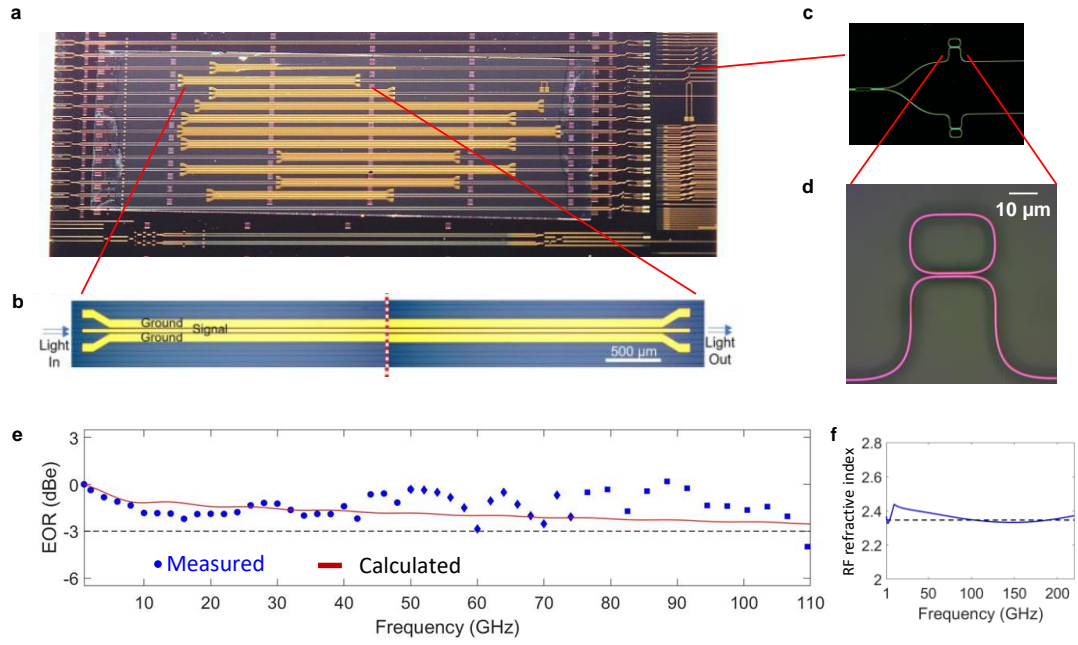
Figure 7.3: (a) Optical image of the chip under test. (b) Microscope picture zoom in of the electrodes. (c) Passive conventional silicon region. (d) Zoom in on the microring used for pair generation. (e) Plot of electro-optic response of modulator, measured from a high resolution optical spectrum analyzer. (f) RF refractive index vs. frequency.

To transition from regions of cross section B to cross section A and vice versa, low loss tapers of about 300 um are used to convert between the first order transverse electric (TE) 150nm thick, 650 nm wide silicon in region B to the first order hybrid rib loaded TE mode with 600 nm thick TFLN slab over the 150 nm thick, 275 nm wide silicon strip, separated by a thin oxide layer of about 50 nm. After the hybrid silicon-TFLN MZM carves the CW laser light into pulses, the pulsed light is routed back into the single mode TE waveguide in 150nm thick, 650 nm wide silicon with only oxide above and no TFLN, where high performance angled-sidewall silicon MMI's couple the light into a single mode waveguide that connects to a silicon ring resonator for SFWM, shown in Fig. 7.3(d).

7.3 Experimental Results

7.3.1 Setup of Experiment

A method to measure JSI called stimulated emission tomography was developed in [184], where it was proven that the stimulated four wave mixing spectrum shares the same joint spectral amplitude of photon pairs in the spontaneous four wave mixing case, and has become a dominant method to characterize spontaneous parametric sources [185]–[187]. The measured JSI was acquired by performing stimulated emission tomography by coupling a CW laser at the pump wavelength and a CW laser at the idler wavelength into the chip through silicon photonic edge couplers, after amplifying with a polarization maintaining erbium doped fiber amplifier (EDFA), as shown in Fig. 7.4 .
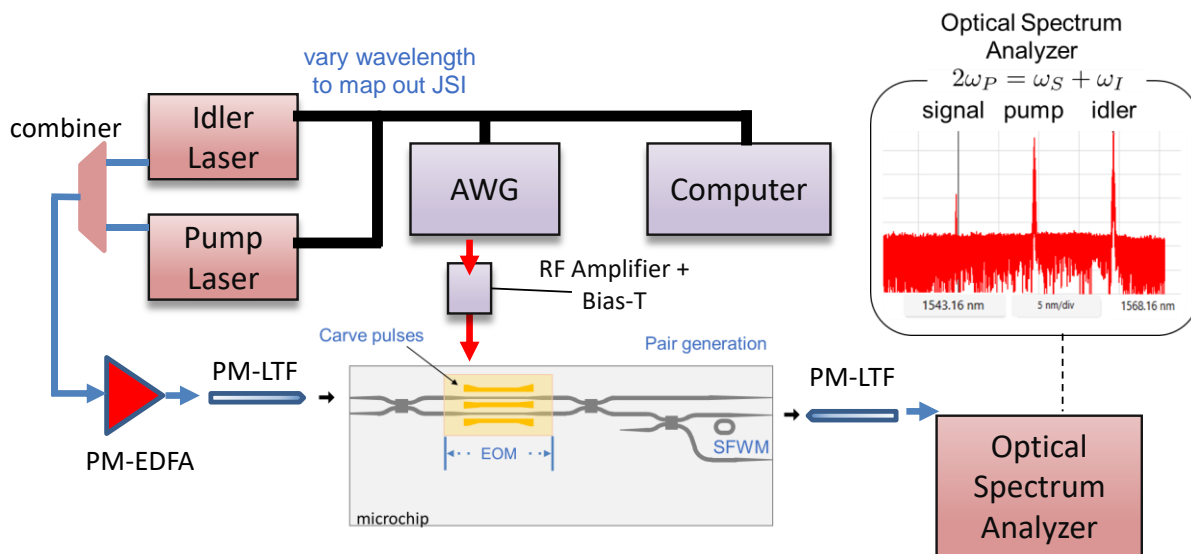
Figure 7.4: Experimental setup for measuring the joint spectral intensity.

The CW pump and idler are coupled into the microchip with a polarization maintaining lens-tapered-fiber into the first silicon waveguide region without lithium niobate (the long feeder silicon waveguides) and into a Mach Zehnder structure through silicon multimode-interferometers, and

carved into pulses by the modulator. A series of experimental measurements were performed to demonstrate the tuning of the joint spectrum by programming an electrical waveform, varying the pulse, until an 80ps (full-width-half-max) pulse is generated to match the lifetime of the microring resonator. An arbitrary waveform generator (Tektronix AWG70000 series) was controlled through a computer in step with the pump and idler lasers, to generate the electrical pulse, and amplified by a high speed RF amplifier and high speed bias T, so that the full $V\pi$ of the modulator could be reached. The RF output was connected to the chip through high speed coaxial cables, contacting the GSG pads on the chip through 110 GHz GSG probes (i110, FormFactor Infinity probe). The stimulated four-wave-mixing light at the idler wavelength was coupled out of the chip onto lensed tapered fibers and into a high resolution optical spectrum analyzer (Finisar WaveAnalyzer) with a 20 MHz spectral resolution.

The idler laser was stepped in wavelength through a span of 0.2nm accumulating a total of 41 spectral measurements on the OSA for each pulse width. The OSA was set to collect across a 40 nm wavelength span, capturing all wavelengths across the signal, pump, and idler, as shown in the inset in Figure 7.4. A high resolution scan over a shorter 2 nm range was then collected for each step. During each measurement, the spectrum of the modulated pump laser was inspected to check if the modulator was biased correctly, and the high-speed bias T after the RF amplifier was adjusted to correct for modulator drifts, requiring a small range of about 0.5 V in adjustment to the DC bias during the span of the experimental measurement time.

7.3.2 Analysis and Data Processing

Raw data collected from two different measurements steps on the high resolution optical spectrum analyzer at the signal wavelength, generated by the pump and seed through stimulated

four-wave-mixing, is shown in Fig. 7.5 (d) and (e), for the 80 ps pulse measurement. A total of forty one measurements of these "slices", for each figure in Fig. 7.5(a)-(c), are collected, spanning 0.2 nm around the microring's resonance closest to the generated signal wavelength, and used to construct the two dimensional image of the raw measured joint spectral intensity of Fig.7.5(a)-(c). The power is normalized to the maximum signal optical peak power measured across all measurements.
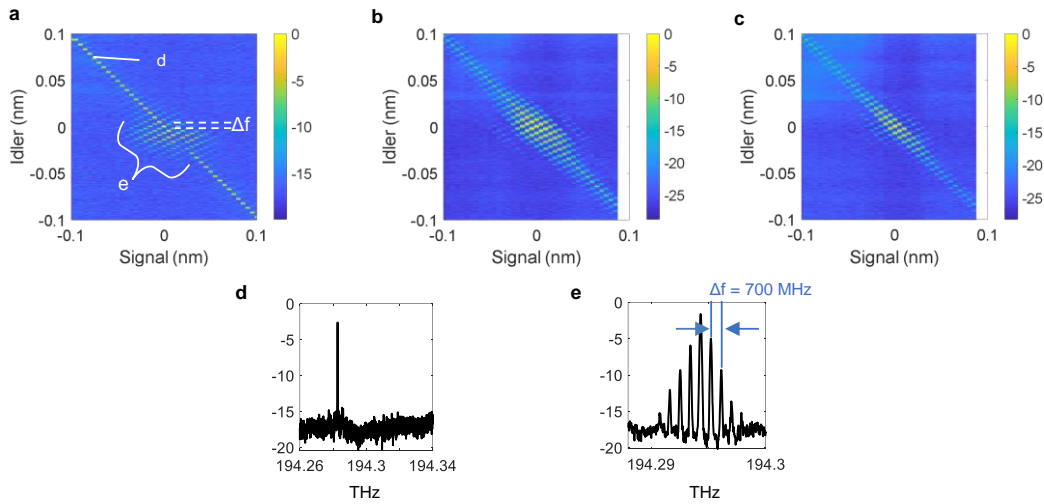
Figure 7.5: (a) raw data collected from the 80 ps pulse measurement. (b) raw data from the 320 ps pulse measurement. (c) raw data from the 560 ps pulse measurement. (d) a single measurement step slice collected from optical spectrum analyzer for the 90 ps pulse measurement, when the laser is far from any ring resonances. (e) a single spectrum slice for the 90 ps pulse measurement when the laser wavelength is at the resonance wavelength of the ring.

Due to the test ports in this device, containing long input waveguides (more than 2000 microns) for testing multiple device across the large die, there is a measurement artifact, the long diagonal stripe marked as "A", coming from the FWM outside the modulator and ring, determined to be generated by the CW light in the long input waveguide. This artifact exists for this particular diagnostic measurement method and test device and would not arise in the lower power regime of degenerate SFWM during pair generation.

To determine the appropriate method of artifact removal, a maximum-likelihood-estimation (MLE) model is created to estimate the possible contributions to the result measured from the optical spectrum analyzer. The parameters of interest are the contribution to the measured result from the CW laser light in the long input test waveguide, and the contribution from the pulsed laser light in the microring resonator. The model is

$$P_{measured}(\lambda) = a_1 P_{CW}(\lambda) + P_{SS}\big(p(\lambda, a_2)\big) \tag{7.6}$$

where $P_{measured}$, the measured optical power spectrum on the optical spectrum analyzer, is given as a sum of a CW interferer at the signal wavelength, P_{CW}, with a parameter a_1 denoting the relative contribution of the CW interferer to the maximum power measured on the spectrum analyzer, and a spread spectrum signal at the signal wavelength, P_{SS}, which is a function of the pulsed light p entering the microring resonator, parameterized by a_2, denoting the lowest optical power of the pulsed light, and gives the extinction ratio of the pulse p. We assume a_1 and a_2 are not wavelength dependent (the model examines only a short span of wavelengths). Thus, this model tests whether the artifact comes from P_{CW} or P_{SS} and quantifies the likelihood of case 1: low extinction pulses with a large CW component circulating in the microring contributing to the diagonal artifact, versus case 2: a strong linear contribution of CW light in the long test waveguide and high extinction pulses with very little CW component circulating in the microring resonator.

Specifically for the stimulated four-wave-mixing case, P_{CW} and, P_{SS} can be written, respectively, as Fourier transformations

$$\mathcal{F}\left\{ S_{CW, 2\omega_p - \omega_i}[E_{\omega_p} e^{j\omega_p t}, E_{\omega_i} e^{j\omega_i t}] \right\} \tag{7.7}$$

$$\mathcal{F}\left\{S_{SS,2\omega_p-\omega_i}[\, H_{ring,\omega_{r,p}}(E_{1,\omega_p}e^{j\omega_p t-jk_p p(\omega_{RF},t)} + \right.$$

$$E_{2,\omega_p}e^{j\omega_p t-j(k_p p(\omega_{RF},t)+\Delta\phi_1)}\,),\quad H_{ring,\omega_{r,i}}(E_{1,\omega_i}e^{j\omega_i t-jk_i p(\omega_{RF},t)} +$$

$$\left. E_{2,\omega_i}e^{j\omega_i t-j(k_i p(\omega_{RF},t)+\Delta\phi_2)}\,)\,]\right\}$$

(7.8)

where $S_{CW,2\omega_p-\omega_i}$ is the generated light at the signal frequency dependent on CW stimulated four-wave-mixing E-field terms $E_{\omega_p}e^{j\omega_p t}$ and $E_{\omega_i}e^{j\omega_i t}$ at the pump and idler frequencies respectively, and $S_{SS,2\omega_p-\omega_i}$ is the "spread-spectrum" light generated by stimulated four-wave-mixing inside the microring at resonance ω_r, with circulating field function H_{ring,ω_r} dependent on pulsed stimulated four-wave mixing and a function of E-field terms E_{1,ω_p}, E_{2,ω_p}, E_{1,ω_i}, E_{2,ω_i}, inside the Mach-Zehnder modulator arms at the pump and idler frequencies respectively. $p(\omega_{RF},t)$ is the pulsed RF waveform at RF frequency ω_{RF}, t is time, k_p and k_i are the wavevectors at pump and idler, and $\Delta\phi_1$ and $\Delta\phi_2$ are the phase offsets in the modulator arms at the pump and idler, respectively. Differences between E_{1,ω_p}, E_{2,ω_p}, E_{1,ω_i}, E_{2,ω_i}, $\Delta\phi_1$ and $\Delta\phi_2$ lead to finite extinction, and can be parameterized by a_2, leading to a simplified form

$$\mathcal{F}\left\{S_{SS,2\omega_p-\omega_i}[\, P_{r,p}(a_2)\,,P_{r,i}(a_2)]\right\}$$ (7.9)

where $P_{r,p}$ and $P_{r,i}$ are the pulse amplitude of finite extinction $10log10(a_2)$ inside the resonator at the pump and idler frequencies.

The joint spectrum generation process using MATLAB described in section 7.1 is used to simulate a SFWM model of the form of eq (7.2). A pulse train with 80 ps pulse width at the pump wavelength plus a CW laser at the pump wavelength are added as inputs into the model. The extinction of the input pulse train is parameterized by the variable a_2, and the power in the CW

laser is parameterized by the variable a_1. With the pump fixed at a constant wavelength, the idler and signal spectrum is plotted across a wavelength of .02 nm, and the resultant simulated $P_{measured}$ is recorded for a specific pair of parameters a_1 and a_2. A representative spectrum for the case of high extinction pulses in the microring and large contributions to generated signal from the CW light in the input feeder waveguide is shown in Fig. 7.6(a), while a representative spectrum for the case of very low extinction pulses in the microring and very low contribution to the generated signal from the input feeder waveguide is shown in Fig. 7.6(b)., with both spectra regridded and interpolated into a coarser grid matching the measurement resolution.
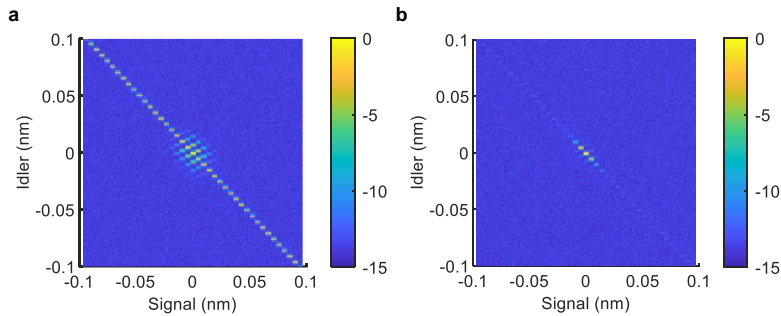
Figure 7.6: (a) a representative simulation of a set of parameters showing a high ER pulse, along with a large CW contribution outside of the microring. (b) a representative simulation with a low ER pulse pumped into the microring.

The maximum-likelihood estimation consists of a likelihood function $\mathcal{L}$,

$$\mathcal{L}(\theta \mid \vec{x}) = p_\theta(x_1, x_2, \dots x_n) \tag{7.10}$$

$$\hat{\theta} = argmax_\theta \, \mathcal{L}(\theta \mid x) \tag{7.11}$$

where $\mathcal{L}$ is a function of the parameter θ, for a given set of data x_i, equal to the distribution p_θ for a specific θ. We seek to find the maximum likelihood estimator $\hat{\theta}$, the parameter set that maximizes $\mathcal{L}$ over all parameter space, given $\vec{x}$, the measurements made, [188]. For the model

discussed earlier, the likelihood function can be expressed as a function of the two parameters we seek to estimate,

$$\mathcal{L}(a_1, a_2 \,|\omega_1, \omega_2, P_{measured}) = p_{a_1, a_2}(\omega_{1,i}, \omega_{2,i}, P_{measured}) \qquad (7.12)$$

where p is a noisy distribution from which the optical power is drawn out of the optical spectrum analyzer, for a given pair of parameters a_1, a_2 that form of the 2D parameter space, of which $\mathcal{L}$ is a function of to be maximized, and $\omega_1, \omega_2, P_{CW}, P_{SS}$ are the observed data. Thus for the problem represented by model eq. (7.6), we sweep parameters a_1 and a_2 by varying the simulated pulse extinction and CW laser in waveguide contribution power and estimate the likelihood that the actual measured data comes from a distribution of parameters a_1 and a_2, for each step of the parameter sweep.

One common way of comparing the similarity of spectral data to a baseline spectrum is by taking a cross-correlation between the two spectrums [189]. We perform the cross-correlation

$$\hat{R}_{xy}(m) = \begin{cases} \sum_{w=0}^{W-m-1} x_{w+m}\, y_w^*, & m \geq 0 \\ \hat{R}_{xy}^*(m), & m < 0 \end{cases} \qquad (7.13)$$

where W is the total number of wavelengths in one spectrum, w enumerates the wavelength shift step in the cross correlation between single spectrum, and m ranges from 1 to $2W - 1$. The maximal correlation coefficient is taken for each measurement step, and normalized to the square root of the product of autocorrelations of x and y.

Since the measurement noise in measurements drawn from the optical spectrum analzyer is approximately flat and white, a joint likelihood distribution of the gaussian form

$$\mathcal{L}(u \,|\vec{x}) = \prod_{i=1}^{n} \left(\frac{1}{\sqrt{2\pi\sigma^2}}\right) exp\left\{\frac{-[x_i - u]^2}{2\sigma^2}\right\} \qquad (7.14)$$

can be formed for all the measurements, where σ^2 is the variance and u is a parameter model of the system. A relation between cross-relation functions on multiple spectral data and the likelihood

function of the form in eq (7.14) was derived in [190] for maximum-likelihood estimators to detect extrasolar star systems given a spectral template. From [190], a likelihood function for observed spectral data, f_n, and template spectral data, g_n, can be formulated similarly to eq (7.14) as

$$\mathcal{L}(u \mid \vec{x}) = \prod_n \left(\frac{1}{\sqrt{2\pi\sigma^2}}\right) exp\left\{\frac{-[f_n(x_i)-ag_n(x_i-u)]^2}{2\sigma^2}\right\} \tag{7.15}$$

where it was shown that cross-correlations of all measurements with a template (or the parameterized simulation, in our case) can be combined into an effective correlation value that is equivalent to a likelihood function across all data measurements as

$$\mathcal{L}^2_{\hat{R}_{xy},effective}(a_1, a_2 \mid \vec{x}) = 1 - \left\{\prod_{i=1}^n \left(1 - \hat{R}_{xy_i}^2(a_1, a_2)\right)\right\}^{1/n} \tag{7.16}$$

where $\hat{R}_{xy_i}^2$ is the cross-correlation between the spectrum collected by i^{th} measurement step on the OSA for a JSI measurement and the simulated spectrum with parameters a_1 and a_2, and $\vec{x}$ is the measurement data, $\omega_{1,i}, \omega_{2,i}$, and $P_{measured}$. The maximum likelihood estimator is then found by simulating $\mathcal{L}_{\hat{R}_{xy},effective}$ over a two-dimensional parameter space represented by the a_1 and a_2 axis, shown in Fig. 7.7 and calculating eq. (7.16) plotting the value of $\mathcal{L}_{\hat{R}_{xy},effective}$ for each (a_1, a_2) pair. The maximum-likelihood estimator is the red dot in Fig 7.7, showing through a high a_1 value that the CW component from the input feeder waveguide contributes strongly to the measured JSI, and that the extinction is very high (above 20 dB), given by a very low a_2 value.
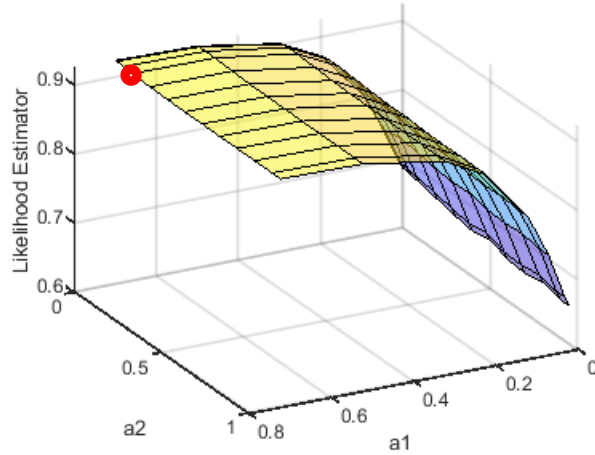
Figure 7.7: A plot of the likelihood function $\mathcal{L}_{\hat{R}_{xy},effective}$, with a1 and a2 parameters representing the relative power contributed from the CW laser in the feeder waveguide and pulse extinction, respectively.

Having established that the maximum-likelihood estimator gives a CW term that contributes linearly to the measurement, we remove the linear term, following standard CW interference rejection techniques in spread-spectrum systems [191]–[193], and subtract P_{CW}. Figure 7.8 (a)-(c) shows the full process performed on simulated data, where the narrowband CW peak estimating the artifact the removed from all measurement slices (each spectrum from each step of an OSA measurement). The peaks of the spectrum of the pulse train are interpolated to give the shape of the envelope. Fig. 7.8 (d) shows the theoretical JSI from a single transform limited 80ps gaussian pulse, which compared the final envelope of the simulated JSI gridded at coarser resolution to match the settings of the OSA, is nearly identical.
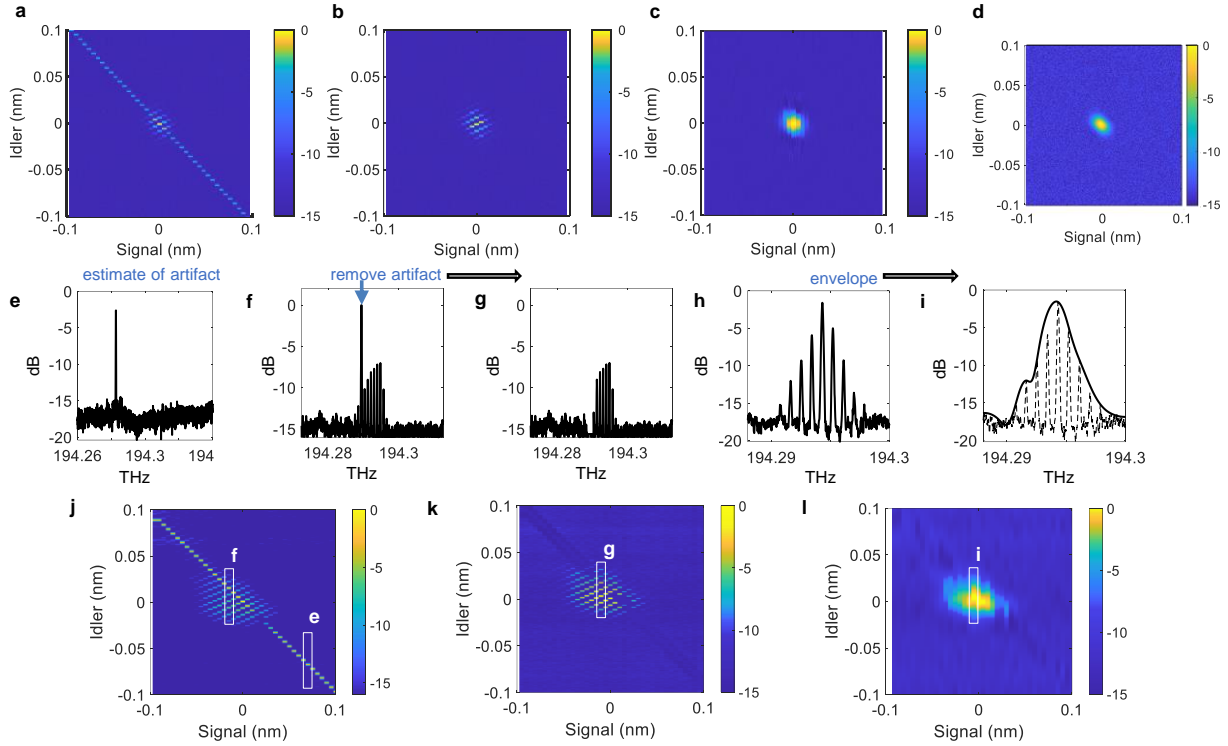
Figure 7.8: (a) Simulated raw JSI with artifact coming from long straight waveguide. (b) Simulated JSI after artifact removal. (c) Simulated final JSI result after taking the envelope. (d) Comparison to analytical theory. (e) A slice of one measurement step, corresponding to the white box in (j) marked with "e". (f) A slice of one measurement step, corresponding to the white box in (j) marked with "f". (g) A slice of one measurement step, corresponding to the white box in (k) marked with "g", after artifact removal. (h) zoomed in view of spectrum analyzer measurement. (i) Result of envelope taken over the spectral lines. (j) Measured raw JSI of 80ps pulse. (k) Measured JSI of 80ps pulse after artifact removal. (l) Final measured JSI extraction.

Fig. 7.8(e)-(i) show a slices of this process performed on a single measurement spectrum from laboratory data taken in the full experiment with the modulator pulses pumping the microring resonator, where the artifact estimation, subtraction, and enveloping is performed to give a final slice of the measured JSI in Fig. 7.8(i). In the experiment, forty-one measurement steps were taken, and all measurements slices collectively contribute to the two dimensional plots shown in Fig. 7.8(j)-(l), where the same post-processing is performed to give the final two dimensional measured JSI of Fig. 7.8(l), on which Schmidt decomposition can be performed.

7.3.4 Experimental and Theoretical Purity

The process described in the prior section is performed on all experimental data, and a Schmidt decomposition performed on the joint spectrum to determine the cooperativity K. The purity, which is the inverse of cooperativity, is plotted in Fig. 7.9. for experimental results from pulses of width 560ps to 80ps, along with an unmodulated CW measurement result.
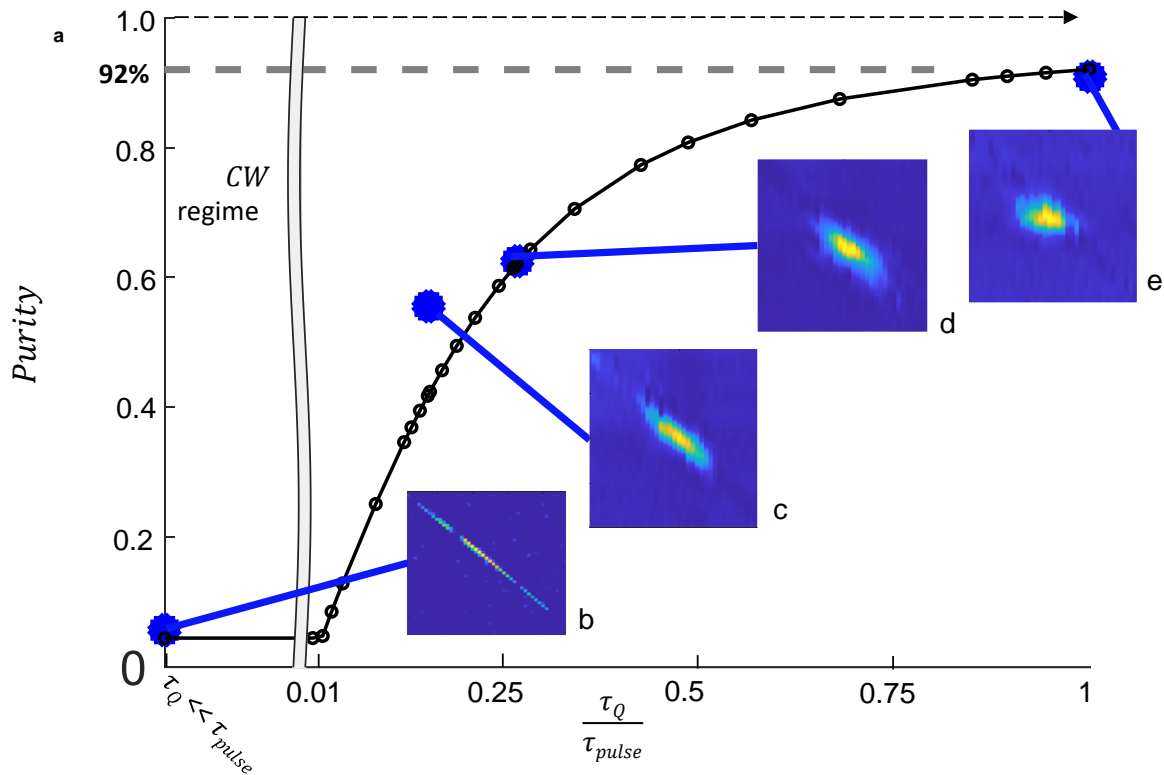
Figure 7.9: Comparison of measured JSI to simulated JSI.

The simulated theoretical purity is also plotted with the measured data and shows close agreement. Fig 7.9 a shows that the theoretical purity for the single bus microring resonator here saturates around 92%, marked by the thick grey dashed line. Both simulation and measurement agree with the limits discussed in Section 7.1.

7.3 Summary and Outlook

We designed and fabricated the first monolithic chip with 110 GHz-bandwidth hybrid thin-film lithium niobate Mach-Zehnder modulators and high-Q silicon microring resonators and silicon photonic circuits—using it to control the joint spectrum of room-temperature photon-pair generation at 1550 nm and reaching the maximum theoretical purity. The theoretical 92% limit in purity in the current demonstration can be overcome by modifications which can be incorporated entirely within the foundry compatible designs on this platform—identified in recent work in parametric sources of quantum light demonstrating several paths to achieving near unity purity. They include: phase matching and dispersion engineering in both SWFM sources [155], [194], [195] and SPDC sources [155], and pump manipulation [196], [197], which can benefit from high bandwidth pulse generation. Common to all these demonstrations is the pulsed pump source, of different types depending on the spectral requirement of the parametric material and architecture, and which so far has been mostly complex laboratory table-top mode locked lasers. The low loss, high bandwidth pump manipulation capabilities in the hybrid silicon-lithium niobate platform we present in this work offers a path in which these advances towards unity purity can be integrated with high performance modulators and high quality chip scale CW lasers [4], [198]. Concurrently, multi-photon sources and higher dimensional entanglement on chip has also progressed: recent chip scale demonstrations of multi-photon entanglement and chip-to-chip quantum teleportation with single coupling point silicon microring sources have shown that complex quantum information processing functions are possible on silicon photonic foundry processes[33]. Moreover, ongoing development in classical photonics demonstrating the largest interconnect and switch fabric capabilities to date continue to compliment broader abilities in quantum photonics from these material [199]–[201].

In summary, we have designed and fabricated the first demonstration of electronically tunable spectral shaping in a single photonic chip. We use foundry level silicon photon pair sources integrated with 110 GHz class thin-film lithium niobate without etching or creating features in the lithium niobate thin film. Our work bridges a high speed, high extinction, and low loss platform with a silicon CMOS compatible foundry process for quantum optics, at room temperature and wavelengths that are compatible with widely available commercial telecommunication products. It combines state of the art performance advances from recent material developments in thin film lithium niobate [9], [121], [123], [125], [126], [128], [202], which has increasingly shown record setting results from nonlinear and spontaneous parametric down conversion[203], [204] to frequency comb generation [128], [205], with a foundry process in silicon that leverages a promising path to scalability [206], [207], and has also led to novel physical phenomena enabled by precision engineering of large area photonic integrated circuits [174, p.], [175], [208]. We demonstrate programmability of a class of room temperature parametric photon sources, reaching the theoretical limit of purity—a timely field of development that has seen parallel advances from the latest demonstrations in on demand quantum sources in optical gain material platforms [20], [31], [209]. We believe the methods we have described in this work offers a path for synergistic advancement in hybrid development for quantum optics, combining best in class demonstrations from different material. This complimentary approach is promising for a wide range of photonic functions from wavelength-shifting of photons and quantum pulse gate operations [177], [210]–[212] to frequency-domain quantum computing and quantum interconnects [17], [213], and can enable scale-up to high dimensionality and complex quantum information processing.

Acknowledgements

Chapter 7, contains material published in: Xiaoxi Wang, Forrest Valdez, Viphretuo Mere, and Shayan Mookherjea, "Monolithic Integration of 110 GHz Thin-film Lithium Niobate Modulator and High-Q Silicon Microring Resonator for Photon-Pair Generation," in Conference on Lasers and Electro-Optics, Technical Digest Series (Optica Publishing Group, 2022), paper JTh6B.9. The dissertation author was the primary author of this paper.

Chapter 7, in part, is currently being prepared for submission for publication of the material. Xiaoxi Wang, Forrest Valdez, Viphretuo Mere, and Shayan Mookherjea, The dissertation author was the primary author, and together with his adviser, led the research efforts for this work.

OpenAI DALL-E's interpretation of "A young Chinese man studying quantum mechanics with his Indian teacher, 1704 (oil on panel)", art courtesy of Luke Schiefelbein.

Chapter 8

Switching Single Photons at High Temporal Resolutions

8.1 Fast and Compact Silicon Photonic Switching of Single Photons with Low Loss

Microchip platforms that generate, control, and route single photons are increasingly benefitting the development of versatile quantum technology platforms [201], [214], [215]. Optical switches are an important building block of these platforms and are often used in communication networks within classical optical applications, but have been limited to slower thermo-optical or microelectromechanical switching [216], [217] in quantum optic demonstrations. Quantum optic applications often require a switch that is low loss and imparts little noise on the desired photon states. As quantum networks grow larger in size [12], fast and low loss switches need to scale to more nodes. Additionally, for quantum photons in microchip platforms, a switch that is simultaneously fast and low loss can reduce the cycle time of time-bin based quantum information processing, for example, by improving the success rate of two-photon quantum communication protocols [218].

We demonstrate here a resonant silicon photonic based switch that targets 10 GHz clock rate time bins with sub-50 ps time scale switching speeds with low insertion loss. While silicon photonic modulators with tens of GHz bandwidth have been continually developed over the last decade for classical communications [219], for quantum optics, the optimization of device design and performance needs to be investigated in the context of single and entangled photons. Within standard silicon photonic platforms, the refractive index and optical absorption can be controlled by the local density of electronic carriers [47], [220] or using all-optical methods [221]. The former approach is more likely to be suitable in the single-photon regime, due to scattering from strong optical pump beams in the latter case.

In the electronic carrier-driven optical modulation category, there are mainly two types of electronic carrier-driven optical modulation methods which are supported on multi-project wafer platforms: those based on carrier injection in a p-i-n junction and those based on carrier-depletion in a p-n junction. Carrier injection switches and modulators have a waveguide core that is mainly composed of intrinsic (undoped) silicon, which can have low optical loss. However, the speed of such devices is limited by the recombination time of electrons and holes and is limited to below 1 GHz [222]. Faster devices require higher levels of doping, which can increase the optical absorption. Carrier depletion modulators can be inherently faster than carrier injection modulators, and can achieve speeds of several tens of GHz without preemphasis. Since reverse bias junction depletion width based changes to the refractive index have a weaker effect on the light, resonant devices are often used to enhance the effect and fold the optical path length into a more compact footprint [51].

Here, we show that resonant carrier depletion based modulators can be well matched to the photon lifetime of typical photons generated through spontaneous four-wave mixing (SFWM) in silicon photonics and can achieve fast tuning speeds with 10%-90% rise times of 48 ps and with 10%-90% fall time of 34 ps. We show that this performance is possible with optical insertion losses of 0.27 dB for the through port and 0.44 dB for the drop port, measured at the single photon regime. We demonstrate through two-photon interferometric experiments that entanglement is preserved when one of the entangled photon pair is switched through the device, and that the noise measured through single photon coincidence measurements is negligible between the two switching ports. We also analytically investigate the optimization and tradeoffs at the device level within the context of switch fabrics and networks.

8.1.1 Device Design

Fig. 1 shows a cartoon of the four port switch device with two bus waveguides loading a resonator. The bus waveguides are strip waveguides in silicon that support a single transverse-electric (TE) polarization mode. The resonator is a silicon disc, with an narrow strip in the central portion of the silicon etched away in order to suppress higher order modes, leaving a single whispering gallery mode in the disc resonator. The disc is doped with a vertical PN junction operated in reverse bias, with areas near the coupling areas of the bus waveguide to disc free of dopants. Application of voltages V1 at -6.5 volts and voltage V2 at -0.5 volts, leads to the resonant transmission at two different wavelengths as shown from theory in Fig. 8(b). The shift in wavelength is from the differences in modal effective index, at different depletion widths of the two different voltages applied to the reverse biased PN junction. A 2D slice from a 3D drift-diffusion charge solver simulation is shown in Fig 8.1(c). The simulated capacitance for the device was 7 fF.
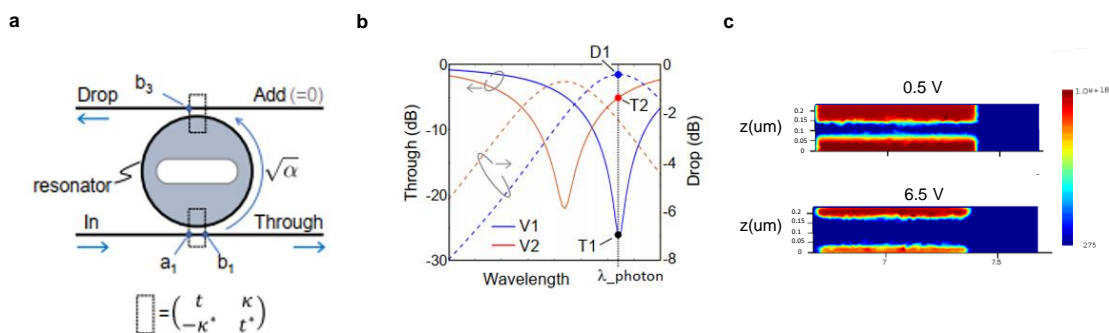
Figure 8.1: a) Drawing of add-drop switch architecture and associated ports. b) Transmission of through and drop port from theory (1D simulation). c) Carrier concentration density plots from 2D slice of 3D drift-diffusion charge simulation at 0.5 V. d) Carrier concentration density plots from 2D slice of 3D drift-diffusion charge simulation at 6.5 V.

The device was fabricated on a 300m silicon photonic process at Sandia National Labs, and has a diameter of 4 um and a height of 230 nm. The n-type dopant (Arsenic, 4×10^{13} cm^{-2}, 70 keV) implantation is performed before the p-type dopant (Boron, 4×10^{13} cm^{-2}, 380 keV)

implantation, and is situated below the p-type. Metal contacts are formed towards the center of the disk away from the optical mode, with low-resistance ohmic contact made from tungsten vias to more heavily p-n doped regions under the contacts.

The resonant device's switching speed is influenced by a combination of the round trip loss in the resonator, the coupling, and the electrical bandwidth from the resistance and capacitance. The device's loss through the drop port and through port is also determined from a combination of these parameters. However, when operating the device as a switch, routing a photon at a specific wavelength through the different ports, the loss at the through port is determined additionally by the wavelength shift from the magnitude of difference in carrier dispersion at the different voltages used for the cross and bar states.

An overlap of the results from carrier concentration simulations shown in Fig 8.1(c). with the bent waveguide mode solved in a 2D eigenmode solver (and verified with the whispering gallery mode solution from 3D FDTD) give the shift in effective index and loss at each reverse bias voltage, and is plotted in Fig 8.2(a). The remaining parameter that determines the through and drop transmission is the coupling strength from the bus waveguides to the disc, kappa, assumed for simplicity here to be symmetric. As opposed to single bus coupled resonators, for a double bus coupled add drop resonator with any amount of loss, increasing the coupling strength will keep increasing the resonant extinction of the through port and increase the transmission at the resonant peak wavelength of the drop port response. However, as Fig 8.2(d)-(e). show, the full-width-half-max (FWHM)) of the transmission peaks and valleys will increase, broadening the resonance (lower quality factor, Q), and as will be discussed next, a tradeoff must be made with the amount of wavelength shift that the difference between the two operating voltages is able to provide.
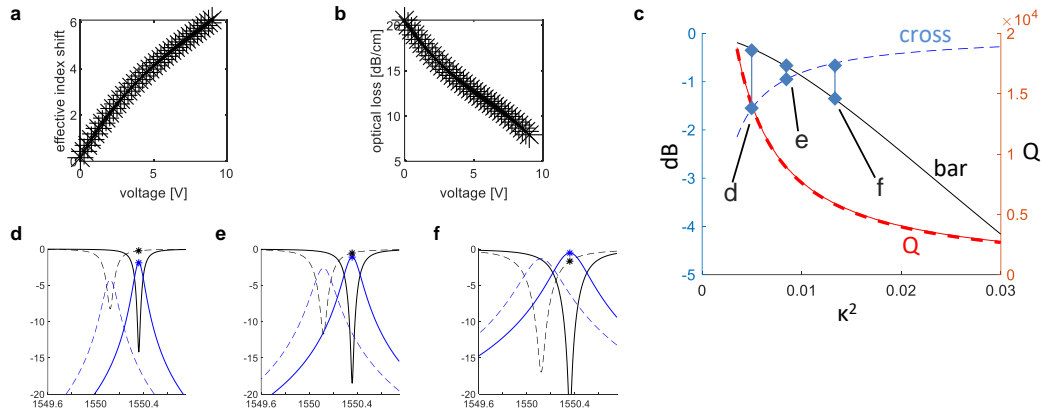
Figure 8.2: (a) Effective index shift from 3D device simulation. (b) Optical loss of the optical mode versus reverse bias voltage at the PN junction. (c) Insertion losses at the through (bar) and drop (cross) ports from loss and index shift simulations with the cross state at 9 V and bar state at 0 V. Points d-f represent the losses calculated at the operating points for different coupling strengths

8.1.2 Optimizing For Drop and Through Insertion Losses

For an add drop resonator cross bar switch, the cross (drop) port insertion loss improves as the coupling strength is increased. For a given dopant setting, since only the coupling is changed, the wavelength shift from the plasma carrier dispersion remains the same, and the wavelength at which the drop port is resonant, and maximum, will have more insertion loss going out the bar (through) port. There is a value of κ for which the bar and cross ports are equal—e.g., the label "g" in Fig. 8.2(c). marks the insertion loss point where both the drop and through losses are < 1dB. Regimes of κ less than it's value at "g" will have lower bar (through) port insertion losses than cross (drop) port insertion losses, while to the right, where values of κ are greater than it's value at "g", the bar port will sharply decline. The insertion loss of the cross port will gradually improve. Often, the insertion losses of different ports (and paths) need to equalized. For single photon transmissions without amplification, the lower loss paths will need to be attenuated to equal the worst case loss path. For a single crossbar switch, the point at which the cross port insertion loss

equals the bar port insertion loss may be used as the optimal worst case loss. Other cases, e.g. in a fabric of many crossbar switches or a network, will be considered in section VII.
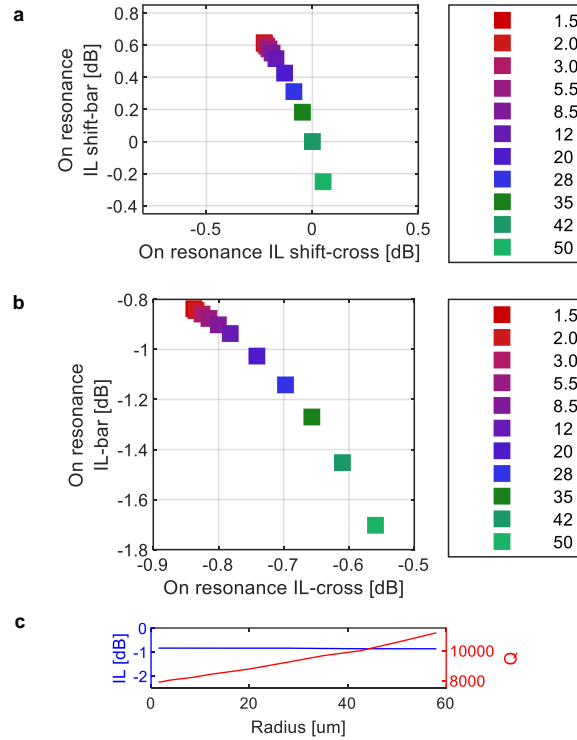
Figure 8.3: (a) The change in the off-resonance through-port insertion loss vs. on resonance drop-port insertion loss, calculated for microring resonators with different radii, normalized to their values for a radius of 42 um. (b) The absolute insertion losses for the simulated microdisc resonator at different radius, (c) Insertion losses for which cross and bar state insertion losses are equal (represented by the point "g" in Fig. 2 c) for different size microdiscs.

Small diameter resonant switches typically have lower capacitance and RC time constants for high speed modulators and wider free spectral range. However, it is necessary to consider also the insertion loss tradeoffs of resonant switches of different sizes when used as single photon switches. A numerical calculation of the switching behavior of a ring resonator, with parameters extractd from a 3D PN junction simulation, showing the tradeoff in the insertion losses between the through (ILBar) and the drop(ILDrop) is plotted in Fig. 8.3(a).—each point represents calculations of ILBar and ILDrop for a chosen value of the resonator radius R and doping

parameters. Different colors are used to indicate different values of R; the range of doping variations considered here only result in a small spread of the points. The reference point, (0;0), is taken as the calculated (ILBar;ILDrop) values for R = 42 µm so that the improvement or penalty for other values of R can be directly read off the graph. These results show that resonators with a small radius can achieve a large improvement in ILBar with a small penalty in ILDrop.
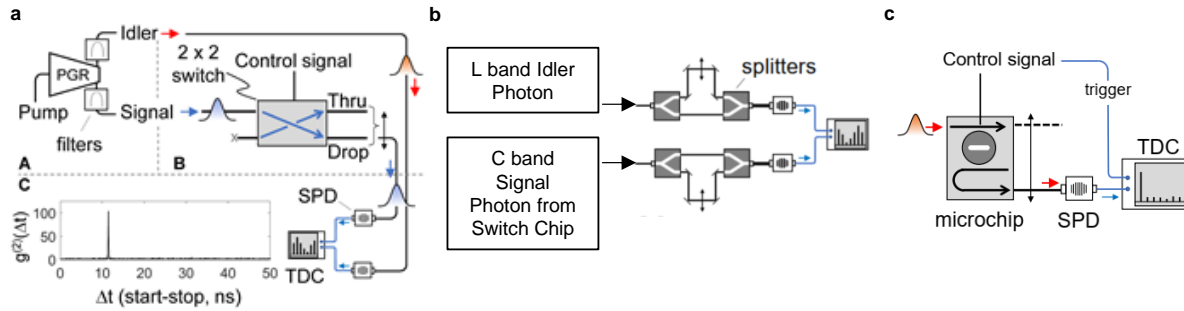
Figure 8.4: (a) Diagram of the experimental setup to measure CAR. (b) Cartoon of setup used to measure the two-photon interferometric visibility using a Franson interferometer. (c) Experimental setup used to measure the time domain response for calculating the rise-fall times at the single photon level.

To determine the tradeoff of insertion losses for the disc modulator with a vertical PN junction, which can made with a very small radius, the changes in insertion loss and effective index experience by the disc's whispering gallery mode from 3D device solver simulations are used to calculate the insertion loss, scaling the overlap of the 2D mode and 2D slice of the 3D device simulation with optical path length (round trip circumference). Fig. 8.3(b) shows the simulated insertion losses for a device with a constant Q factor, the target of which should result in a spectrum that is broader than the bandwidth of the SWFM single photon, and allow fast enough switching speeds. The trend of Fig 8.3(a)'s numerical theory is verified by the trend of Fig 8.3(b)'s 3D simulation with the device designed, showing the improvement in the off resonance insertion loss at the through port while trading off drop port insertion loss, while keeping both insertion losses < 1 dB. Furthermore, Fig 8.3(c). shows the insertion loss across different radii at which both drop

and through port losses are equal, as was illustrated visually by the point "g" in Fig 8.2(c)., for the results from simulation, while letting the optical Q factor vary. While the insertion loss at which drop and through losses are equal improves a little at the smaller radius, the Q factor is significantly lower, and can allow for faster switching and handling more optically broadband photons.

8.1.3 Experimental Setup

To study the resonant switch while actively switching single photons coming from an entangled photon pair source, we used our previously studied source devices [133], [153] to allow a full characterization of the switch at the single photon level and with entanglement. This kind of SFWM source can be easily integrated on the same microchip as the switch.

Fig. 8.4 (a) shows the experimental setup used to perform the first set of experiments to characterize the coincidences-to-accidentals ratio (CAR) for the cross and bar states. This experiment is performed in order to show that the switch adds negligible noise and that there is still high temporal correlation between the switched photon from the photon pair and the other photon in the pair, used as a timing reference.

First, a CW laser at the pump wavelength around 1560.5 nm was fiber coupled into the entangled photon pair source microchip to generate entangled photons at 1550.5 nm (signal) and 1570.5 nm (idler). These photons were fiber coupled out of the entangled photon pair source microchip, demultiplexed, and filtered by narrowband optical filters to suppress laser amplified spontaneous emission noise. Signal photons were fiber coupled and sent through the switch chip, whereas the idler photon bypassed the switch chip for the following two-photon measurements. Detection was performed using efficient and low-jitter cryogenically-cooled superconducting single-photon detectors (SNSPD) with cryogenic amplifiers. The time stamps were then recorded

by a time-to-digital converter. Digitally-generated electronic control signals generated by an arbitrary waveform generator (AWG) drive the switch between cross and bar states with about 6V voltage swing in the reverse-biased regime, without significant current flow. No pre-emphasis was used.

Fig. 8.4(b) shows the experimental setup used to perform the second set of experiments to show that entanglement is preserved through the different ports of the switch chip. A two-photon interference measurement using a Franson interferometer is set up by sending the C band signal photon coming out from the switch chip through a delay-line interferometer (DLI) with voltage controlled phase tuning and detected by one single photon detector. The L band reference photon is coupled into a second DLI identical in pathlength to the first DLI, and detected by a second single photon detector. Both photons are time-tagged by a high resolution time-to-digital converter that records the time of arrival.

Fig. 8.4(c) shows the experimental setup used to perform a third set of experiments to characterize the switching speed of the resonant disc cross-bar switch. For this experiment, the single photons of about 80ps were obtained from heavily attenuating modulated pulses from a CW laser, to reduce the source jitter in order to characterize switching speeds below 50 ps. Enough attenuation was used to ensure that multi-photon probability per pulse was less than 3%. An electrical control signal generated by a high speed AWG also served as a reference trigger for the time to digital converter, and only one single photon detector was used to detect the switching waveform from the stream of single photons coming from the switch chip. Single photon time domain oscilloscopy was used to perform high timing resolution measurements of the switch speed at the single photon level [223].

8.1.4 Experimental Results

From the experimental setup described in Fig 8.4 (a), a series of histograms is recorded for varying optical powers. Fig. 8.5(a) shows the CAR calculated from each power level, corresponding to the single photon count rates in the x-axis of the plot. We find high CAR rates, scaling across increasing power following conventional trends described elsewhere [224]. Both cross and bar states show high CAR with similar trends, and negligible difference.

The results of the two-photon interference measurement taken from the experimental setup described in Fig. 8.4(b) is shown in Fig. 8.5(b). The lower panel verifies that the singles counts from both channels were stationary as the phase of the Franson interferometer was scanned by stepping the voltage on the DLI [142]. The two-photon coincidence counts as a function of the scanned phase are shown in the upper panel. The data visibility was 99%, and the fitted (R2=0.83) visibility was 92% (well above the Bell-Clauser-Shimony non-classical limit ~71% for both cases) establishing the entanglement of the light switched by the device.
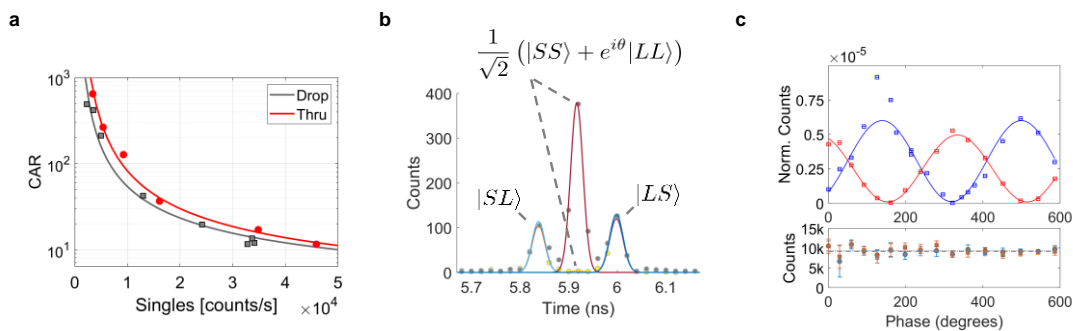
Figure 8.5: (a) CAR measured for switched signal photons collected from the Bar (Thru) and Cross (Drop) port, with the idler photons. (b). Two-photon coincidence interferometry in an (unfolded) Franson interferometer; The visibility is 99% (92%) for raw data (fitted). (c). Time stamped histogram showing three peaks in the time-resolved measurement at two phase settings.

Figure 8.6. shows the 10%-90% rise and fall times of the switch, measured at the single photon level with the experimental setup described in Figure 8.4(c). The rise time was measured

to be 48 ps and the fall time was measured to be 34 ps. The asymmetry is expected from the carrier dynamics at the reverse bias voltage—for nominal time bins of 100ps, the switch will be fully transitioned by the time that the single photon is expected to be switched through the device.
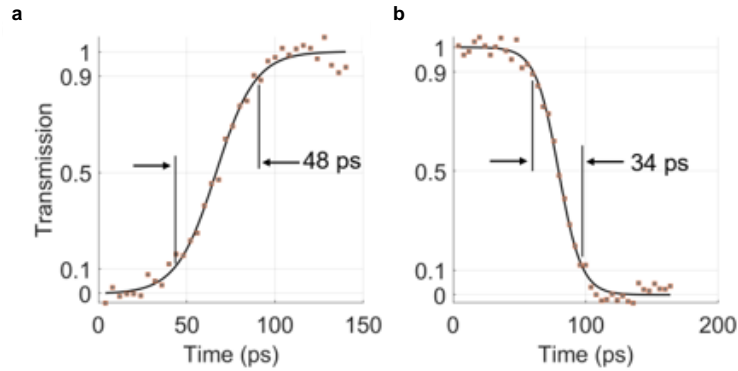
Figure 8.6: (a) Single-photon transmission measured in start-stop mode in response to voltage pulses, indicating the 10% and 90% levels for the rise time. (b) Fall time measurement 10% and 90% levels.

8.1.5 Insertion Loss Characterization

The scaling of electro-optic switch device to larger number of cascaded switches depends on the insertion loss of the switch in both the cross and bar states. To characterize the insertion loss of the switch through both ports accurately at the single photon level, a test device is designed to loop the drop port back into the disc resonator, allowing storage of the single photon inside this loop. Fig. 8.7(a) shows a diagram of the loss measurement loop, where a control voltage pulse from the AWG captures a photon from the bus waveguide into the storage loop. After a programmable delay, a second electrical voltage pulse releases the stored photon from the loop to the output port. The photon recirculates in the loop with gradual loss from absorption, through port, and drop port insertion losses. The loop storage time was about 100ps. Here, pulses were

carved with an external high extinction ratio (29 dB) modulator, with a repetition rate of 10 MHz and a pulse duration (full-width at half-maximum, FWHM) of 80 ps.
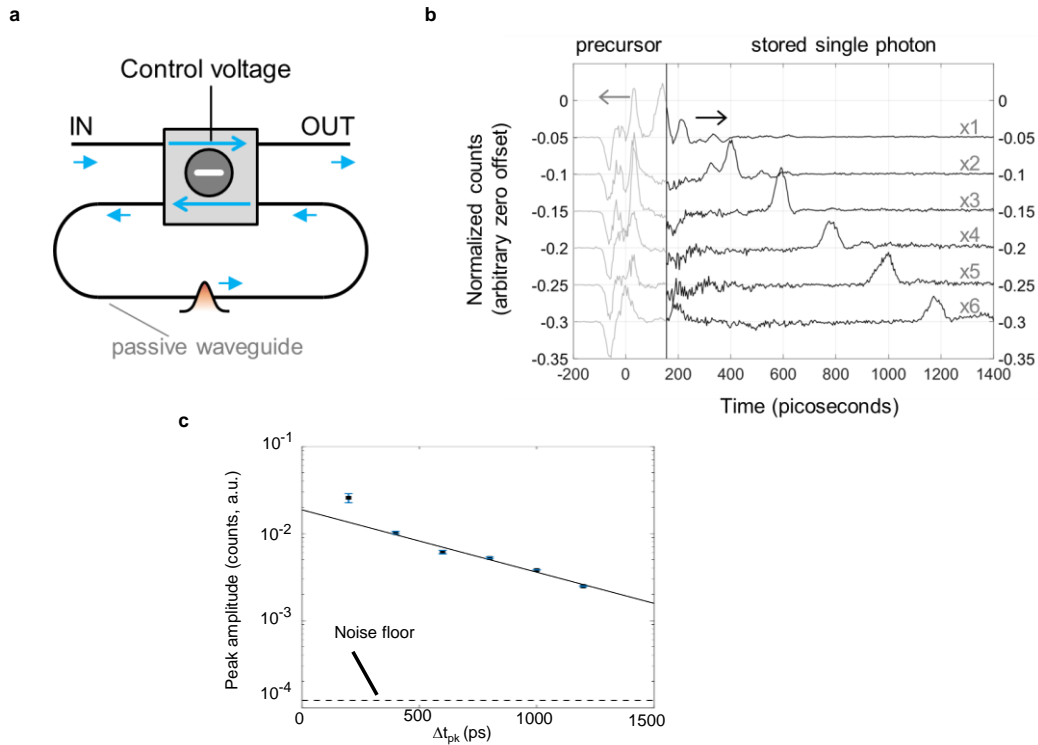
Figure 8.7: (a) A diagram of the loop structure used to measure insertion loss. (b) Data after baseline subtraction for storage times of 200 ps, 400 ps, 600 ps, 800 ps, 1 ns and 1.2 ns. For clarity, traces are offset vertically and multiplied by the indicated integer. (d) The peak amplitudes are plotted versus the programmed delay.

Fig. 8.7(b) shows a series of photon storage and release events at different storage times up to over 1 ns. The photons released after the variable programmed delays are detected on a single photon detector. Because there is an electrical reference trigger with every store and release pulse, setting the start-top times to the differences between the reference trigger and single photon detection even will results in a histogram of peaks corresponding to the release of stored single photons. It should be noted that although the histogram is a collection of many photons over minutes, the attenuation of the laser (-91.6 dBm average power into the microdisc) ensures that there is only one photon per loop in each store and release measurement. Post processing the

histogram peaks from the time-tag data gives a set of decay per loop round trip. There is an initial peak marked as "Precursor"—due to the deviation from perfect coupling of the photons into the disk. This deviation from critical coupling causes the light that did not make it through the disk to show up on the single photon detectors, resulting in an initial peak. However, the photons that contribute to this initial peak do not physically affect any of the photons circulating in the disk and can be factored out by taking a base line histogram.and subtracting it from the subsequent store and release histograms.

Fig. 8.7(c) shows a plot of the magnitudes of the peaks from the histograms collected in the set of measurements with varied hold time delays. The initial data point is excluded from the fit due to the dominant contribution of the input light leaking directly to the detector without entering the loop. A fit to round trip loss gives 0.72 dB per round trip. A previously calibrated loss coefficient for the passive waveguide gives 0.45 dB, giving a bar state switch loss of 0.27 dB, and 0.44 dB in the cross state.

8.1.6 Optimizing The Device Across Switch Fabrics And Networks

Basic components of Quantum optical networks can include Nx1, 1xN, and NxN switches connecting and rerouting input ports to output ports—with increasingly larger port counts as quantum networks increase in node size and span further distances [225], [226]. Cascades of crossbar switches and can be used as basic elements to construct these types of network topologies and fabrics [199], [227], [228]. While channel equalization is common in classical channels and can be achieved through a combination of amplification to make up for loss and variable attenuation to fine tune the power equalization, Quantum optical signals propagating in these networks cannot be amplified in the way that classical optical signals can. Unequal path losses can

be equalized through attenuation to avoid higher accidental counts (noise). In these circumstances, optimizing across the worst case paths rather than the single switch device needs to be considered more carefully. At the single switch device level, there is an operating and design point where the insertion losses through both ports are equal—but when cascaded or arranged in a switch fabric or network where multiple devices define a path, a device design where the losses through both ports are not equal may result in a lower worst case path loss.
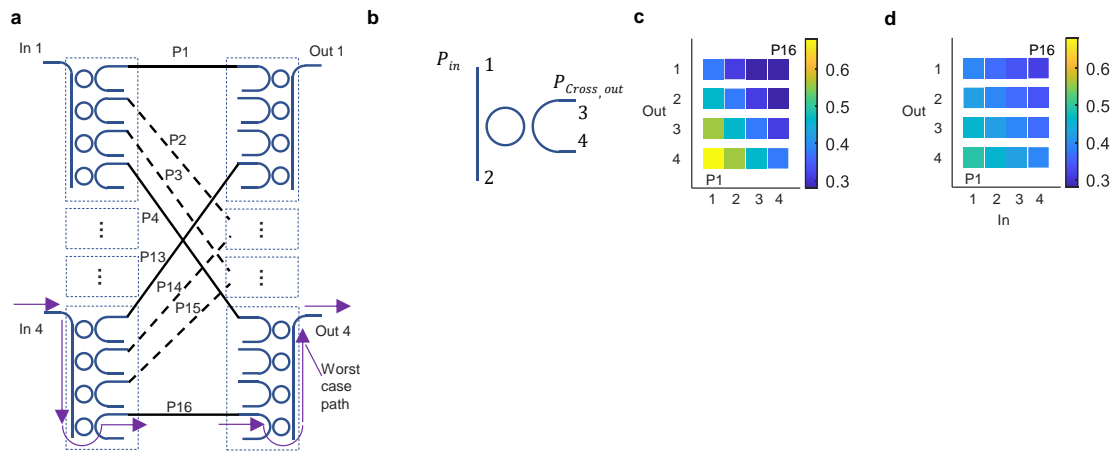
Figure 8.8: A diagram of the loop structure used to measure insertion loss. (b) A diagram of a single crossbar switch, with port names labeled. (c) A colormap showing all possible sixteen paths that can be taken and their respective transmissions (i.e. "P16" is the worst case path with lowest transmission), chosen for a κ^2 that is set to equalize cross and bar insertion losses. (d) A colormap showing all possible sixteen paths for a different κ^2 that does not equalize cross and bar insertion losses, but instead minimizes the worst case path loss. (e) An equivalent NxN without waveguide crossings, which is not strictly non-blocking.

In this section, we first examine the path losses of a NxN strictly non-blocking Benes microresonator switch architecture, studied in the context of classical optics in prior work [229, p.]. A diagram of a 4x4 version of this switch is shown in Fig. 8.8(a). In this all-to-all switch, each input has a set of N microresonator crossbar switches. To route the input to a specific output, only the wavelength selective microresonator crossbar switch that maps to the desired output is tuned so that it's resonant wavelength matches the wavelength of the input light. In this switch topology the insertion loss of the bar port, ILBar, has a larger impact on the total loss of the paths

the light can take in this switch fabric. Note that the possible path losses incurred by this strictly

non-blocking all-to-all switch is the same as a switch topology with reduced switch count, that is

not strictly non-blocking, shown in Fig. 8.8(e), in the limit of very low waveguide crossing losses.

The topology in Fig. 8.8(e) is blocking—however, when the switch speed is much faster than the

average rate photon arrivals, fixed timing schedules [230] can be implemented to address input

blocking issues.

To plot the insertion losses through the different paths from inputs to outputs as device

parameters are varied, a cascade the transmission relations of a single crossbar element through

the sixteen possible paths in the example 4x4 switch is taken, where the outputs at the cross and

bar ports PCross,out and PBar,out (labeled in Fig 8.8(b)) are

$$
\begin{pmatrix} P_{1,out} \\ P_{Bar,out} \\ P_{Cross,out} \\ P_{4,out} \end{pmatrix} = \underbrace{\begin{pmatrix} S11 & S12 & S13 & S14 \\ S21 & S22 & S23 & S24 \\ S31 & S32 & S33 & S34 \\ S41 & S42 & S43 & S44 \end{pmatrix}}_{M} \begin{pmatrix} P_{in} \\ 0 \\ 0 \\ 0 \end{pmatrix} \tag{8.1}
$$

where $S21$ is the power transmission from the input port "1" to the through (bar) port "2", and $S31$

is the power transmission from the input port "1" to the drop (cross) port "3". Ignoring reflections

and waveguide crossing losses for simplicity of analysis here where switch loss dominates, all

other elements in M are set to zero, and the sixteen possible paths formed through selecting the

appropriate cross or bar paths with

$$
B = \begin{pmatrix} 0 & 1 & 0 & 0 \\ 0 & 0 & 0 & 0 \\ 0 & 0 & 0 & 0 \\ 0 & 0 & 0 & 0 \end{pmatrix}, \; C = \begin{pmatrix} 0 & 0 & 1 & 0 \\ 0 & 0 & 0 & 0 \\ 0 & 0 & 0 & 0 \\ 0 & 0 & 0 & 0 \end{pmatrix} \tag{8.2}
$$

selecting the bar or cross state, so that, for example, the path "P16" in Fig. 8 (a) is given as

$$P16 = \begin{pmatrix} P_{16,1,out} \\ P_{16,Bar,out} \\ P_{16,Cross,out} \\ P_{16,4,out} \end{pmatrix} = M_{Out4}M_{In4} \begin{pmatrix} P_{in} \\ 0 \\ 0 \\ 0 \end{pmatrix} \qquad (8.3)$$

where M_{In4} and M_{Out4} are the input stage for the fourth input "In 4" and the fourth output "Out 4" in Fig. 8(a), where

$$M_{In4} = CMBMBMBM \qquad (8.4)$$

$$M_{Out4} = BMBMBMCM \qquad (8.5)$$

so that the total path transmission through all the insertion losses occurred is

$$P_{16,Bar,out} = S31^2 S21^6 \qquad (8.6)$$

Fig. 8 (c) and (d) show the transmission for each of the sixteen paths, for when the coupling constant κ2 is set at equal cross and bar insertion loss in (c), and for when κ2 is set to minimize the worst-case insertion loss for the worst case path ("P16") in (d). This shows that the worst-case insertion loss can be improved by setting κ2 to a different value than the value at which cross and bar insertion losses are the same, at the expense of lowering the best-case insertion loss, but simultaneously making path losses more equal.

To examine the regimes of different insertion loss, κ2 is swept and the results through each path plotted versus κ2. Fig. 9 (a) shows the transmission (equivalent to the snapshot at specific κ2 in Fig. 8 (c)-(d)), of the sixteen possible paths. Note that there are less than sixteen unique combinations of loss (as can be seen by the colormap in Fig. 8), so only a subset of unique values is plotted.
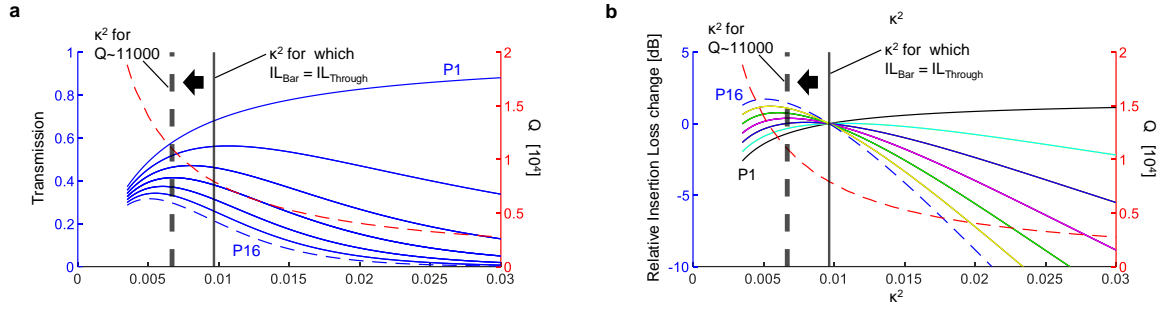
Figure 8.9: (a) A plot of the unique set of path insertion losses in the NxN topology, across varying coupling parameter, κ2. Solid black vertical line indicates the coupling parameter that gives identical cross and bar state insertion losses. Dashed black vertical line indicates the lower bound on the value so that the single phoon photon lifetime is matched to the switch. (b) Data from each curve in plot (a) is normalized to each of its value at which it intersects the solid black line, positive y-values indicate improvement in insertion loss, while negative y-values indicate worse insertion loss.

Each path has a slightly different κ^2 value that results in the lowest insertion loss. The plots of Fig. 9 (a) shows that the global worse-case insertion loss is determined by path "P16", denoted by the dashed blue line. For this worst-case path, designing for a κ^2 value lower than that which equalizes the cross and bar losses especially improves the insertion loss. As Fig. 9 (b) shows, by normalizing the loss through the paths to the equal cross and bar loss point, the worst-case path stands to benefit the most by moving the κ^2 value in this direction, by an improvement of 1.7 dB in the case of the 4x4 switch. One can keep lowering the κ^2 value to improve the loss through the bar state, at the expense of switching speed, but for switching the single photons, as noted earlier, we also desire a switch transmission spectrum that is broader than the bandwidth of the SWFM single photon. For the SWFM photons in this case, the lowermost limit of the κ^2 that we are bounded by is around 0.67% for Q's of about 11000. The change in the κ^2 is from the original value of 0.97% to 0.67%, giving an improvement in the worst-case simulated path insertion loss of about 1.5 dB. The measured values from the fabricated single switch device, in which the bar state loss is 0.27 dB, and the cross state loss is 0.44 dB, show that the measured device's κ^2 values are also in the regime lower than for which the cross and bar state losses are equal. The lower bar

140

state loss would result in a better worst-case path insertion loss for the NxN switches as predicted in the analysis here. While the target regime is achieved in this study, further design iterations on the specific dopant concentration deviations can provide insight on simulation differences in future studies.

8.1.6 Summary

We show the first voltage-driven, entanglement-preserving cross-bar switching element (the foundation of scalable networks [231]) in integrated photonics which is fast enough to achieve reconfigurability of each single photon and addressing of each time bin up to 10 GHz clock rates, four orders of magnitude faster than thermo-optics or MEMS switches. Entanglement is verified through two-photon interferometry experiments through single photon detection, showing high visibility. We find low bar and cross port losses of 0.27 dB and 0.44 dB respectively, and analyze the differences in device level design parameters within the context of switch fabrics. The microchip was made entirely in silicon photonics which is a wafer-scale manufacturable technology [232] and was operated at room-temperature. This result enables high-throughput, high-speed programmable quantum circuits, avoiding long and lossy delays required by slow switches [233].
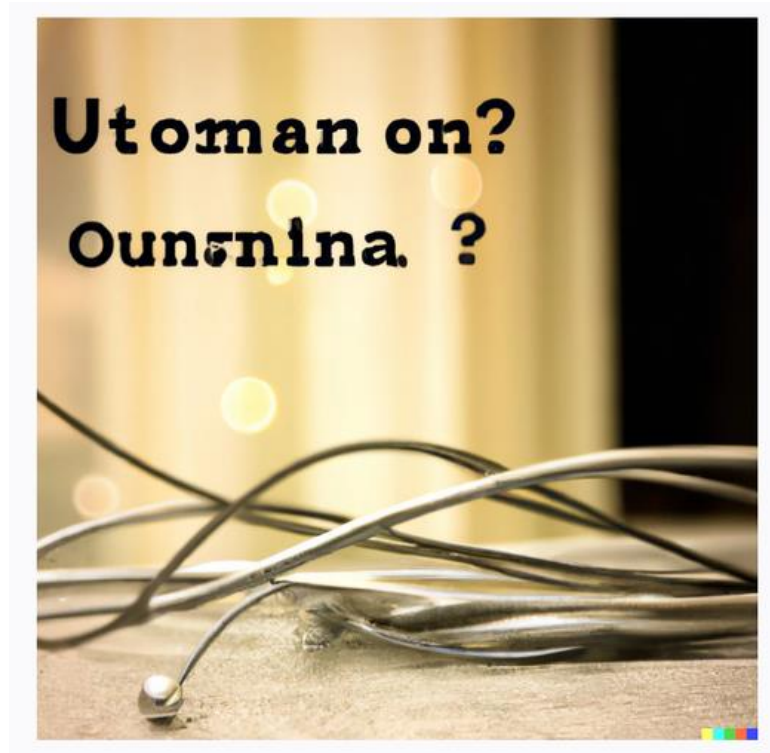
OpenAI DALL-E's interpretation of "Quantum shenanigans", art courtesy of Luke Schiefelbein.

Chapter 9

An Oscilloscopic Method of Capturing greater-than-100 GHz, Ultra-weak optical waveforms enabled by Integrated Electro-Optic Devices

While the generation, spectral manipulation, switching, and detection of single and entangled photons of sub-Poissonian fields were described in the previous chapters, this sub-chapter will describe a novel measurement setup for capturing fast (>100 GHz modulation bandwidth) optical signals in the femtowatt power regime (-100 dBm, approximately) directly in the time domain which can be a useful tool for capturing ultra-fast classical lightwave signals as well. Capturing fast signals at very low power is fundamentally challenging due to the proportional scaling of detectivity with bandwidth. The minimum power of a signal that can be acquired by a state-of-the-art 110 GHz analog bandwidth oscilloscope is about -48 dBm after extensive averaging is performed [234]. For capturing modulated optical signals, the photodiodes which support 100 GHz modulation bandwidth require milliwatt power levels [235], and since electrical power generated by a linear photodiode bears a quadratic relationship to optical power, there is a steep roll-off in performance with decreasing average optical powers. Avalanche photodiodes can have a high gain-bandwidth product, but do not scale to such high bandwidths. Further improvements in optical oscilloscope technology, even with the aid of sophistical electronic signal processing, are expected to be extremely challenging [236], [237].

Here, we show a different approach to capturing modulated optical waveforms capable of scaling to very low power levels, down to a single photon detection event per cycle of a measurement clock, which is typically 80 MHz range in our experiment, but could be faster or slower depending on the input power level and the detector characteristics, as described below. Here, we use recently-developed electro-optic modulators, superconducting nanowire single photon detectors (SNSPDs) and time-correlated single photon counting (TCSPC) electronics, to perform time-domain waveform capture of optical signals at a wavelength of 1550 nm in the femtowatt (approximately 64 fW) average power regime and analog bandwidths exceeding 100

143

GHz. Generally, TCSPC techniques [238], due to their relative simplicity, reasonable cost, and calibration-free nature, are often used in applications such as spectroscopy, ranging, and imaging [239]–[241]. Over the past decade, measurement of signals with up to about 1-10 GHz effective measurement bandwidth has been achieved using available components [234], [242], [243], which is substantially improved upon here by using newly designed and fabricated electro-optic components (Mach-Zehnder modulators and SNSPDs).
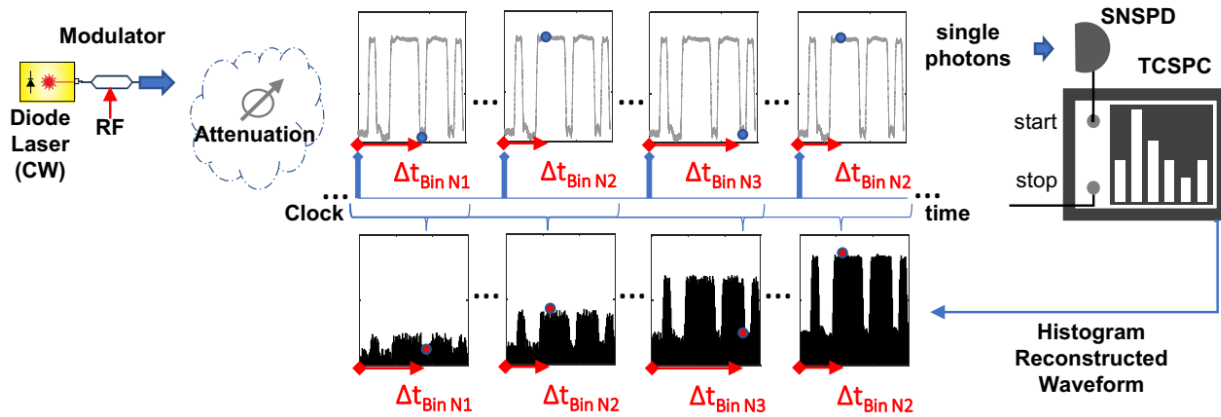
Figure 9.1: Experimental setup and working principle. The optical power after the modulator was heavily attenuated so that the detector detected, on average, less than one photon per clocking window. Detected single photons started the time interval recorded on the TCSPC card until the next trigger pulse from the "Clock" stopped the time interval. The time interval was saved into a list of start-stop time lengths, time-tagging each photon detection event. This list of time-tags was used to build a histogram, which directly reconstructs the modulated waveform.

9.1 High Speed Waveform Sampling By Photon Counting

The instrumentation described here is shown schematically in Fig. 10. Light from a continuous-wave laser was modulated using an electro-optic modulator, which was driven by high-frequency RF signals, which could be either sinusoidal waves or data waveforms depending on the application. For testing purposes, the modulated lightwave signal was attenuated down to an

average power level around -100 dBm, and was detected using a single-pixel superconducting nanowire single-photon detector (SNSPD). Each photon detected by the SNSPD generated a "start" pulse for a TCSPC card. A periodic electrical clock (here, at 80 MHz) was sent to one of the electrical inputs of the TCSPC card, and generated the trigger of the "stop" signal. The clock frequency should be chosen so that there is no more than one detection event in each clock cycle. Thus, a faster clock cycle is required for handling higher input powers by this technique, while keeping in mind that single-photon detectors have a reset time before they are able to detect another photons. On the other hand, it is not a problem to have many time bins with no detection events; these do not contribute to the digital data bandwidth handled by the card. The start-stop time difference Δt_{Bin}, was acquired repeatedly (N1, N2, … labels the time bins) over about 2 minutes, and the resulting histogram reproduced the waveform to be measured. In these experiments, each photon detection event was also time-stamped, in order to characterize the build-up of the histogram over time; however, this is not required in routine operation.

Each event building up the start-stop histogram can be viewed as having been caused, under the correct operating conditions, by a randomly selected photon with uniform probability from the entire waveform. Since the random selection of a Poisson process is itself a Poisson process, the entire waveform should get "fair sampled" over time - without truncation, omission or bias towards either the head or tail of the message.
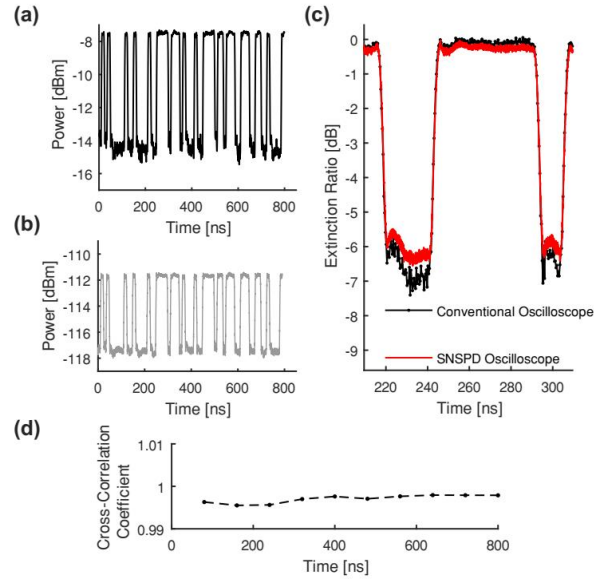
Figure 9.2: (a) Bit sequence detected by a 20 GHz photodiode (optical module in a conventional sampling oscilloscope) at -7 dBm received power. (b) Same bit sequence detected by the single photon TCSPC oscilloscope method after 105 dB additional attenuation. (c) Overlay of the same bit sequence under the two different methods showing high fidelity. (d) Quantitative comparison showing accuracy of replicas.

Fig. 8.11 reports on an experiment demonstrating the concept using standard, commercially available instruments: a conventional 10 Gbit/s lithium niobate electro-optic modulator (EOM), tungsten silicide (WSi) SNSPD and TCSPC card. Here the waveform was measured with a (relatively coarse) resolution of about 25 ps, in order to capture a long end-to-end measurement window. Fig. 8.11(d) compares the detection of a non-return-to-zero (NRZ) message using both a conventional sampling oscilloscope and the start-stop technique. The measurements demonstrate that the individual bits as well as the entire bit pattern were captured with high fidelity, as quantified by the high degree of correlation over both narrow and wide time bases, and without bias, tilt or errors. The average optical power at the detector input of the conventional sampling oscilloscope was -7 dBm (200 μW), whereas it was only -112 dBm (6.3 fW) for our scheme.

146
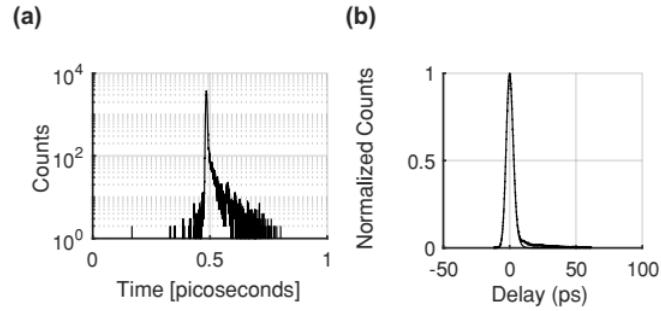
Figure 9.3: (a) The instrument response function (IRF) for the data reported in Fig. 8.10 was measured using a mode-locked fiber laser at 1550 nm wavelength, with a nominal output optical pulse width of 0.5 ps. (b) The raw data, with the mean-value (in time) subtracted out, was fit to an exponentially modified Gaussian function. The fitted value of the full width at half-maximum (FWHM) is 6.32 ps.

To study the modulation traces of the highest RF frequencies that could be captured, the EOM device used in the results reported in Fig. 8.12 was a research-grade hybrid EOM device, in which unetched thin-film lithium niobate was oxide-bonded to silicon photonic waveguides [244], achieving phase-matched operation with >140 GHz 3-dB electrical modulation bandwidth. The modulated optical signals were detected using a low-jitter niobium nitride SNSPD with cryogenic amplification of the detector signal [245], and a customized, high-resolution, low-jitter TCSPC card was used (currently, the highest-reported photon timing resolution, 200 fs). The combination of the SNSPD, amplifier and (room temperature) TCSPC card was measured to have an instrument response function (IRF) of 6.3 ps full-width at half-maximum at 1550 nm as shown in Fig. 8.12, which improves upon previous results.
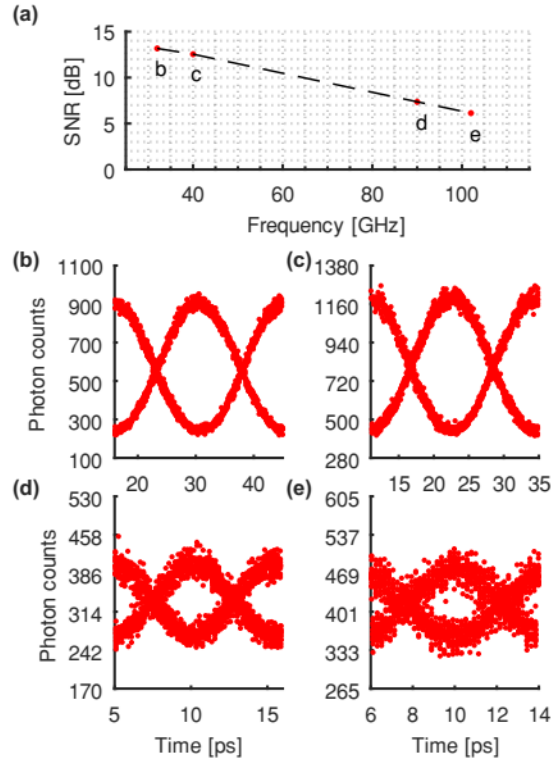
Figure 9.4: (a) Signal to noise ratio (SNR) calculated from the acquired data, captured at an input average optical power of 64 fW and an acquisition time of 120 s in each case, versus various modulation frequencies from 32 GHz to 102 GHz. (b)-(e) Eye diagrams were constructed from the waveforms, with a calculated SNR of 13.2 dB at 32 GHz, 12.5 dB at 40 GHz, 7.36 dB at 90 GHz, 6.13 dB at 102 GHz.

In Fig. 8.13, a resolution of 200 fs was used in the (short time-base) experiments which study the highest frequency (102 GHz) that we can presently capture at 1550 nm wavelengths at the single-photon levels. These modulation frequencies are far higher than the analog bandwidth of commercially available arbitrary waveform generators (approximately 45 GHz), and hence, the test modulation patterns are sinusoidal waves generated from millimeter-wave RF oscillators rather than binary digital data patterns as in Fig. 8.11.

9.2 Experimental Details

In the first lower speed experimental setup, used to compare the fidelity across 100 dBm

differences in optical power, a commercial 10 Gbit/s lithium niobate (LN) electro-optic modulator (Optilab) was used to modulate the light at 1550 nm from an external-cavity tunable single-mode semiconductor laser. The data signal was generated by an arbitrary waveform generator (Keysight), under computer control. After suitable attenuation, the optical waveform was detected using a conventional sampling oscilloscope (DCA-X, Keysight) with a single-mode fiber coupled optical front-end module, and using the readout of a WSi SNSPDs operated in a cryostat at 0.8K (PhotonSpot Inc.) and acquired using a TCSPC card (TimeHarp 260, PicoQuant GmbH) used in a computer workstation. The fiber-coupled, free-running WSi SNSPD has a system detection efficiency, SDE > 90% (due to a resonant cavity design) for 1550 nm and the jitter was estimated to be about 70 ps. The TCSPC card performs, effectively, a 15-bit time-to-amplitude conversion, and has a dead time of 25 ns when used with a time bin resolution of 25 ps. The dead time (25 ns) is therefore substantially smaller than the time window that is captured.

In the second, high speed, experimental setup, a beyond-110 GHz (3 dB electrical) bandwidth electro-optic modulator was used, which was realized using oxide-bonded thin-film hybrid silicon (Si)-LN waveguide technology in the Mach-Zehnder configuration (Vπ = 6.5V). Optical input and output coupling was achieved using tapered single-mode, polarization-maintaining fibers, and multi-axis nano-positioning stages.

The microwave signal was generated directly, for frequencies up to 40 GHz, from a swept-frequency microwave CW oscillator (Anritsu), with a Rubidium clock reference signal at 10 MHz. For generating RF frequencies from 32 GHz - 40 GHz, an RF amplifier (MITEQ) bandlimited to about 26 GHz – 40 GHz was used. For generation of RF frequencies greater than 40 GHz, a multiplier chain was used, consisting of an RF synthesizer, 6x multiplier (AMC10, Millitech) covering the frequency range 75 GHz – 110 GHz (approximately), along with GaAs and GaN

149

amplifiers. The output of the amplifier chain was coupled to a WR-10 waveguide, which was adapted to a 1.0 mm RF cable (for reasons of compatibility with the test station). The RF swept-frequency source also provided a 10 MHz reference, which was used by an arbitrary waveform generator (AWG5202, Tektronix) to generate a steep-transition output trigger at 80 MHz. The mm-wave signal was incident on the modulator microchip using 50-Ω GSG probes rated to 110 GHz. Calibration of the signal pathway was performed using a high-frequency RF power sensor and calibration substrates. The generated signal showed a 50% power drop from 102 GHz to 104.88 GHz and 98% power drop beyond 104.88 GHz; thus, the latter number (approximately 105 GHz) was the highest frequency used in this experiment.

The histogram was captured in the reverse start-stop mode. A free-running NbN SNSPD with negligible after-pulsing and low dark counts (<50 Hz) was used to generate the 'start' signals, whereas the 'stop' signal was generated by a conventional electronic clocking waveform, derived from a stable rubidium time source as described earlier. The SNSPD was cooled below 1K using a closed-cycle Helium-4 sorption refrigerator. Light was coupled onto the detector through free-space windows and filters, using a lens located outside the cryostat. The Instrument Response Function (IRF), from the SNSPD jitter and TCSPC instrumental broadening, was measured to be 6.3 ps full-width at half-maximum, at 1550 nm. An additional, though minor, contribution to the system jitter was the jitter (1.5 ps) measured between the trigger signal and the RF signal driving the modulator. Critical to achieving high resolution is achieving a short and stable rise time (tR) of the SNSPD signal, which is given by the ratio of the kinetic inductance (Lk~ 80 nH) and the sum of the normal domain resistance $R\_N \sim$ 1 kΩ and load resistance $R_L \sim$50 Ω, thus achieving tR ~80 ps. Low-noise RF amplifiers (CITLF1, Cosmic Microwave Technology) were used to

readout the SNSPD signal and were placed on the 4 Kelvin stage of the cryostat. The bandwidth of the RF signal transmitted to the room-temperature electronics card was about 3 GHz.

The output of the RF amplifiers was captured using a PCIe TCSPC module (SPC-150NXX, Becker and Hickl) in a computer workstation. By increasing the TAC transfer ratio (time-to-voltage ratio), a minimum time channel width of 204 fs was obtained, as well as reduced TAC readout noise. High-frequency cables and connectors were not required between the amplifier and the TCSPC board. The electronics converted the time interval between the detection event and the clock signal to a voltage using a calibrated time-to-amplitude converter (TAC) circuit, and the voltage signal was read out by a high-resolution analog to digital converter (ADC). The ADC was not required to operate at the Nyquist bandwidth of the optical signal, since it is only the jitter in the interval between the start-stop events, corresponding to an imprecision in incrementing the appropriate histogram bin, which eventually imposes the effective bandwidth limitation. Increasing the trigger rates in reverse start-stop counting cards can mitigate pileup; here the trigger frequency was set to 80 MHz giving a 12.5 ns period (TTrigger = 12.5 ns). The TCSPC card used in Figs. 8.10, 8.13 and 8.14 required Tdead = 100 ns dead time (regardless of the computer speed), which imposed a limit on the maximum count rate in thse experiments. Future improvements in the dead time of the card would allow higher count rate detectors to be used.

9.3 Signal Extraction and Reconstruction
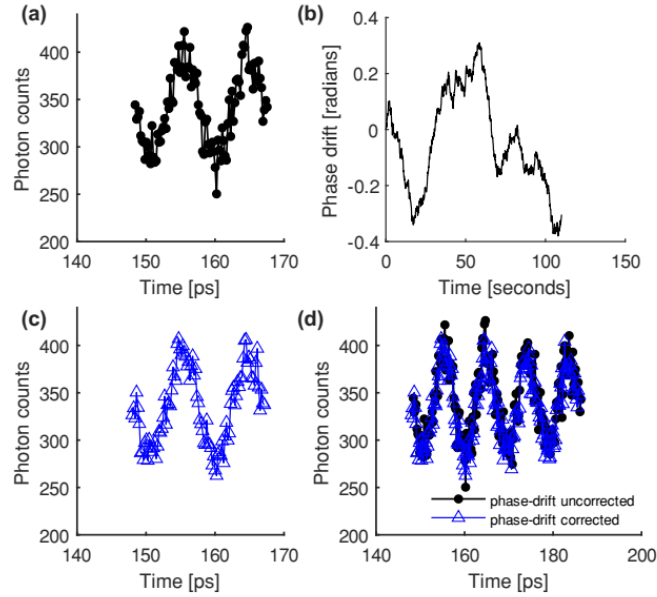
Figure 9.5: (a) Raw waveform prior to phase drift correction. (b) The drift between the trigger and the signal was dominated by a slow variation of the phase over the span of the collection time, with 0.19 radians root-mean-squared (r.m.s.) amplitude. The drift was extracted by sliding a 10 second window by 0.1 second increments over the time-tagged dataset and creating a histogram of the counts in each window, which was then fit to a raised-cosine function. The window was large enough so that a fit could be extracted giving a phase estimate with a 95% confidence interval and standard error smaller than the maximum slope of the phase change per time-step. The phase drift of the 102 GHz signal is shown here. (c) Segment of phase drift corrected waveform. (d) Overlaid waveforms.

In our proof of principle demonstrations, thermal drift of the devices was not stabilized and a slow phase drive in the optical waveform out of the modulator was observed as Fig. 8.14 shows. To correct for the phase drift in the high-speed experiments of Fig. 8.13, the raw measured time-tags of the photon detection events acquired over a typical experimental run of 120 seconds were assembled into 10 second blocks in increments of 0.1 seconds. Each segment was fitted with a raised-cosine function, in accord with the sinusoidal modulation imposed on the thin-film hybrid silicon (Si)-LN electro-optic modulator, using a nonlinear least-squares algorithm. The blocks were chosen to be large enough so that the standard error of the fit was smaller than the slope of

152

the largest phase drift per unit time. The fitted phase-offset term is plotted over the (120 seconds) measurement time in Fig. 8.14, and was seen to vary slowly and by a relatively small amount, less than 0.19 radian root-mean-square of drift. Such slow phase drifts can be due to the lack of bias-point stabilization on the research-grade electro-optic modulator microchip, the noise picked up in the RF cables, or a slow rotation in the state of polarization of the laser light incident on the modulator, which was also not feedback-stabilized.
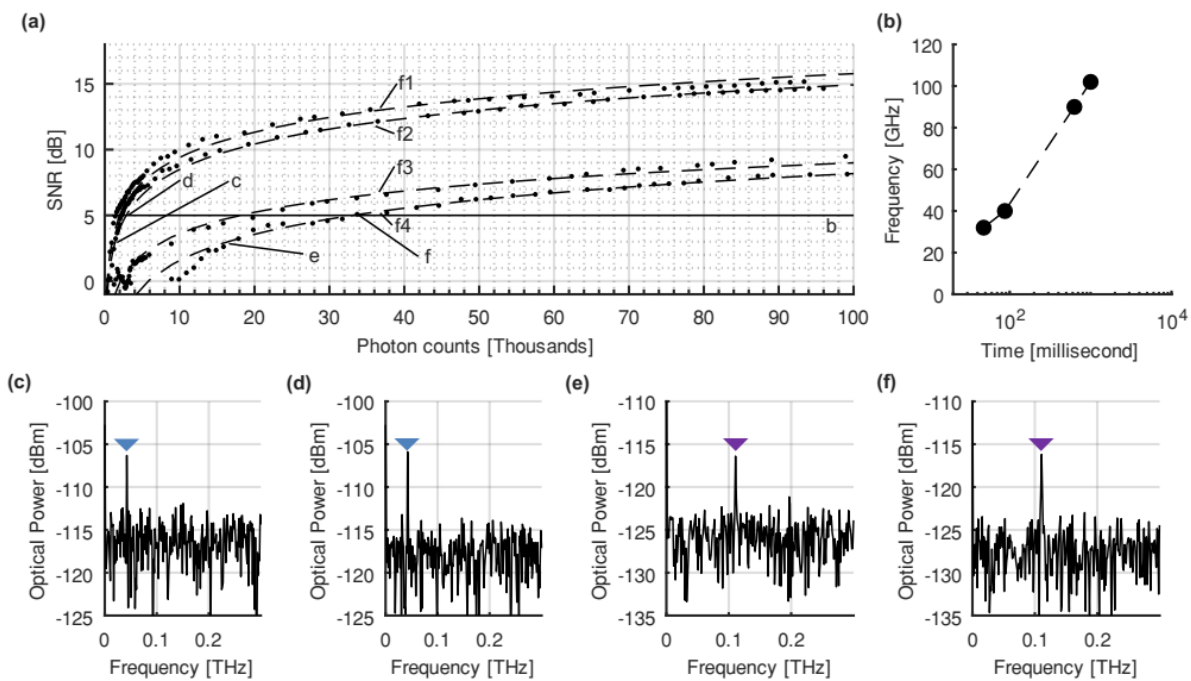
Figure 9.6: (a) The SNR of the frequency-domain peak, identifying the frequency of the sinusoidal wave from the calculated Fourier transform of the measured data, was calculated from snapshots of the data acquired as the measurement gradually progressed. (b) Acquisition time to reach SNR = 5, an arbitrarily-chosen representative value, versus the modulation frequency. (c)-(d) Calculated power spectral densities for 40 GHz modulation at (c) SNR=3, and (d) SNR = 5, showing that the signal peak has been detected and remains the same, whereas the noise floor decreases. (e)-(f) Calculated power spectral densities for 102 GHz modulation at (e) SNR=3, and (f) SNR = 5, showing a similar behavior.

The traces shown in Fig. 4, and those that were processed for the generation of Fig. 8.15, have had this slow phase drift removed from the raw data. The differences between the waveforms before and after phase drift correction are minor, as shown visually, but the waveform with the

153

phase drift removed leads to a more accurate calculation of Signal-to-Noise Ratio (SNR) between different measurements. Fig. 8.13(a) reports the calculation of a figure-of-merit, labeled SNR, defined as the ratio of the mean signal power over twice the standard deviation of the noise power. The SNR was calculated across the entire Nyquist bandwidth of the effective sampling frequency, determined by the duration (200 fs) of a single time bin. The noise signal was computed by the subtraction of the measured data points from a raised-cosine fit to the data (nonlinear least-squares fitting procedure). The fit was performed after phase-drift removal and correcting for time-bin nonlinearity across the measurement epoch (4096 bins cumulatively addressing 0.8 ns). It was verified that a subtraction of the raw data from the line of best-fit did not result in any observable periodicity or identifiable skew in the residual trace, which was therefore, taken as a noise signal for purposes of calculating the SNR. The eye diagram reconstructions were performed by folding over successive segments of the processed waveform onto the same horizontal time base, and are shown in Fig 8.12(b)-(f). In this comparative SNR calculation by successive segmentation in the time domain, the deviation from the raised cosine fit or higher harmonics was not considered, nor was the error margin, and so the SNR here is a lower bound.

9.3 Frequency Domain Characterization

Fig. 8.15 reports the SNR as a function of the number of detected photons, at various RF frequencies. In the frequency domain, SNR is defined differently than in the time-domain traces studied in Fig. 8.13. Here, the SNR is defined in terms of the power spectral density in the frequency domain (consistent with the definition of SNR usually used in the calculation of the effective number of bits, ENOB), and was calculated as the ratio of the signal power to the integrated noise power across the 200 picosecond sampling bandwidth. To calculate the power

spectral density, a fast-Fourier-transform was performed on the entire measurement set of the full acquisition time of the phase-drift-corrected time-domain waveform of whose length was approximately 4096 time-bin samples (minus an appropriate number of time bins to make the data periodic prior to windowing). To estimate the power density spectrum as a Fourier-transform of the autocorrelation function, the accumulated photon counts are first converted to units of power on a linear scale (Watts) by accounting for the acquisition time. This approximates the mean power and a fast-Fourier-transform on the measurement set gives the power spectrum. The noise bandwidth was then taken to be the entire Nyquist-sampling range (i.e., the inverse of the temporal duration of the single bin width, 200 fs), minus a number of frequency bins around the signal equal to one-half of the signal bandwidth. The noise power was estimated by summing these noise bins across the noise bandwidth and weighting the average by a fourth-order central moment of the distribution of noise bins. For a Poisson distribution, the fourth-order central moment was taken as the mean plus three times the square of the mean. With the assumption that the noise floor is spectrally flat, the fourth order central moment was multiplied by a weight term and added to the variance such that the noise floor was taken to be four standard deviations away from the mean. Since the noise floor has a distribution about the average of the noise bins, this weights the upper tail of the noise floor more (decreases the estimated SNR). Finally, the peak value of the signal power spectral density was multiplied by the same number of noise bins as used in the noise bandwidth calculation, and was then divided by the noise power. This approximates the definition of Optical Signal-to-Noise ratio (OSNR) typically used in optical spectrum analyzers to estimate the ratio of peak signal power to the noise floor by taking the data points representing the noise floor a specific bandwidth away from the signal, as in a dense-wavelength-division-multiplexing communication channel.

The capture time, expressed as the number of photons needed to reach a target SNR, is studied in Fig. 8.15. As shown in Fig. 8.15(a), SNR improves in all cases with increased acquisition time. The maximum achievable dynamic range is ultimately limited to about 60 dB, based on the ratio of the maximum count rates achievable from the SNSPD detector (a few million counts per second) to the dark count rate (a few counts per second). Figure 8.15(b) shows the time needed to reach a threshold SNR that is acceptable for identification of the signal from its (Fourier) spectrum. For simplicity, we take the threshold to be SNR=5 dB. Fig. 8.15(b) shows that, at an incident photon rate of about 0.5 MHz, detection of photons over about 6 milliseconds is adequate at fRF = 40 GHz, and the required acquisition time increases to about 150 milliseconds for fRF >100 GHz. Figs. 8.15(c)-(d) show representative examples of the power spectrum of the waveform, identifying the carrier frequency above the noise floor at capture times well short of 120 seconds.

9.4 Summary and Outlook

It should be noted that SNSPDs themselves, like many other single-photon detectors, require time for reset after each detection event; here, the SNSPD reset time was 10 ns but due to AC coupling of the cryogenic amplifier, at least 100 ns was required to avoid detector re-biasing. The average reset time was smaller than the average inter-arrival time of detected photons (approximately 1 μs in Fig. 8.1, and 10 μs in Fig. 8.11) in order to avoid pile-up [246]. Additionally, the combination of multiple detectors addressed through temporal segmentation, along with increased memory, may enable long continuous sequences of data to be acquired. Single-chip-based multi-channel time-to-digital converter systems with adequately-low jitter have been developed [247], which could reduce the cost of a multi-channel system and enable simpler synchronization in the future. The acquisition time can be decreased and seamless coverage of the

temporal window can be achieved by simply parallelizing the TCSPC electronics and using multiple detectors. Although the SNSPD detector is cryogenically cooled, the cost and complexity of closed-cycle cryocoolers is rapidly dropping, and more than a dozen detectors can be housed in a single system. The method described here avoids the Nyquist requirement, i.e., does not require generation or propagation of a signal at twice f_{RF} (i.e., at 210 GHz) anywhere in the instrumentation. Nyquist-rate filtering or scan synchronization is very challenging at these millimeter-wave frequencies, and our method also does not require the RF cabling or connectors to support such a high bandwidth, which would be costly, and difficult to operate and calibrate.

In summary, we have demonstrated, for the first time, the eye-diagram capture of ultra-broadband (greater than 100 GHz bandwidth) modulated optical waveforms at a wavelength of 1550 nm at ultra-low (less than -100 dBm) average power. Achieving these results required the design, fabrication and operation of the broad-band electro-optic modulator, the low-jitter SNSPD detector, and the high-resolution TCSPC card. Building upon our demonstration, we believe that the technology exists today to use state-of-the-art ultra-high-bandwidth electro-optic modulators, low-jitter single-photon detectors, and commercially available electronics to achieve breakthrough performance in sampling oscilloscope technology. Although conventional oscilloscopes may continue to be the most widely used waveform capture modality for routine usage, and sampling or nonlinear based optical oscilloscopes are useful in certain applications, when the input power is relatively high, this complementary technology may be highly attractive when capturing ultra-high bandwidth optical modulated waveforms at very weak signal levels without directly being subject to conventional limitations.

REFERENCES

[1] M. Sysak, J. Johnson, and D. Lewis, "CW-WDM MSA Technical Specifications Rev 1.0." CW-WDM MSA public document, Jun. 04, 2021.

[2] M. Sakib *et al.*, "A 240 Gb/s PAM4 Silicon Micro-Ring Optical Modulator," in *2022 Optical Fiber Communications Conference and Exhibition (OFC)*, Mar. 2022, pp. 01–03.

[3] W. M. Mellette, R. Das, Y. Guo, R. McGuinness, A. C. Snoeren, and G. Porter, "Expanding across time to deliver bandwidth efficiency and low latency," 2020, pp. 1–18. Accessed: Aug. 23, 2022. [Online]. Available: https://www.usenix.org/conference/nsdi20/presentation/mellette

[4] D. Liang and J. E. Bowers, "Recent progress in lasers on silicon," *Nat. Photonics*, vol. 4, no. 8, Art. no. 8, Aug. 2010, doi: 10.1038/nphoton.2010.167.

[5] M. de Cea, A. H. Atabaki, and R. J. Ram, "Power handling of silicon microring modulators," *Opt. Express*, vol. 27, no. 17, pp. 24274–24285, Aug. 2019, doi: 10.1364/OE.27.024274.

[6] E. Timurdogan, C. M. Sorace-Agaskar, E. S. Hosseini, and M. R. Watts, "An Interior-Ridge Silicon Microring Modulator," *J. Light. Technol.*, vol. 31, no. 24, pp. 3907–3914, Dec. 2013, doi: 10.1109/JLT.2013.2278761.

[7] J. Müller *et al.*, "Optical Peaking Enhancement in High-Speed Ring Modulators," *Sci. Rep.*, vol. 4, no. 1, Art. no. 1, Sep. 2014, doi: 10.1038/srep06310.

[8] A. Moscoso-Mártir *et al.*, "Silicon Photonics Transmitter with SOA and Semiconductor Mode-Locked Laser," *Sci. Rep.*, vol. 7, no. 1, Art. no. 1, Oct. 2017, doi: 10.1038/s41598-017-14347-3.

[9] P. O. Weigel *et al.*, "Bonded thin film lithium niobate modulator on a silicon photonics platform exceeding 100 GHz 3-dB electrical modulation bandwidth," *Opt. Express*, vol. 26, no. 18, pp. 23728–23739, Sep. 2018, doi: 10.1364/OE.26.023728.

[10] V. Mere, F. Valdez, X. Wang, and S. Mookherjea, "A modular fabrication process for thin-film lithium niobate modulators with silicon photonics," *J. Phys. Photonics*, vol. 4, no. 2, p. 024001, Apr. 2022, doi: 10.1088/2515-7647/ac5e0b.

[11] S. Paesani *et al.*, "Generation and sampling of quantum states of light in a silicon chip," *Nat. Phys.*, vol. 15, no. 9, Art. no. 9, Sep. 2019, doi: 10.1038/s41567-019-0567-8.

[12] Y.-A. Chen *et al.*, "An integrated space-to-ground quantum communication network over 4,600 kilometres," *Nature*, vol. 589, no. 7841, Art. no. 7841, Jan. 2021, doi: 10.1038/s41586-020-03093-8.

[13] F. Lecocq, F. Quinlan, K. Cicak, J. Aumentado, S. A. Diddams, and J. D. Teufel, "Control and readout of a superconducting qubit using a photonic link," *Nature*, vol. 591, no. 7851, Art. no. 7851, Mar. 2021, doi: 10.1038/s41586-021-03268-x.

[14] M. Saffman, "Quantum computing with atomic qubits and Rydberg interactions: progress and challenges," *J. Phys. B At. Mol. Opt. Phys.*, vol. 49, no. 20, p. 202001, Oct. 2016, doi: 10.1088/0953-4075/49/20/202001.

[15] C. Monroe and J. Kim, "Scaling the Ion Trap Quantum Processor," *Science*, vol. 339, no. 6124, pp. 1164–1169, Mar. 2013, doi: 10.1126/science.1231298.

[16] M. H. Devoret and R. J. Schoelkopf, "Superconducting Circuits for Quantum Information: An Outlook," *Science*, vol. 339, no. 6124, pp. 1169–1174, Mar. 2013, doi: 10.1126/science.1231930.

[17] D. Awschalom *et al.*, "Development of Quantum Interconnects (QuICs) for Next-Generation Information Technologies," *PRX Quantum*, vol. 2, no. 1, p. 017002, Feb. 2021, doi: 10.1103/PRXQuantum.2.017002.

[18] S. Kako, C. Santori, K. Hoshino, S. Götzinger, Y. Yamamoto, and Y. Arakawa, "A gallium nitride single-photon source operating at 200 K," *Nat. Mater.*, vol. 5, no. 11, Art. no. 11, Nov. 2006, doi: 10.1038/nmat1763.

[19] S. Strauf, N. G. Stoltz, M. T. Rakher, L. A. Coldren, P. M. Petroff, and D. Bouwmeester, "High-frequency single-photon source with polarization control," *Nat. Photonics*, vol. 1, no. 12, Art. no. 12, Dec. 2007, doi: 10.1038/nphoton.2007.227.

[20] D. Najer *et al.*, "A gated quantum dot strongly coupled to an optical microcavity," *Nature*, vol. 575, no. 7784, Art. no. 7784, Nov. 2019, doi: 10.1038/s41586-019-1709-y.

[21] T. Gaebel, I. Popa, A. Gruber, M. Domhan, F. Jelezko, and J. Wrachtrup, "Stable single-photon source in the near infrared," *New J. Phys.*, vol. 6, pp. 98–98, Jul. 2004, doi: 10.1088/1367-2630/6/1/098.

[22] L. Li *et al.*, "Efficient Photon Collection from a Nitrogen Vacancy Center in a Circular Bullseye Grating," *Nano Lett.*, vol. 15, no. 3, pp. 1493–1497, Mar. 2015, doi: 10.1021/nl503451j.

[23] L.-T. Feng, G.-C. Guo, and X.-F. Ren, "Progress on Integrated Quantum Photonic Sources with Silicon," *Adv. Quantum Technol.*, vol. 3, no. 2, p. 1900058, 2020, doi: 10.1002/qute.201900058.

[24] S. Signorini and L. Pavesi, "On-chip heralded single photon sources," *AVS Quantum Sci.*, vol. 2, no. 4, p. 041701, Dec. 2020, doi: 10.1116/5.0018594.

[25] T. J. Steiner *et al.*, "Ultrabright Entangled-Photon-Pair Generation from an $\mathrm{Al}\mathrm{Ga}\mathrm{As}$-On-Insulator Microring Resonator," *PRX Quantum*, vol. 2, no. 1, p. 010337, Mar. 2021, doi: 10.1103/PRXQuantum.2.010337.

[26] E. Meyer-Scott, C. Silberhorn, and A. Migdall, "Single-photon sources: Approaching the ideal through multiplexing," *Rev. Sci. Instrum.*, vol. 91, no. 4, p. 041101, Apr. 2020, doi: 10.1063/5.0003320.

[27] A. L. Migdall, D. Branning, and S. Castelletto, "Tailoring single-photon and multiphoton probabilities of a single-photon on-demand source," *Phys. Rev. A*, vol. 66, no. 5, p. 053805, Nov. 2002, doi: 10.1103/PhysRevA.66.053805.

[28] J. Nunn *et al.*, "Enhancing Multiphoton Rates with Quantum Memories," *Phys. Rev. Lett.*, vol. 110, no. 13, p. 133601, Mar. 2013, doi: 10.1103/PhysRevLett.110.133601.

[29] R. J. A. Francis-Jones, R. A. Hoggarth, and P. J. Mosley, "All-fiber multiplexed source of high-purity single photons," *Optica*, vol. 3, no. 11, pp. 1270–1273, Nov. 2016, doi: 10.1364/OPTICA.3.001270.

[30] F. Kaneda and P. G. Kwiat, "High-efficiency single-photon generation via large-scale active time multiplexing," *Sci. Adv.*, vol. 5, no. 10, p. eaaw8586, Oct. 2019, doi: 10.1126/sciadv.aaw8586.

[31] L. Zhai *et al.*, "Quantum interference of identical photons from remote GaAs quantum dots," *Nat. Nanotechnol.*, pp. 1–5, May 2022, doi: 10.1038/s41565-022-01131-2.

[32] N. Tomm *et al.*, "A bright and fast source of coherent single photons," *Nat. Nanotechnol.*, vol. 16, no. 4, Art. no. 4, Apr. 2021, doi: 10.1038/s41565-020-00831-x.

[33] D. Llewellyn *et al.*, "Chip-to-chip quantum teleportation and multi-photon entanglement in silicon," *Nat. Phys.*, vol. 16, no. 2, Art. no. 2, Feb. 2020, doi: 10.1038/s41567-019-0727-x.

[34] A. Christ, A. Fedrizzi, H. Hübel, T. Jennewein, and C. Silberhorn, "Chapter 11 - Parametric Down-Conversion," in *Experimental Methods in the Physical Sciences*, vol. 45, A. Migdall, S. V. Polyakov, J. Fan, and J. C. Bienfang, Eds. Academic Press, 2013, pp. 351–410. doi: 10.1016/B978-0-12-387695-9.00011-1.

[35] A. McMillan, Y.-P. Huang, B. Bell, A. Clark, P. Kumar, and J. Rarity, "Chapter 12 - Four-Wave Mixing in Single-Mode Optical Fibers," in *Experimental Methods in the Physical Sciences*, vol. 45, A. Migdall, S. V. Polyakov, J. Fan, and J. C. Bienfang, Eds. Academic Press, 2013, pp. 411–465. doi: 10.1016/B978-0-12-387695-9.00012-3.

[36] M. Borghi and M. Borghi, "Phase-resolved joint spectra tomography of a ring resonator photon pair source using a silicon photonic chip," *Opt. Express*, vol. 28, no. 5, pp. 7442–7462, Mar. 2020, doi: 10.1364/OE.386139.

[37] C. Reimer *et al.*, "Generation of multiphoton entangled quantum states by means of integrated frequency combs," *Science*, vol. 351, no. 6278, pp. 1176–1180, Mar. 2016, doi: 10.1126/science.aad8532.

[38] S. Francesconi *et al.*, "Engineering two-photon wavefunction and exchange statistics in a semiconductor chip," *Optica*, vol. 7, no. 4, pp. 316–322, Apr. 2020, doi: 10.1364/OPTICA.379477.

[39] G. P. Agrawal, "Chapter 10 - PARAMETRIC PROCESSES," in *Nonlinear Fiber Optics (Second Edition)*, G. P. Agrawal, Ed. Boston: Academic Press, 1995, pp. 404–470. doi: 10.1016/B978-0-12-045142-5.50016-7.

[40] Q. Lin, O. J. Painter, and G. P. Agrawal, "Nonlinear optical phenomena in silicon waveguides: Modeling and applications," *Opt. Express*, vol. 15, no. 25, pp. 16604–16644, Dec. 2007, doi: 10.1364/OE.15.016604.

[41] R. W. Boyd, *Nonlinear Optics*. Elsevier, 2008.

[42] M. Dinu, "Dispersion of phonon-assisted nonresonant third-order nonlinearities," *IEEE J. Quantum Electron.*, vol. 39, no. 11, pp. 1498–1503, Nov. 2003, doi: 10.1109/JQE.2003.818277.

[43] M. Dinu, F. Quochi, and H. Garcia, "Third-order nonlinearities in silicon at telecom wavelengths," *Appl. Phys. Lett.*, vol. 82, no. 18, pp. 2954–2956, May 2003, doi: 10.1063/1.1571665.

[44] C. Koos, L. Jacome, C. Poulton, J. Leuthold, and W. Freude, "Nonlinear silicon-on-insulator waveguides for all-optical signal processing," *Opt. Express*, vol. 15, no. 10, pp. 5976–5990, May 2007, doi: 10.1364/OE.15.005976.

[45] D. T. H. Tan, K. Ikeda, P. C. Sun, and Y. Fainman, "Group velocity dispersion and self phase modulation in silicon nitride waveguides," *Appl. Phys. Lett.*, vol. 96, no. 6, p. 061101, Feb. 2010, doi: 10.1063/1.3299008.

[46] J. Chen, X. Li, and P. Kumar, "Two-photon-state generation via four-wave mixing in optical fibers," *Phys. Rev. A*, vol. 72, no. 3, p. 033801, Sep. 2005, doi: 10.1103/PhysRevA.72.033801.

[47] R. Soref and B. Bennett, "Electrooptical effects in silicon," *IEEE J. Quantum Electron.*, vol. 23, no. 1, pp. 123–129, Jan. 1987, doi: 10.1109/JQE.1987.1073206.

[48] R. F. Aguinaldo, "Silicon Photonics with Applications to Data Center Networks," Ph.D., University of California, San Diego, United States -- California. Accessed: Aug. 22, 2022. [Online]. Available: https://www.proquest.com/docview/1562946492/abstract/36A813C8F0DA4F29PQ/1

[49] P. E. Barclay, K. Srinivasan, and O. Painter, "Nonlinear response of silicon photonic crystal microresonators excited via an integrated waveguide and fiber taper," *Opt. Express*, vol. 13, no. 3, pp. 801–820, Feb. 2005, doi: 10.1364/OPEX.13.000801.

[50] T. J. Johnson, M. Borselli, and O. Painter, "Self-induced optical modulation of the transmission through a high-Q silicon microdisk resonator," *Opt. Express*, vol. 14, no. 2, pp. 817–831, Jan. 2006, doi: 10.1364/OPEX.14.000817.

[51] Q. Xu, B. Schmidt, S. Pradhan, and M. Lipson, "Micrometre-scale silicon electro-optic modulator," *Nature*, vol. 435, no. 7040, Art. no. 7040, May 2005, doi: 10.1038/nature03569.

[52] G. Li *et al.*, "Ring Resonator Modulators in Silicon for Interchip Photonic Links," *IEEE J. Sel. Top. Quantum Electron.*, vol. 19, no. 6, pp. 95–113, Nov. 2013, doi: 10.1109/JSTQE.2013.2278885.

[53] E. Timurdogan, C. M. Sorace-Agaskar, J. Sun, E. Shah Hosseini, A. Biberman, and M. R. Watts, "An ultralow power athermal silicon modulator," *Nat. Commun.*, vol. 5, no. 1, Art. no. 1, Jun. 2014, doi: 10.1038/ncomms5008.

[54] A. Jain *et al.*, "A High Spur-Free Dynamic Range Silicon DC Kerr Ring Modulator for RF Applications," *J. Light. Technol.*, vol. 37, no. 13, pp. 3261–3272, Jul. 2019, doi: 10.1109/JLT.2019.2913638.

[55] H. Yu *et al.*, "Trade-off between optical modulation amplitude and modulation bandwidth of silicon micro-ring modulators," *Opt. Express*, vol. 22, no. 12, pp. 15178–15189, Jun. 2014, doi: 10.1364/OE.22.015178.

[56] D. Liang and J. E. Bowers, "Recent Progress in Heterogeneous III-V-on-Silicon Photonic Integration," *Light Adv. Manuf.*, vol. 2, no. 1, pp. 59–83, Mar. 2021, doi: 10.37188/lam.2021.005.

[57] R. Kumar *et al.*, "A multi-wavelength III-V/Si hybrid DFB laser with even wavelength spacing and uniform output power," in *2021 IEEE 17th International Conference on Group IV Photonics (GFP)*, Dec. 2021, pp. 1–2. doi: 10.1109/GFP51802.2021.9673975.

[58] D. K. Schroder, R. N. Thomas, and J. C. Swartz, "Free carrier absorption in silicon," *IEEE Trans. Electron Devices*, vol. 25, no. 2, pp. 254–261, Feb. 1978, doi: 10.1109/T-ED.1978.19066.

[59] D. M. Gill, C. Xiong, J. C. Rosenberg, P. Pepeljugoski, J. S. Orcutt, and W. M. J. Green, "Modulator figure of merit for short reach data links," *Opt. Express*, vol. 25, no. 20, pp. 24326–24339, Oct. 2017, doi: 10.1364/OE.25.024326.

[60] K. Frojdh, "1300 and 1550 nm single mode serial PMDs," p. 16, 2000.

[61] "IEEE Standard for Information technology– Local and metropolitan area networks– Part 3: CSMA/CD Access Method and Physical Layer Specifications Amendment: Media Access Control Parameters, Physical Layers, and Management Parameters for Subscriber Access Networks," *IEEE Std 8023ah-2004*, pp. 1–640, Sep. 2004, doi: 10.1109/IEEESTD.2004.94617.

[62] X. Guan, W. Shi, and L. A. Rusch, "Ultra-Dense Wavelength-Division Multiplexing With Microring Modulator," *J. Light. Technol.*, vol. 39, no. 13, pp. 4300–4306, Jul. 2021, doi: 10.1109/JLT.2021.3070515.

[63] C. Xiong, D. M. Gill, J. E. Proesel, J. S. Orcutt, W. Haensch, and W. M. J. Green, "Monolithic 56 Gb/s silicon photonic pulse-amplitude modulation transmitter," *Optica*, vol. 3, no. 10, pp. 1060–1065, Oct. 2016, doi: 10.1364/OPTICA.3.001060.

[64] W. M. Mellette *et al.*, "Optical networking within the Lightwave Energy-Efficient Datacenter project [Invited]," *J. Opt. Commun. Netw.*, vol. 12, no. 12, pp. 378–389, Dec. 2020, doi: 10.1364/JOCN.401903.

[65] M. R. Watts, W. A. Zortman, D. C. Trotter, R. W. Young, and A. L. Lentine, "Vertical junction silicon microdisk modulators and switches," *Opt. Express*, vol. 19, no. 22, pp. 21989–22003, Oct. 2011, doi: 10.1364/OE.19.021989.

[66] A. L. Lentine *et al.*, "Silicon photonics platform for national security applications," in *2015 IEEE Aerospace Conference*, Mar. 2015, pp. 1–9. doi: 10.1109/AERO.2015.7119249.

[67] J. C. Rosenberg *et al.*, "A 25 Gbps silicon microring modulator based on an interleaved junction," *Opt. Express*, vol. 20, no. 24, pp. 26411–26423, Nov. 2012, doi: 10.1364/OE.20.026411.

[68] D. Dimitropoulos, R. Jhaveri, R. Claps, J. C. S. Woo, and B. Jalali, "Lifetime of photogenerated carriers in silicon-on-insulator rib waveguides," *Appl. Phys. Lett.*, vol. 86, no. 7, p. 071115, Feb. 2005, doi: 10.1063/1.1866635.

[69] X. Wang *et al.*, "Wide-range and fast thermally-tunable silicon photonic microring resonators using the junction field effect," *Opt. Express*, vol. 24, no. 20, pp. 23081–23093, Oct. 2016, doi: 10.1364/OE.24.023081.

[70] C. Sun *et al.*, "A 45 nm CMOS-SOI Monolithic Photonics Platform With Bit-Statistics-Based Resonant Microring Thermal Tuning," *IEEE J. Solid-State Circuits*, vol. 51, no. 4, pp. 893–907, Apr. 2016, doi: 10.1109/JSSC.2016.2519390.

[71] A. Yariv, "Universal relations for coupling of optical power between microresonators and dielectric waveguides," *Electron. Lett.*, vol. 36, no. 4, pp. 321–322, Feb. 2000.

[72] B. E. Little, S. T. Chu, H. A. Haus, J. Foresi, and J.-P. Laine, "Microring resonator channel dropping filters," *J. Light. Technol.*, vol. 15, no. 6, pp. 998–1005, Jun. 1997, doi: 10.1109/50.588673.

[73] D. Zheng, C. Qiu, H. Zhang, X. Jiang, and Y. Su, "Demonstration of a Push-Pull Silicon Dual-Ring Modulator With Enhanced Optical Modulation Amplitude," *J. Light. Technol.*, vol. 38, no. 14, pp. 3694–3700, Jul. 2020, doi: 10.1109/JLT.2020.2978149.

[74] H. Li *et al.*, "A 112 Gb/s PAM4 Silicon Photonics Transmitter With Microring Modulator and CMOS Driver," *J. Light. Technol.*, vol. 38, no. 1, pp. 131–138, Jan. 2020, doi: 10.1109/JLT.2019.2938731.

[75] E. Timurdogan, "Wafer-scale integrated active silicon photonics for manipulation and conversion of light," Thesis, Massachusetts Institute of Technology, 2016. Accessed: Aug. 23, 2022. [Online]. Available: https://dspace.mit.edu/handle/1721.1/107355

[76] X. Xiao *et al.*, "25 Gbit/s silicon microring modulator based on misalignment-tolerant interleaved PN junctions," *Opt. Express*, vol. 20, no. 3, pp. 2507–2515, Jan. 2012, doi: 10.1364/OE.20.002507.

[77] T. Gu, Y.-K. Chen, C. W. Wong, and P. Dong, "Cascaded uncoupled dual-ring modulator," *Opt. Lett.*, vol. 39, no. 16, pp. 4974–4977, Aug. 2014, doi: 10.1364/OL.39.004974.

[78] H. Yu *et al.*, "Silicon dual-ring modulator driven by differential signal," *Opt. Lett.*, vol. 39, no. 22, pp. 6379–6382, Nov. 2014, doi: 10.1364/OL.39.006379.

[79] N. J. D. Martinez *et al.*, "Low Power Thermal Tuning in Resonant Vertical Junction Silicon Modulators Through Substrate Removal," *IEEE Photonics J.*, vol. 10, no. 3, pp. 1–12, Jun. 2018, doi: 10.1109/JPHOT.2018.2824026.

[80] G. Porter *et al.*, "Integrating microsecond circuit switching into the data center," in *Proceedings of the ACM SIGCOMM 2013 conference on SIGCOMM*, New York, NY, USA, Aug. 2013, pp. 447–458. doi: 10.1145/2486001.2486007.

[81] J. Niehusmann, A. Vörckel, P. H. Bolivar, T. Wahlbrink, W. Henschel, and H. Kurz, "Ultrahigh-quality-factor silicon-on-insulator microring resonator," *Opt. Lett.*, vol. 29, no. 24, pp. 2861–2863, Dec. 2004, doi: 10.1364/OL.29.002861.

[82] H. Chen, X. Luo, and A. W. Poon, "Cavity-enhanced photocurrent generation by 1.55 μm wavelengths linear absorption in a p-i-n diode embedded silicon microring resonator," *Appl. Phys. Lett.*, vol. 95, no. 17, p. 171111, Oct. 2009, doi: 10.1063/1.3257384.

[83] W. Bogaerts *et al.*, "Silicon-on-Insulator Spectral Filters Fabricated With CMOS Technology," *IEEE J. Sel. Top. Quantum Electron.*, vol. 16, no. 1, pp. 33–44, Jan. 2010, doi: 10.1109/JSTQE.2009.2039680.

[84] P. Dong *et al.*, "Low power and compact reconfigurable multiplexing devices based on silicon microring resonators," *Opt. Express*, vol. 18, no. 10, pp. 9852–9858, May 2010, doi: 10.1364/OE.18.009852.

[85] J. R. Ong, R. Kumar, and S. Mookherjea, "Ultra-High-Contrast and Tunable-Bandwidth Filter Using Cascaded High-Order Silicon Microring Filters," *IEEE Photonics Technol. Lett.*, vol. 25, no. 16, pp. 1543–1546, Aug. 2013, doi: 10.1109/LPT.2013.2267539.

[86] A. Canciamilla *et al.*, "Photo-induced trimming of chalcogenide-assisted silicon waveguides," *Opt. Express*, vol. 20, no. 14, pp. 15807–15817, Jul. 2012, doi: 10.1364/OE.20.015807.

[87] Y. Shen, I. B. Divliansky, D. N. Basov, and S. Mookherjea, "Electric-field-driven nano-oxidation trimming of silicon microrings and interferometers," *Opt. Lett.*, vol. 36, no. 14, pp. 2668–2670, Jul. 2011, doi: 10.1364/OL.36.002668.

[88] J. Teng *et al.*, "Athermal Silicon-on-insulator ring resonators by overlaying a polymer cladding on narrowed waveguides," *Opt. Express*, vol. 17, no. 17, pp. 14627–14633, Aug. 2009, doi: 10.1364/OE.17.014627.

[89] R. L. Espinola, M. C. Tsai, J. T. Yardley, and R. M. Osgood, "Fast and low-power thermooptic switch on thin silicon-on-insulator," *IEEE Photonics Technol. Lett.*, vol. 15, no. 10, pp. 1366–1368, Oct. 2003, doi: 10.1109/LPT.2003.818246.

[90] D. H. Geuzebroek, E. J. Klein, H. Kelderman, and A. Driessen, "Wavelength Tuning and Switching of a Thermo-Optic Microring Resonator," p. 4.

[91] M. S. Nawrocka, T. Liu, X. Wang, and R. R. Panepucci, "Tunable silicon microring resonator with wide free spectral range," *Appl. Phys. Lett.*, vol. 89, no. 7, p. 071110, Aug. 2006, doi: 10.1063/1.2337162.

[92] L. Chrostowski and M. Hochberg, *Silicon Photonics Design: From Devices to Systems*. Cambridge: Cambridge University Press, 2015. doi: 10.1017/CBO9781316084168.

[93] M. R. Watts and G. N. Nielson, "Optical waveguide device with an adiabatically-varying width," US7941014B1, May 10, 2011 Accessed: Aug. 24, 2022. [Online]. Available: https://patents.google.com/patent/US7941014B1/en

[94] C. T. DeRose *et al.*, "Low Power and Broadband 2 × 2 Silicon Thermo-Optic Switch," in *Optical Fiber Communication Conference/National Fiber Optic Engineers Conference 2011 (2011), paper OThM3*, Mar. 2011, p. OThM3. doi: 10.1364/OFC.2011.OThM3.

[95] M. R. Watts, W. A. Zortman, D. C. Trotter, G. N. Nielson, D. L. Luck, and R. W. Young, "Adiabatic Resonant Microrings (ARMs) with directly integrated thermal microphotonics," in *2009 Conference on Lasers and Electro-Optics and 2009 Conference on Quantum*

electronics and Laser Science Conference, Jun. 2009, pp. 1–2. doi: 10.1364/CLEO.2009.CPDB10.

[96]   R. Aguinaldo *et al.*, "Silicon photonic integrated components for add, drop, and VOA in a 4-channel data-center network," in *2014 IEEE Photonics Conference*, Oct. 2014, pp. 1–2. doi: 10.1109/IPCon.2014.7092976.

[97]   S. K. Wiedmann, "Monolithic circuits with pinch resistors," U.S. 3,693,057, Sep. 19, 1972

[98]   N. H. E. Weste and D. M. Harris, *CMOS VLSI Design: A Circuits and Systems Perspective*. Addison Wesley, 2011.

[99]   M. Harjanne, M. Kapulainen, T. Aalto, and P. Heimala, "Sub-µs switching time in silicon-on-insulator Mach-Zehnder thermooptic switch," *IEEE Photonics Technol. Lett.*, vol. 16, no. 9, pp. 2039–2041, Sep. 2004, doi: 10.1109/LPT.2004.833896.

[100]   E. Timurdogan, C. M. Sorace-Agaskar, E. S. Hosseini, and M. R. Watts, "An Interior-Ridge Silicon Microring Modulator," *J. Light. Technol.*, vol. 31, no. 24, pp. 3907–3914, Dec. 2013, doi: 10.1109/JLT.2013.2278761.

[101]   P. Dong *et al.*, "Thermally tunable silicon racetrack resonators with ultralow tuning power," *Opt. Express*, vol. 18, no. 19, pp. 20298–20304, Sep. 2010, doi: 10.1364/OE.18.020298.

[102]   Q. Fang *et al.*, "Ultralow Power Silicon Photonics Thermo-Optic Switch With Suspended Phase Arms," *IEEE Photonics Technol. Lett.*, vol. 23, no. 8, pp. 525–527, Apr. 2011, doi: 10.1109/LPT.2011.2114336.

[103]   R. Aguinaldo, Yiran Shen, and S. Mookherjea, "Large Dispersion of Silicon Directional Couplers Obtained via Wideband Microring Parametric Characterization," *IEEE Photonics Technol. Lett.*, vol. 24, no. 14, pp. 1242–1244, Jul. 2012, doi: 10.1109/LPT.2012.2198639.

[104]   F. Xia, M. Rooks, L. Sekaric, and Y. Vlasov, "Ultra-compact high order ring resonator filters using submicron silicon photonic wires for on-chip optical interconnects," *Opt. Express*, vol. 15, no. 19, pp. 11934–11941, Sep. 2007, doi: 10.1364/OE.15.011934.

[105]   J. R. Ong, R. Kumar, and S. Mookherjea, "Ultra-High-Contrast and Tunable-Bandwidth Filter Using Cascaded High-Order Silicon Microring Filters," *IEEE Photonics Technol. Lett.*, vol. 25, no. 16, pp. 1543–1546, Aug. 2013, doi: 10.1109/LPT.2013.2267539.

[106]   R. Ahmed, A. A. Rifat, A. K. Yetisen, M. S. Salem, S.-H. Yun, and H. Butt, "Optical microring resonator based corrosion sensing," *RSC Adv.*, vol. 6, no. 61, pp. 56127–56133, Jun. 2016, doi: 10.1039/C6RA11538A.

[107]   J. Li *et al.*, "Improving the Spatial Resolution of an OFDR Based on Recirculating Frequency Shifter," *IEEE Photonics J.*, vol. 7, no. 5, pp. 1–10, Oct. 2015, doi: 10.1109/JPHOT.2015.2484283.

[108]   H. Hemmati, A. Biswas, and I. B. Djordjevic, "Deep-Space Optical Communications: Future Perspectives and Applications," *Proc. IEEE*, vol. 99, no. 11, pp. 2020–2039, Nov. 2011, doi: 10.1109/JPROC.2011.2160609.

[109]   Z. Wang *et al.*, "A III-V-on-Si ultra-dense comb laser," *Light Sci. Appl.*, vol. 6, no. 5, Art. no. 5, May 2017, doi: 10.1038/lsa.2016.260.

[110]   M. A. Foster, J. S. Levy, O. Kuzucu, K. Saha, M. Lipson, and A. L. Gaeta, "Silicon-based monolithic optical frequency comb source," *Opt. Express*, vol. 19, no. 15, pp. 14233–14239, Jul. 2011, doi: 10.1364/OE.19.014233.

[111]   T. Yamamoto, K. Hitomi, W. Kobayashi, and H. Yasaka, "Optical Frequency Comb Block Generation by Using Semiconductor Mach–Zehnder Modulator," *IEEE Photonics Technol. Lett.*, vol. 25, no. 1, pp. 40–42, Jan. 2013, doi: 10.1109/LPT.2012.2227696.

[112] S. Chandrasekhar, X. Liu, B. Zhu, and D. W. Peckham, "Transmission of a 1.2-Tb/s 24-carrier no-guard-interval coherent OFDM superchannel over 7200-km of ultra-large-area fiber," in *2009 35th European Conference on Optical Communication*, Sep. 2009, vol. 2009-Supplement, pp. 1–2.

[113] J. Lin, H. Sepehrian, L. A. Rusch, and W. Shi, "Flexible on-chip frequency comb generation using a SOI dual-drive MZM," in *2017 IEEE Optical Interconnects Conference (OI)*, Jun. 2017, pp. 27–28. doi: 10.1109/OIC.2017.7965514.

[114] J. Lin *et al.*, "High-quality frequency-locked optical frequency comb source for terabits optical communication system," *Opt. Eng.*, vol. 53, no. 12, p. 122608, Sep. 2014, doi: 10.1117/1.OE.53.12.122608.

[115] N. Dupuis *et al.*, "InP-based comb generator for optical OFDM," in *Optical Fiber Communication Conference/National Fiber Optic Engineers Conference 2011 (2011), paper PDPC8*, Mar. 2011, p. PDPC8. doi: 10.1364/OFC.2011.PDPC8.

[116] L. Zhang, Y. Song, S. Zou, Y. Li, J. Ye, and R. Lin, "Performance analysis of flat optical comb generation based on recirculating frequency shifter," in *International Conference on Applications of Optics and Photonics*, Jul. 2011, vol. 8001, pp. 364–371. doi: 10.1117/12.892157.

[117] J. Li, X. Li, X. Zhang, F. Tian, and L. Xi, "Analysis of the stability and optimizing operation of the single-side-band modulator based on re-circulating frequency shifter used for the T-bit/s optical communication transmission," *Opt. Express*, vol. 18, no. 17, pp. 17597–17609, Aug. 2010, doi: 10.1364/OE.18.017597.

[118] J. Lin, L. Xi, J. Li, X. Zhang, X. Zhang, and S. A. Niazi, "Low noise optical multi-carrier generation using optical-FIR filter for ASE noise suppression in re-circulating frequency shifter loop," *Opt. Express*, vol. 22, no. 7, pp. 7852–7864, Apr. 2014, doi: 10.1364/OE.22.007852.

[119] W. Sohler *et al.*, "Integrated Optical Devices in Lithium Niobate," *Opt. Photonics News*, vol. 19, no. 1, pp. 24–31, Jan. 2008, doi: 10.1364/OPN.19.1.000024.

[120] L. Chen, Q. Xu, M. G. Wood, and R. M. Reano, "Hybrid silicon and lithium niobate electro-optical ring modulator," *Optica*, vol. 1, no. 2, pp. 112–118, Aug. 2014, doi: 10.1364/OPTICA.1.000112.

[121] A. Rao *et al.*, "High-performance and linear thin-film lithium niobate Mach–Zehnder modulators on silicon up to 50 GHz," *Opt. Lett.*, vol. 41, no. 24, pp. 5700–5703, Dec. 2016, doi: 10.1364/OL.41.005700.

[122] A. Boes, B. Corcoran, L. Chang, J. Bowers, and A. Mitchell, "Status and Potential of Lithium Niobate on Insulator (LNOI) for Photonic Integrated Circuits," *Laser Photonics Rev.*, vol. 12, no. 4, p. 1700256, 2018, doi: 10.1002/lpor.201700256.

[123] C. Wang *et al.*, "Integrated lithium niobate electro-optic modulators operating at CMOS-compatible voltages," *Nature*, vol. 562, no. 7725, Art. no. 7725, Oct. 2018, doi: 10.1038/s41586-018-0551-y.

[124] D. Zhu *et al.*, "Integrated photonics on thin-film lithium niobate," *Adv. Opt. Photonics*, vol. 13, no. 2, pp. 242–352, Jun. 2021, doi: 10.1364/AOP.411024.

[125] P. O. Weigel *et al.*, "Lightwave Circuits in Lithium Niobate through Hybrid Waveguides with Silicon Photonics," *Sci. Rep.*, vol. 6, no. 1, Art. no. 1, Mar. 2016, doi: 10.1038/srep22301.

[126] X. Wang, P. O. Weigel, J. Zhao, M. Ruesing, and S. Mookherjea, "Achieving beyond-100-GHz large-signal modulation bandwidth in hybrid silicon photonics Mach Zehnder

modulators using thin film lithium niobate," *APL Photonics*, vol. 4, no. 9, p. 096101, Sep. 2019, doi: 10.1063/1.5115243.

[127] A. J. Mercante, P. Yao, S. Shi, G. Schneider, J. Murakowski, and D. W. Prather, "110 GHz CMOS compatible thin film LiNbO3 modulator on silicon," *Opt. Express*, vol. 24, no. 14, pp. 15590–15595, Jul. 2016, doi: 10.1364/OE.24.015590.

[128] M. He *et al.*, "High-performance hybrid silicon and lithium niobate Mach–Zehnder modulators for 100 Gbit s−1 and beyond," *Nat. Photonics*, vol. 13, no. 5, Art. no. 5, May 2019, doi: 10.1038/s41566-019-0378-6.

[129] P. Rabiei, J. Ma, S. Khan, J. Chiles, and S. Fathpour, "Heterogeneous lithium niobate photonics on silicon substrates," *Opt. Express*, vol. 21, no. 21, pp. 25573–25581, Oct. 2013, doi: 10.1364/OE.21.025573.

[130] L. Cao, A. Aboketaf, Z. Wang, and S. Preble, "Hybrid amorphous silicon (a-Si:H)– LiNbO3 electro-optic modulator," *Opt. Commun.*, vol. 330, pp. 40–44, Nov. 2014, doi: 10.1016/j.optcom.2014.05.021.

[131] N. Boynton *et al.*, "A heterogeneously integrated silicon photonic/lithium niobate travelling wave electro-optic modulator," *Opt. Express*, vol. 28, no. 2, pp. 1868–1884, Jan. 2020, doi: 10.1364/OE.28.001868.

[132] P. O. Weigel, F. Valdez, J. Zhao, H. Li, and S. Mookherjea, "Design of high-bandwidth, low-voltage and low-loss hybrid lithium niobate electro-optic modulators," *J. Phys. Photonics*, vol. 3, no. 1, p. 012001, Nov. 2020, doi: 10.1088/2515-7647/abc17e.

[133] M. Savanier, R. Kumar, and S. Mookherjea, "Photon pair generation from compact silicon microring resonators using microwatt-level pump powers," *Opt. Express*, vol. 24, no. 4, pp. 3313–3328, Feb. 2016, doi: 10.1364/OE.24.003313.

[134] C. Xiong *et al.*, "Quantum-correlated photon pair generation in chalcogenide As_2S_3 waveguides," *Opt. Express*, vol. 18, no. 15, pp. 16206–16216, Jul. 2010, doi: 10.1364/OE.18.016206.

[135] C. Xiong *et al.*, "Generation of correlated photon pairs in a chalcogenide As2S3 waveguide," *Appl. Phys. Lett.*, vol. 98, no. 5, p. 051101, Jan. 2011, doi: 10.1063/1.3549744.

[136] J. Schneeloch *et al.*, "Introduction to the absolute brightness and number statistics in spontaneous parametric down-conversion," *J. Opt.*, vol. 21, no. 4, p. 043501, Feb. 2019, doi: 10.1088/2040-8986/ab05a8.

[137] R. Loudon, "The Quantum Theory of Light," *Am. J. Phys.*, vol. 42, no. 11, pp. 1041– 1042, Nov. 1974, doi: 10.1119/1.1987930.

[138] R. Loudon and L. Hunter, "The Quantum Theory of Light, Second Edition," *Am. J. Phys.*, vol. 54, no. 3, pp. 285–286, Mar. 1986, doi: 10.1119/1.14652.

[139] G. A. Steudle *et al.*, "Measuring the quantum nature of light with a single source and a single detector," *Phys. Rev. A*, vol. 86, no. 5, p. 053814, Nov. 2012, doi: 10.1103/PhysRevA.86.053814.

[140] S. Liu, X. Lin, F. Liu, H. Lei, W. Fang, and C. Jin, "Observation of photon antibunching with only one standard single-photon detector," *Rev. Sci. Instrum.*, vol. 92, no. 1, p. 013105, Jan. 2021, doi: 10.1063/5.0038035.

[141] C. Ma, X. Wang, V. Anant, A. D. Beyer, M. D. Shaw, and S. Mookherjea, "Silicon photonic entangled photon-pair and heralded single photon generation with CAR > 12,000 and g^(2)(0) < 0006," *Opt. Express*, vol. 25, no. 26, p. 32995, Dec. 2017, doi: 10.1364/OE.25.032995.

[142] J. D. Franson, "Bell inequality for position and time," *Phys. Rev. Lett.*, vol. 62, no. 19, pp. 2205–2208, May 1989, doi: 10.1103/PhysRevLett.62.2205.

[143] Z. J. Ou, *Quantum Optics for Experimentalists*. WORLD SCIENTIFIC, 2017. doi: 10.1142/10453.

[144] C. Gerry and P. Knight, *Introductory Quantum Optics*. Cambridge: Cambridge University Press, 2004. doi: 10.1017/CBO9780511791239.

[145] R. Kumar, "Photon Pairs from a Silicon Photonic Chip," UC San Diego, 2016. Accessed: Aug. 21, 2022. [Online]. Available: https://escholarship.org/uc/item/8rf1660h

[146] J. F. Clauser and A. Shimony, "Bell's theorem. Experimental tests and implications," *Rep. Prog. Phys.*, vol. 41, no. 12, pp. 1881–1927, Dec. 1978, doi: 10.1088/0034-4885/41/12/002.

[147] J. F. Clauser, M. A. Horne, A. Shimony, and R. A. Holt, "Proposed Experiment to Test Local Hidden-Variable Theories," *Phys. Rev. Lett.*, vol. 23, no. 15, pp. 880–884, Oct. 1969, doi: 10.1103/PhysRevLett.23.880.

[148] E. Dulkeith, F. Xia, L. Schares, W. M. J. Green, and Y. A. Vlasov, "Group index and group velocity dispersion in silicon-on-insulator photonic wires," *Opt Express*, vol. 14, no. 9, pp. 3853–3863, May 2006, doi: 10.1364/OE.14.003853.

[149] H. P. Bazargani, J. Flueckiger, L. Chrostowski, and J. Azaña, "Microring resonator design with improved quality factors using quarter Bezier curves," in *CLEO: 2015*, San Jose, California, 2015, p. JTu5A.58. doi: 10.1364/CLEO_AT.2015.JTu5A.58.

[150] T. Y. L. Ang, J. R. Ong, S. T. Lim, C. E. Png, X. Guo, and H. Wang, "Versatile bezier bends for silicon photonics," in *2017 conference on lasers and electro-optics pacific rim*, 2017, p. s1869. [Online]. Available: http://opg.optica.org/abstract.cfm?URI=CLEOPR-2017-s1869

[151] T. Barwicz and H. A. Haus, "Three-dimensional analysis of scattering losses due to sidewall roughness in microphotonic waveguides," *J. Light. Technol.*, vol. 23, no. 9, pp. 2719–2732, Sep. 2005, doi: 10.1109/JLT.2005.850816.

[152] C. Ma, X. Wang, and S. Mookherjea, "Progress towards a widely usable integrated silicon photonic photon-pair source," *OSA Contin.*, vol. 3, no. 6, p. 1398, Jun. 2020, doi: 10.1364/OSAC.392495.

[153] C. Ma, X. Wang, V. Anant, A. D. Beyer, M. D. Shaw, and S. Mookherjea, "Silicon photonic entangled photon-pair and heralded single photon generation with CAR > 12,000 and $g^{(2)}(0)$ < 0.006," *Opt. Express*, vol. 25, no. 26, pp. 32995–33006, Dec. 2017, doi: 10.1364/OE.25.032995.

[154] X. Lu, S. Rogers, T. Gerrits, W. C. Jiang, S. W. Nam, and Q. Lin, "Heralding single photons from a high-Q silicon microdisk," *Optica*, vol. 3, no. 12, pp. 1331–1338, Dec. 2016, doi: 10.1364/OPTICA.3.001331.

[155] Y. Liu *et al.*, "High-spectral-purity photon generation from a dual-interferometer-coupled silicon microring," *Opt. Lett.*, vol. 45, no. 1, pp. 73–76, Jan. 2020, doi: 10.1364/OL.45.000073.

[156] J. R. Ong, R. Kumar, and S. Mookherjea, "Silicon microring-based wavelength converter with integrated pump and signal suppression," *Opt. Lett.*, vol. 39, no. 15, p. 4439, Aug. 2014, doi: 10.1364/OL.39.004439.

[157] M. L. Cooper and S. Mookherjea, "Modeling of Multiband Transmission in Long Silicon Coupled-Resonator Optical Waveguides," *IEEE Photonics Technol. Lett.*, vol. 23, no. 13, pp. 872–874, Jul. 2011, doi: 10.1109/LPT.2011.2141657.

[158] S. Mookherjea and M. A. Schneider, "Avoiding bandwidth collapse in long chains of coupled optical microresonators," *Opt. Lett.*, vol. 36, no. 23, p. 4557, Dec. 2011, doi: 10.1364/OL.36.004557.

[159] H. Takagi, R. Maeda, N. Hosoda, and T. Suga, "Room-temperature bonding of lithium niobate and silicon wafers by argon-beam surface activation," *Appl. Phys. Lett.*, vol. 74, no. 16, pp. 2387–2389, Apr. 1999, doi: 10.1063/1.123860.

[160] M. M. R. Howlader, T. Suga, and M. J. Kim, "Room temperature bonding of silicon and lithium niobate," *Appl. Phys. Lett.*, vol. 89, no. 3, p. 031914, Jul. 2006, doi: 10.1063/1.2229262.

[161] R. Takigawa, E. Higurashi, T. Suga, S. Shinada, and T. Kawanishi, "Low-temperature bonding of a LiNbO3 waveguide chip to a Si substrate in ambient air for hybrid-integrated optical devices," in *Optomechatronic Micro/Nano Devices and Components II*, Oct. 2006, vol. 6376, pp. 16–22. doi: 10.1117/12.690741.

[162] P. O. Weigel and S. Mookherjea, "Reducing the thermal stress in a heterogeneous material stack for large-area hybrid optical silicon-lithium niobate waveguide micro-chips," *Opt. Mater.*, vol. 66, pp. 605–610, Apr. 2017, doi: 10.1016/j.optmat.2017.03.014.

[163] V. E. Stenger *et al.*, "Low Loss and Low Vpi Thin Film Lithium Niobate on Quartz Electro-optic Modulators," in *2017 European Conference on Optical Communication (ECOC)*, Sep. 2017, pp. 1–3. doi: 10.1109/ECOC.2017.8346144.

[164] C. Wang, M. Zhang, B. Stern, M. Lipson, and M. Lončar, "Nanophotonic lithium niobate electro-optic modulators," *Opt. Express*, vol. 26, no. 2, pp. 1547–1555, Jan. 2018, doi: 10.1364/OE.26.001547.

[165] G. Ulliac, V. Calero, A. Ndao, F. I. Baida, and M.-P. Bernal, "Argon plasma inductively coupled plasma reactive ion etching study for smooth sidewall thin film lithium niobate waveguide application," *Opt. Mater.*, vol. 53, pp. 1–5, Mar. 2016, doi: 10.1016/j.optmat.2015.12.040.

[166] M. Zhang *et al.*, "Ultra-High Bandwidth Integrated Lithium Niobate Modulators with Record-Low Vπ," in *2018 Optical Fiber Communications Conference and Exposition (OFC)*, Mar. 2018, pp. 1–3.

[167] I.-L. Gheorma, P. Savi, and R. M. Osgood, "Thin layer design of X-cut LiNbO3 modulators," *IEEE Photonics Technol. Lett.*, vol. 12, no. 12, pp. 1618–1620, Dec. 2000, doi: 10.1109/68.896326.

[168] G. Ghione, Ed., "Modulators," in *Semiconductor Devices for High-Speed Optoelectronics*, Cambridge: Cambridge University Press, 2009, pp. 356–439. doi: 10.1017/CBO9780511635595.007.

[169] D. M. Pozar, *Microwave Engineering*. John Wiley & Sons, 2011.

[170] G. Ghione, *Semiconductor Devices for High-Speed Optoelectronics*. Cambridge: Cambridge University Press, 2009. doi: 10.1017/CBO9780511635595.

[171] S. Ummethala *et al.*, "Hybrid electro-optic modulator combining silicon photonic slot waveguides with high-k radio-frequency slotlines," *Optica*, vol. 8, no. 4, pp. 511–519, Apr. 2021, doi: 10.1364/OPTICA.411161.

[172] Y. Ogiso *et al.*, "80-GHz Bandwidth and 1.5-V Vπ InP-Based IQ Modulator," *J. Light. Technol.*, vol. 38, no. 2, pp. 249–255, Jan. 2020.

[173] X. Qiang *et al.*, "Large-scale silicon quantum photonics implementing arbitrary two-qubit processing," *Nat. Photonics*, vol. 12, no. 9, Art. no. 9, Sep. 2018, doi: 10.1038/s41566-018-0236-y.

[174]   A. Blanco-Redondo, B. Bell, D. Oren, B. J. Eggleton, and M. Segev, "Topological protection of biphoton states," *Science*, vol. 362, no. 6414, pp. 568–571, Nov. 2018, doi: 10.1126/science.aau4296.

[175]   S. Mittal, E. A. Goldschmidt, and M. Hafezi, "A topological source of quantum light," *Nature*, vol. 561, no. 7724, Art. no. 7724, Sep. 2018, doi: 10.1038/s41586-018-0478-3.

[176]   A. W. Elshaari, W. Pernice, K. Srinivasan, O. Benson, and V. Zwiller, "Hybrid integrated quantum photonic circuits," *Nat. Photonics*, vol. 14, no. 5, Art. no. 5, May 2020, doi: 10.1038/s41566-020-0609-x.

[177]   B. Brecht, D. V. Reddy, C. Silberhorn, and M. G. Raymer, "Photon Temporal Modes: A Complete Framework for Quantum Information Science," *Phys. Rev. X*, vol. 5, no. 4, p. 041017, Oct. 2015, doi: 10.1103/PhysRevX.5.041017.

[178]   L. G. Helt, Z. Yang, M. Liscidini, and J. E. Sipe, "Spontaneous four-wave mixing in microring resonators," *Opt. Lett.*, vol. 35, no. 18, pp. 3006–3008, Sep. 2010, doi: 10.1364/OL.35.003006.

[179]   Z. Vernon *et al.*, "Truly unentangled photon pairs without spectral filtering," *Opt. Lett.*, vol. 42, no. 18, pp. 3638–3641, Sep. 2017, doi: 10.1364/OL.42.003638.

[180]   R. Grobe, K. Rzazewski, and J. H. Eberly, "Measure of electron-electron correlation in atomic physics," *J. Phys. B At. Mol. Opt. Phys.*, vol. 27, no. 16, pp. L503–L508, Aug. 1994, doi: 10.1088/0953-4075/27/16/001.

[181]   J. H. Eberly, "Schmidt analysis of pure-state entanglement," *Laser Phys.*, vol. 16, no. 6, pp. 921–926, Jun. 2006, doi: 10.1134/S1054660X06060041.

[182]   C. K. Law and J. H. Eberly, "Analysis and Interpretation of High Transverse Entanglement in Optical Parametric Down Conversion," *Phys. Rev. Lett.*, vol. 92, no. 12, p. 127903, Mar. 2004, doi: 10.1103/PhysRevLett.92.127903.

[183]   A. B. U'Ren *et al.*, "Generation of Pure-State Single-Photon Wavepackets by Conditional Preparation Based on Spontaneous Parametric Downconversion," *Laser Phys.*, vol. 15, no. 1, p. 16, 2005.

[184]   M. Liscidini and J. E. Sipe, "Stimulated Emission Tomography," *Phys. Rev. Lett.*, vol. 111, no. 19, p. 193602, Nov. 2013, doi: 10.1103/PhysRevLett.111.193602.

[185]   A. Eckstein *et al.*, "High-resolution spectral characterization of two photon states via classical measurements," *Laser Photonics Rev.*, vol. 8, no. 5, pp. L76–L80, 2014, doi: 10.1002/lpor.201400057.

[186]   B. Fang, O. Cohen, M. Liscidini, J. E. Sipe, and V. O. Lorenz, "Fast and highly resolved capture of the joint spectral density of photon pairs," *Optica*, vol. 1, no. 5, pp. 281–284, Nov. 2014, doi: 10.1364/OPTICA.1.000281.

[187]   M. A. Ciampini *et al.*, "Stimulated emission tomography: beyond polarization," *Opt. Lett.*, vol. 44, no. 1, pp. 41–44, Jan. 2019, doi: 10.1364/OL.44.000041.

[188]   K. Knight, *Mathematical Statistics*. CRC Press, 1999.

[189]   P. Stoica and R. L. Moses, *Spectral Analysis of Signals*, 1st edition. Upper Saddle River, N.J: Pearson, 2005.

[190]   S. Zucker, "Cross-correlation and maximum-likelihood analysis: a new approach to combining cross-correlation functions," *Mon. Not. R. Astron. Soc.*, vol. 342, no. 4, pp. 1291–1298, Jul. 2003, doi: 10.1046/j.1365-8711.2003.06633.x.

[191]   M. Bouvier, "The Rejection of Large CW Interferers in Spread Spectrum Systems," *IEEE Trans. Commun.*, vol. 26, no. 2, pp. 254–256, Feb. 1978, doi: 10.1109/TCOM.1978.1094056.

[192] L. B. Milstein, "Interference rejection techniques in spread spectrum communications," *Proc. IEEE*, vol. 76, no. 6, pp. 657–671, Jun. 1988, doi: 10.1109/5.4455.

[193] B. Kelleci, T. W. Fischer, A. İ. Karşılayan, K. Shi, and E. Serpedin, "Adaptive Narrowband Interference Suppression in Multiband OFDM Receivers," *Circuits Syst. Signal Process.*, vol. 27, no. 4, pp. 475–489, Aug. 2008, doi: 10.1007/s00034-008-9041-z.

[194] S. Paesani, M. Borghi, S. Signorini, A. Maïnos, L. Pavesi, and A. Laing, "Near-ideal spontaneous photon sources in silicon quantum photonics," *Nat. Commun.*, vol. 11, no. 1, Art. no. 1, May 2020, doi: 10.1038/s41467-020-16187-8.

[195] C. M. Gentry, G. T. Garcés, X. Zeng, and M. A. Popović, "Tailoring of Individual Photon Lifetimes as a Degree of Freedom in Resonant Quantum Photonic Sources," in *Conference on Lasers and Electro-Optics (2016), paper JTu5A.17*, Jun. 2016, p. JTu5A.17. doi: 10.1364/CLEO_AT.2016.JTu5A.17.

[196] J. B. Christensen, J. G. Koefoed, K. Rottwitt, and C. J. McKinstrie, "Engineering spectrally unentangled photon pairs from nonlinear microring resonators by pump manipulation," *Opt. Lett.*, vol. 43, no. 4, pp. 859–862, Feb. 2018, doi: 10.1364/OL.43.000859.

[197] B. M. Burridge, B. M. Burridge, I. I. Faruque, J. G. Rarity, and J. Barreto, "High spectro-temporal purity single-photons from silicon micro-racetrack resonators using a dual-pulse configuration," *Opt. Lett.*, vol. 45, no. 14, pp. 4048–4051, Jul. 2020, doi: 10.1364/OL.393077.

[198] D. Thomson *et al.*, "Roadmap on silicon photonics," *J. Opt.*, vol. 18, no. 7, p. 073003, Jun. 2016, doi: 10.1088/2040-8978/18/7/073003.

[199] T. J. Seok, K. Kwon, J. Henriksson, J. Luo, and M. C. Wu, "Wafer-scale silicon photonic switches beyond die size limit," *Optica*, vol. 6, no. 4, pp. 490–494, Apr. 2019, doi: 10.1364/OPTICA.6.000490.

[200] Y. Shen *et al.*, "Deep learning with coherent nanophotonic circuits," *Nat. Photonics*, vol. 11, no. 7, Art. no. 7, Jul. 2017, doi: 10.1038/nphoton.2017.93.

[201] N. C. Harris *et al.*, "Quantum transport simulations in a programmable nanophotonic processor," *Nat. Photonics*, vol. 11, no. 7, Art. no. 7, Jul. 2017, doi: 10.1038/nphoton.2017.95.

[202] A. Rao and S. Fathpour, "Compact Lithium Niobate Electrooptic Modulators," *IEEE J. Sel. Top. Quantum Electron.*, vol. 24, no. 4, pp. 1–14, Jul. 2018, doi: 10.1109/JSTQE.2017.2779869.

[203] J. Zhao, C. Ma, M. Rüsing, and S. Mookherjea, "High Quality Entangled Photon Pair Generation in Periodically Poled Thin-Film Lithium Niobate Waveguides," *Phys. Rev. Lett.*, vol. 124, no. 16, p. 163603, Apr. 2020, doi: 10.1103/PhysRevLett.124.163603.

[204] Z. Ma *et al.*, "Ultrabright Quantum Photon Sources on Chip," *Phys. Rev. Lett.*, vol. 125, no. 26, p. 263602, Dec. 2020, doi: 10.1103/PhysRevLett.125.263602.

[205] M. Zhang *et al.*, "Broadband electro-optic frequency comb generation in a lithium niobate microring resonator," *Nature*, vol. 568, no. 7752, Art. no. 7752, Apr. 2019, doi: 10.1038/s41586-019-1008-7.

[206] T. Rudolph, "Why I am optimistic about the silicon-photonic route to quantum computing," *APL Photonics*, vol. 2, no. 3, p. 030901, Mar. 2017, doi: 10.1063/1.4976737.

[207] J. Wang, F. Sciarrino, A. Laing, and M. G. Thompson, "Integrated photonic quantum technologies," *Nat. Photonics*, vol. 14, no. 5, Art. no. 5, May 2020, doi: 10.1038/s41566-019-0532-1.

[208] S. Mittal, V. V. Orre, E. A. Goldschmidt, and M. Hafezi, "Tunable quantum interference using a topological source of indistinguishable photon pairs," *Nat. Photonics*, vol. 15, no. 7, Art. no. 7, Jul. 2021, doi: 10.1038/s41566-021-00810-1.

[209] N. Somaschi *et al.*, "Near-optimal single-photon sources in the solid state," *Nat. Photonics*, vol. 10, no. 5, Art. no. 5, May 2016, doi: 10.1038/nphoton.2016.23.

[210] D. Zhu *et al.*, "Spectral control of nonclassical light using an integrated thin-film lithium niobate modulator." arXiv, Dec. 18, 2021. doi: 10.48550/arXiv.2112.09961.

[211] M. G. Raymer and I. A. Walmsley, "Temporal modes in quantum optics: then and now," *Phys. Scr.*, vol. 95, no. 6, p. 064002, Mar. 2020, doi: 10.1088/1402-4896/ab6153.

[212] N. Fabre, A. Keller, and P. Milman, "Time and frequency as quantum continuous variables," *Phys. Rev. A*, vol. 105, no. 5, p. 052429, May 2022, doi: 10.1103/PhysRevA.105.052429.

[213] H.-H. Lu *et al.*, "A controlled-NOT gate for frequency-bin qubits," *Npj Quantum Inf.*, vol. 5, no. 1, Art. no. 1, Mar. 2019, doi: 10.1038/s41534-019-0137-z.

[214] G. Moody *et al.*, "2022 Roadmap on integrated quantum photonics," *J. Phys. Photonics*, vol. 4, no. 1, p. 012501, Jan. 2022, doi: 10.1088/2515-7647/ac1ef4.

[215] J. Carolan *et al.*, "Universal linear optics," *Science*, vol. 349, no. 6249, pp. 711–716, Aug. 2015, doi: 10.1126/science.aab3642.

[216] F. Kaneda, F. Xu, J. Chapman, and P. G. Kwiat, "Quantum-memory-assisted multi-photon generation for efficient quantum information processing," *Optica*, vol. 4, no. 9, pp. 1034–1037, Sep. 2017, doi: 10.1364/OPTICA.4.001034.

[217] S. Gyger *et al.*, "Reconfigurable photonics with on-chip single-photon detectors," *Nat. Commun.*, vol. 12, no. 1, Art. no. 1, Mar. 2021, doi: 10.1038/s41467-021-21624-3.

[218] C. Xiong *et al.*, "Active temporal multiplexing of indistinguishable heralded single photons," *Nat. Commun.*, vol. 7, no. 1, Art. no. 1, Mar. 2016, doi: 10.1038/ncomms10853.

[219] J. Witzens, "High-Speed Silicon Photonics Modulators," *Proc. IEEE*, vol. 106, no. 12, pp. 2158–2182, Dec. 2018, doi: 10.1109/JPROC.2018.2877636.

[220] X. Tu, C. Song, T. Huang, Z. Chen, and H. Fu, "State of the Art and Perspectives on Silicon Photonic Switches," *Micromachines*, vol. 10, no. 1, Art. no. 1, Jan. 2019, doi: 10.3390/mi10010051.

[221] V. R. Almeida, C. A. Barrios, R. R. Panepucci, and M. Lipson, "All-optical control of light on a silicon chip," *Nature*, vol. 431, no. 7012, Art. no. 7012, Oct. 2004, doi: 10.1038/nature02921.

[222] S. J. Spector *et al.*, "Operation and Optimization of Silicon-Diode-Based Optical Modulators," *IEEE J. Sel. Top. Quantum Electron.*, vol. 16, no. 1, pp. 165–172, Jan. 2010, doi: 10.1109/JSTQE.2009.2027817.

[223] X. Wang *et al.*, "Oscilloscopic Capture of Greater-Than-100 GHz, Ultra-Low Power Optical Waveforms Enabled by Integrated Electrooptic Devices," *J. Light. Technol.*, vol. 38, no. 1, pp. 166–173, Jan. 2020, doi: 10.1109/JLT.2019.2954295.

[224] C. Ma, X. Wang, V. Anant, A. D. Beyer, M. D. Shaw, and S. Mookherjea, "Silicon photonic entangled photon-pair and heralded single photon generation with CAR > 12,000 and g$^{(2)}$(0) < 0.006," *Opt. Express*, vol. 25, no. 26, pp. 32995–33006, Dec. 2017, doi: 10.1364/OE.25.032995.

[225] T.-Y. Chen *et al.*, "Implementation of a 46-node quantum metropolitan area network," *Npj Quantum Inf.*, vol. 7, no. 1, Art. no. 1, Sep. 2021, doi: 10.1038/s41534-021-00474-3.

[226]   M. Sasaki *et al.*, "Field test of quantum key distribution in the Tokyo QKD Network,"
         Opt. Express, vol. 19, no. 11, pp. 10387–10409, May 2011, doi: 10.1364/OE.19.010387.

[227]   S.-Y. Chen, G. Xu, X.-B. Chen, T. Shang, and Y.-X. Yang, "Quantum Cooperative
         Multicast in a Quantum Hybrid Topology Network," *Front. Phys.*, vol. 10, 2022, Accessed:
         Aug. 09, 2022. [Online]. Available:
         https://www.frontiersin.org/articles/10.3389/fphy.2022.842035

[228]   K. Suzuki *et al.*, "Low-Insertion-Loss and Power-Efficient 32×32 Silicon Photonics
         Switch With Extremely High-Δ Silica PLC Connector," *J. Light. Technol.*, vol. 37, no. 1,
         pp. 116–122, Jan. 2019.

[229]   Q. Cheng *et al.*, "Ultralow-crosstalk, strictly non-blocking microring-based optical
         switch," *Photonics Res.*, vol. 7, no. 2, pp. 155–161, Feb. 2019, doi: 10.1364/PRJ.7.000155.

[230]   W. M. Mellette *et al.*, "RotorNet: A Scalable, Low-complexity, Optical Datacenter
         Network," in *Proceedings of the Conference of the ACM Special Interest Group on Data
         Communication*, New York, NY, USA, Aug. 2017, pp. 267–280. doi:
         10.1145/3098822.3098838.

[231]   R. Soref, "Tutorial: Integrated-photonic switching structures," *APL Photonics*, vol. 3, no.
         2, p. 021101, Feb. 2018, doi: 10.1063/1.5017968.

[232]   E. Timurdogan *et al.*, "APSUNY Process Design Kit (PDKv3.0): O, C and L Band
         Silicon Photonics Component Libraries on 300mm Wafers," in *2019 Optical Fiber
         Communications Conference and Exhibition (OFC)*, Mar. 2019, pp. 1–3.

[233]   I. A. Walmsley, "Quantum optics: Science and technology in a new light," *Science*, vol.
         348, no. 6234, pp. 525–530, May 2015, doi: 10.1126/science.aab0097.

[234]   Keysight, "Infiniium UXR-Series Oscilloscopes," *Keysight*.
         https://www.keysight.com/us/en/products/oscilloscopes/infiniium-real-time-
         oscilloscopes/infiniium-uxr-series-oscilloscopes.html (accessed Aug. 23, 2022).

[235]   "XPDV412xR Datasheet by Finisar Corporation | Digi-Key Electronics."
         https://www.digikey.jp/htmldatasheets/production/2382395/0/0/1/xpdv412xr.html
         (accessed Aug. 07, 2022).

[236]   M. Takamiya, M. Mizuno, and K. Nakamura, "An on-chip 100 GHz-sampling rate 8-
         channel sampling oscilloscope with embedded sampling clock generator," in *2002 IEEE
         International Solid-State Circuits Conference. Digest of Technical Papers (Cat.
         No.02CH37315)*, Feb. 2002, vol. 1, pp. 182–458 vol.1. doi: 10.1109/ISSCC.2002.992996.

[237]   H. Füser *et al.*, "Optoelectronic time-domain characterization of a 100 GHz sampling
         oscilloscope," *Meas. Sci. Technol.*, vol. 23, no. 2, p. 025201, Dec. 2011, doi: 10.1088/0957-
         0233/23/2/025201.

[238]   W. Becker, *Advanced Time-Correlated Single Photon Counting Techniques*. Springer
         Science & Business Media, 2005.

[239]   A. McCarthy *et al.*, "Kilometer-range, high resolution depth imaging via 1560 nm
         wavelength single-photon detection," *Opt. Express*, vol. 21, no. 7, pp. 8904–8915, Apr.
         2013, doi: 10.1364/OE.21.008904.

[240]   G. Gariepy *et al.*, "Single-photon sensitive light-in-fight imaging," *Nat. Commun.*, vol. 6,
         no. 1, Art. no. 1, Jan. 2015, doi: 10.1038/ncomms7021.

[241]   A. Kirmani *et al.*, "First-Photon Imaging," *Science*, vol. 343, no. 6166, pp. 58–61, Jan.
         2014, doi: 10.1126/science.1246775.

[242]   M. J. Stevens, R. H. Hadfield, R. E. Schwall, S. W. Nam, and R. P. Mirin, "Time-
         correlated single-photon counting with superconducting single-photon detectors," in

Advanced Photon Counting Techniques, Oct. 2006, vol. 6372, pp. 229–238. doi: 10.1117/12.685447.

[243]   H. Fedder *et al.*, "Characterization of Electro-Optical Devices with Low Jitter Single Photon Detectors – Towards an Optical Sampling Oscilloscope Beyond 100 GHz," in *2018 European Conference on Optical Communication (ECOC)*, Sep. 2018, pp. 1–3. doi: 10.1109/ECOC.2018.8535415.

[244]   C. Dorrer, C. R. Doerr, I. Kang, R. Ryf, J. Leuthold, and P. J. Winzer, "Measurement of eye diagrams and constellation diagrams of optical sources using linear optics and waveguide technology," *J. Light. Technol.*, vol. 23, no. 1, pp. 178–186, Jan. 2005, doi: 10.1109/JLT.2004.840359.

[245]   K. Okamoto and F. Ito, "Nearly Shot-Noise-Limited Performance of Dual-Channel Linear Optical Sampling for Ultrafast DPSK Signals," *IEEE J. Quantum Electron.*, vol. 45, no. 6, pp. 711–719, Jun. 2009, doi: 10.1109/JQE.2009.2013112.

[246]   W. R. Donaldson, J. R. Marciante, and R. G. Roides, "An Optical Replicator for Single-Shot Measurements at 10 GHz With a Dynamic Range of 1800:1," *IEEE J. Quantum Electron.*, vol. 46, no. 2, pp. 191–196, Feb. 2010, doi: 10.1109/JQE.2009.2029544.

[247]   J. Li, J. Hansryd, P. O. Hedekvist, P. A. Andrekson, and S. N. Knudsen, "300-Gb/s eye-diagram measurement by optical sampling using fiber-based parametric amplification," *IEEE Photonics Technol. Lett.*, vol. 13, no. 9, pp. 987–989, Sep. 2001, doi: 10.1109/68.942669.
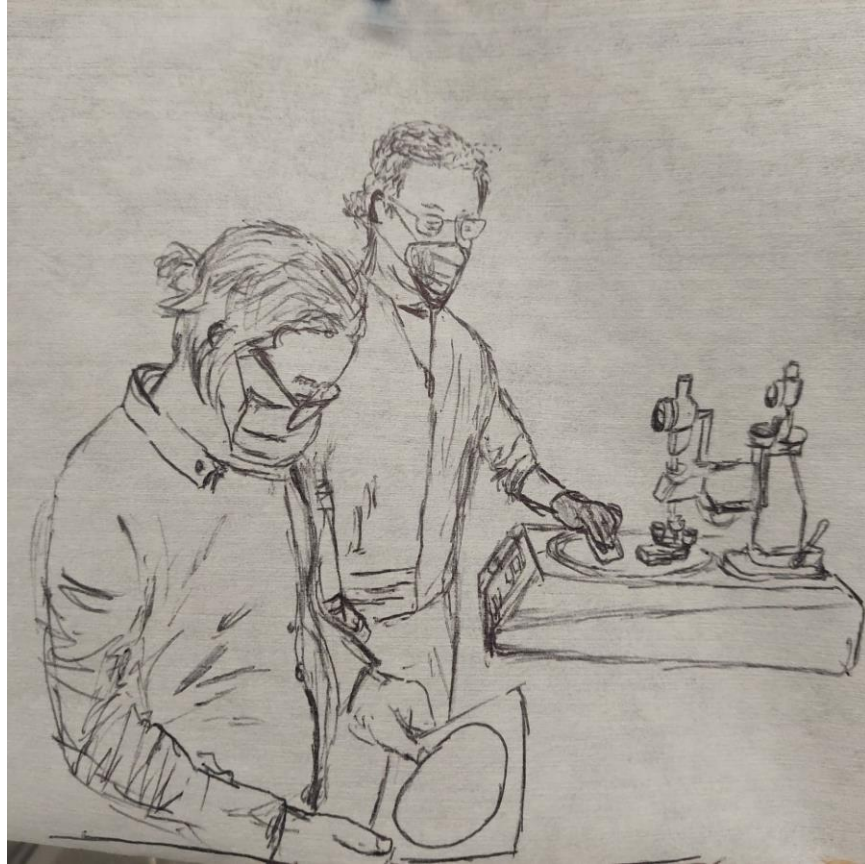
"Courtroom sketch of polishing", art by Xiaoxi Wang.